

The Determination of Lithospheric Rheology and Long-Term Interplate Coupling in Japan: Finite Element Modeling

Shaosong Huang

Dissertation submitted to the Faculty of the Virginia Polytechnic Institute and State
University in partial fulfillment of the requirement for the degree of

Doctor of Philosophy
in
Geophysics

J. Arthur Snoke, Co-chairman
I. Selwyn Sacks, Co-chairman
Kenneth A. Eriksson
Richard D. Law
Edwin S. Robinson

September 26, 1996
Blacksburg, Virginia

Keywords: Lithosphere rheology, Subduction-zone interplate coupling,
Finite-element modeling

The Determination of Lithospheric Rheology and Long-Term Interplate Coupling in Japan: Finite Element Modeling

Shaosong Huang

(ABSTRACT)

Northeast Japan experienced an approximately constant, compressional deformation during the last 5 million years resulting from the steady subduction of the Pacific plate. Because the direction of the maximum compression axis is approximately perpendicular to the strike of the island arc, 2-D finite-element modeling can be used to examine the deformation over time of the island-arc lithosphere. The model geometry is based on geophysical and geological data, and each model run requires an assumed rheology and interplate coupling. Novel to our modeling is the ability to include erosion/deposition loading and the creation of strike-slip faults, based on a dynamically-applied fracture criterion. The criterion for acceptability is how well a model matches observed present-day topography, gravity, and seismicity patterns. Results given below are for models that satisfy this criterion.

The long-term effective elastic thickness is 10 km in the inner arc, increasing to about 50 km near the trench. The effective elastic thickness in the inner arc is therefore much smaller than the about 30 km short-term elastic thickness estimated from seismological data. The viscosity of the lower crust is on the order of 10^{22} Pa s or less.

The strength of interplate coupling off Sanriku is about two to four times greater than off Miyagi, and there is about twice as strong a coupling at greater depths. The relative strength of coupling correlates well with the observed interplate seismicity. Hence the inferred weaker coupling off Miyagi indicates a lack of seismogenic potential -- a low probability for large earthquakes in that region, not just a long return cycle.

The same modeling procedure was also applied to southwest Japan. The viscosity of the lower crust is not more than 10^{21} Pa s, and the elastic thickness is about 10 km. The calculated strength of interplate coupling for southwest Japan is about 1.5 times greater than for the off-Sanriku region in northeast Japan, which correlates well with the fact that there have been great ($M > 8$) earthquakes in the Nankai Trough region, but none that large in the off-Sanriku region.

Acknowledgments

First of all, I would like to express my thanks to my parents for their support and encouragement throughout these years. They pushed me to excel. A special thanks to my wife, Ying, for her support and assistance during my graduate study in Blacksburg. She sacrificed her own beloved career in medicine to follow me to study abroad. I can not image how hard it is to give up one's career and to resume another. She helped me in many ways during the dissertation preparation: typing manuscripts, proofing, and preparing figures on the Macintosh.

I would like to thanks Dr. Kenneth A. Eriksson for his recognition of my academic potential when I was in China. He and Dr. Susan Eriksson gave me a good orientation to graduate study here, and provided much assistance to help me adapt to the environment in Blacksburg.

On the scholastic side of life, I wish to express my sincere thanks to Dr. J. Arthur Snoke, my academic co-advisor, for his constant encouragement, generous help and careful guidance. I have learned from him novel approaches for implementing geophysical processes on to the computer. I would like to thank him for teaching me logical thinking in the English language. This dissertation profits greatly from his advice, and I am indebted to him for his continuous support throughout my stay in Blacksburg.

I owe a great deal to Dr. I. Selwyn Sacks, my co-advisor, for the initialization of the dissertation project, for providing me the opportunity to work at the Department of Terrestrial Magnetism of the Carnegie Institution of Washington as a predoctoral fellow, and his thorough guidance on the research project. I am especially appreciative of his thoughtful responses to my research questions. I am also grateful to him for his detailed and critical review of the dissertation. He has such a sharp mind!

I am grateful to Drs. Edwin S. Robinson, Kenneth A. Eriksson and Richard D. Law for their useful discussions in many different fields during my graduate study and their careful review of the dissertation.

I wish to thank Drs. A. Hasegawa and T. Matsuzawa for discussion and advice in the geophysics of Japan, and Drs. H. J. Melosh, and M. H. Wallace for help and suggestions in finite-element modeling. Dr. H. J. Melosh kindly provided the finite-element code, TECTON for use in the dissertation study. Martin Chapman and Matt Sibol provided generous support in seismicity studies. I would like to thank follow graduate students in the Department of Geological Sciences for help in various aspects, especially Jun Lu, Eric Gardner, and Jane Gardner. It would have been much more difficult for me to adapt to study and living in Blacksburg without their helps. I also want to thank fellow students Bill Domoracki and Sam Peavy for discussions in geophysics.

This research was partially supported by 1994 and 1995 student research grants from the Geological Society of America and a 1994 Sigma Xi research grant. Computation facilities were provided by the Department of Geological Sciences, Virginia Polytechnic Institute and State University, and the Department of Terrestrial Magnetism, Carnegie Institution of Washington. During my studies in Blacksburg, financial support was received from the Department of Geological Sciences in the form of a two-year teaching assistantship, and a two-year research assistantship from the Virginia Tech Seismological Observatory.

Table of Contents

1	Introduction	1
2	Compressional deformation of island arc lithosphere in northeast Japan resulting from long-term subduction-related tectonic forces: finite element modeling	3
2.1	Introduction.....	3
2.1.1	Tectonic setting.....	3
2.1.2	Lithospheric folding.....	4
2.1.3	Approaches.....	4
2.2	Geophysical data.....	5
2.3	Finite element modeling.....	5
2.3.1	Modeling preliminaries.....	6
2.3.2	Stick-slip faulting.....	6
2.3.3	Erosion and deposition.....	7
2.4	Application.....	7
2.4.1	The starting model.....	7
2.4.2	The model.....	8
2.4.3	Boundary conditions	9
2.4.4	Model discussion	10
2.5	Results.....	11
2.5.1	Stress, topography, gravity, and fault slip.....	11
2.5.2	Comparison with observed data.....	11
2.5.3	Discussion	12
2.6	Conclusions.....	13
3	Topography and seismic effects of long term coupling between the subducting plate and the overriding plate in northeast Japan	30
3.1	Introduction.....	30
3.2	Coupling	30
3.3	Basic modeling concepts.....	31
3.3.1	Modeling approach	31
3.3.2	Stick-slip faulting.....	32
3.3.3	Erosion and deposition.....	32
3.4	Geophysical data in northeast japan.....	32
3.4.1	Earthquakes.....	32
3.4.2	Gravity and topography.....	33
3.4.3	Heat flow and the Curie depth.....	33
3.5	Implementation of coupling in finite element modeling.....	34
3.6	Modeling.....	34

3.6.1	Modeling preliminaries.....	35
3.6.2	Boundary conditions.....	36
3.6.3	Faulting.....	36
3.7	Results.....	37
3.7.1	Region 1.....	37
3.7.2	Region 2.....	38
3.8	Discussions.....	38
3.8.1	Interplate seismicity and coupling.....	38
3.8.2	Aseismic front and seismicity in the outer arc	39
3.8.3	Intraplate seismicity.....	39
3.9	Conclusions.....	40
4	Large scale deformation of island arc lithosphere beneath southwest Japan in the latest Cenozoic: finite element modeling	57
4.1	Introduction.....	57
4.2	Geophysical data	58
4.2.1	Topography, gravity, and heat flow.....	58
4.2.2	Interplate seismicity.....	59
4.3	Finite element modeling.....	59
4.3.1	Modeling preliminaries.....	59
4.3.2	Model.....	59
4.3.3	Boundary conditions.....	60
4.3.3	Time history	61
4.4	Results	61
4.4.1	Effect of lower-crust viscosity	61
4.4.2	Varying the depth dependence of coupling.....	61
4.4.3	Varying the coupling magnitude	62
4.4.3	Summary	62
4.5	Discussions.....	62
4.5.1	Topography and gravity in the outer-arc slope	62
4.5.2	Topography and gravity in the outer-arc slope	62
4.5.3	Interplate seismicity and coupling.....	63
4.6	Conclusions.....	63
	Bibliography.....	73
	Appendix A: Calculation of gravity anomaly from a deformed FEM grid.....	78
	Appendix B: Failure criterion	78
	Appendix C: Implementation of erosion and deposition	79
	Appendix D: Nonlinear viscosity.....	80
	Vita	83

List of tables

Table 2.1: Material properties of the model	8
Table 3.1: Material properties of the model for both the southern region and the northern region.....	35
Table 4.1: Material properties of the model	60
Table 4.2: Viscosity of the lower crust.....	60
Table D.1: Steady-state flow-law parameters for granite, granulite, and dunite...	82

List of figures

Figure 2.1: Map of the study area in northeast Honshu, Japan.....	14
Figure 2.2: Amount of uplift / subsidence during the Quaternary period in northeast Japan.....	15
Figure 2.3: Shallow seismicity in northeastern japan from 1975 to 1982	16
Figure 2.4: Profiles of (a) gravity residual, (b) topography, and (c) heat flow In northeast Honshu	17
Figure 2.5: Gravitational effect of a denser subducting slab	18
Figure 2.6: Schematic diagrams to illustrate Bouguer gravity, isostatic gravity, and gravity residual of a mountain in two end-member cases.....	19
Figure 2.7: A Stick-Slip Faulting Test	20
Figure 2.8: Starting model for finite-element analysis	21
Figure 2.9: The FEM grid and material properties and boundary conditions	22
Figure 2.10: Horizontal stress and PTF at 1.8 ma, just before faulting	23
Figure 2.11: Orientation of the faults in the model.....	24
Figure 2.12: Horizontal stress averaged along the plate thickness versus time	25
Figure 2.13: Calculated topography and gravity residual of the model.....	26
Figure 2.14: Three models for comparison in Figure 2.15	27
Figure 2.15: Comparison of topography (left) and gravity residual (right) with observations among three types of viscosity structures.....	28
Figure 2.16: A schematic rheological structure of the lithosphere in northeast Japan derived from the finite element modeling	29
Figure 3.1: Study area in northeast Honshu, Japan	41
Figure 3.2: Aftershock area for the shallow (60 km) interplate earthquakes with magnitude 7 or greater in the period from 1962 to 1983.....	42
Figure 3.3: A schematic cross section to illustrate coupling between the downgoing oceanic plate and the overriding continental plate.....	43
Figure 3.4: Cross sections of shallow earthquakes (<60 km)	44
Figure 3.5: Topography and gravity in northeast Japan in region 1, 2 and 3.....	45
Figure 3.6: Depth dependence of coupling between the subducting and overriding plates	46
Figure 3.7: Zooming in on the model in region 1.....	47
Figure 3.8: Finite element model for region 2.....	48
Figure 3.9: Horizontal stress (a) and PTF (b) just before faults initiate.	49
Figure 3.10: Zooming in on the model in region 2.....	50
Figure 3.11: Effect of coupling strength in region 1	51
Figure 3.12: The effect of coupling ratio on topography and gravity in region 1.....	52
Figure 3.13: Effect of C_0 on topography (left) and gravity (right) in region 2.	53
Figure 3.14: Effect of C_r on topography (left) and gravity (right) in region 2:	54

Figure 3.15: Overlaying of PTF and intraplate seismicity at 5 ma.....	55
Figure 3.16: Schematic profiles in northeast Japan showing coupling and its relationship to topography, gravity and seismicity.....	56
Figure 4.1: Study area of southwest Japan.	64
Figure 4.2: Topography and gravity residual anomaly profiles along A-A' (a,b) , and B-B' (c,d) in southwest japan.....	65
Figure 4.3: The gravitational effect of the dense subducting Philippine plate.	66
Figure 4.4: Heat flow in southwest Japan.	67
Figure 4.5: Interplate earthquakes in 1944 and 1946	68
Figure 4.6: Finite element model: (a) The boundary conditions and the material properties. (b) The mesh in the outer arc region.....	69
Figure 4.7: Effect of lower crust viscosity on topography (left panel) and gravity residual anomaly (right panel).....	70
Figure 4.8: Effect of C_r on topography (left) and gravity (right) in southwest Japan.	71
Figure 4.9: Effect of C_0 on topography (left) and gravity (right) in southwest Japan.....	72

Chapter 1: Introduction

For at least 5 million years, Japan has experienced compressional tectonics with a high rate of deformation, especially in northeast Japan (Hashimoto, 1991; Matsuda et al., 1967). The compressional deformation is characterized by folding of the upper crust (Matsuda et al., 1967; Sato, 1994). The flexural response of lithosphere under vertical loading and subduction-related tectonic forces may explain the undulative deformation in Japan. The flexure of the oceanic plate in subduction zones is of the form of a damped sinusoid oscillation (Turcotte and Schubert, 1982). The model explains the upwarping of the oceanic plate adjacent to the trench. We expect that similar upwarping will occur on the continental side due to the long-term compressional subduction-related forces.

In this dissertation, the following questions are addressed about the compressional lithospheric deformation in Japan: First, the rheological structure of the island arc lithosphere; Second, how does the subduction-related force system, i.e., interplate coupling, control lithosphere deformation? Third, the nature of interplate thrust earthquakes, and how the interplate and intraplate seismicity is related to the interplate coupling; Fourth, the effect of the Quaternary volcanic front, and the formation of the inland sea in southwest Japan; Finally, how do the surface processes, erosion and deposition, affect the lithosphere deformation?

The unique geological settings, along with a wealth of available seismicity, gravity, topographic, heat flow, and crustal motion data, provide the constraints which allow a test of the hypothesis that the large-scale features of topography, gravity and seismicity in northeast and southwest Japan result from tectonic compression, and, in the context of that model, allow the determination of the lithosphere rheology and long-term coupling along the interface between the subducting plate and the overriding oceanic plate.

Due to the large variation of observed heat flow and the corresponding changes in lithospheric rheology from the inner to the outer arc, an analytical solution based on simple beam theory cannot be used to model the undulative deformation. Hence a numerical analysis procedure, finite element modeling, is employed. Because the steady subduction of the study areas is approximately perpendicular to the strike of the present mountain system, it suffices to use a 2-D model in the analysis of the nature of the compressional deformation.

Chapters 2, 3 and 4 are papers which have been submitted to the journal *Tectonophysics*. As of this writing, the paper comprising Chapter 3 has been accepted, while the papers comprising Chapters 2 and 4 are under review. Because the papers are on a common theme, there is only a single reference list at the end, as well as a single Acknowledgment section. Aside from that, along with the single abstract, the format is as used in *Tectonophysics*. There are four appendices to describe some details of finite element modeling and viscosity estimate.

Chapter 2 focuses on the Kitakami range and off-Sanriku region, of northeast Japan. The Kitakami range has a positive isostatic gravity anomaly, which indicates that the region is out of isostatic equilibrium. The finite element modeling code TECTON (Melosh and Raefsky, 1980; Wallace and Melosh, 1994) was adapted to analyze the deformation of folding and faulting of island arc lithosphere resulting from long-term compressional forces and slab drag using appropriate rheologies, lithospheric thickness and faulting systems. The code was modified to

allow the simulation of stick-slip behavior of faults with different stress-drop ratios, and we have added the capability of including the effects of erosion/deposition and time-dependent loading. These allow the monitoring of the long-term deformation of island-arc lithosphere with forces from the subduction of the Pacific plate as well as the surface processes of erosion and deposition.

A critical requirement we apply in our modeling is that it should be consistent with the observed relationship between topography and gravity as well as providing a plausible explanation for the observed seismicity patterns. Our starting model is based on geophysical data in northeast Japan. To evaluate the gravity observations, we use the *gravity residual anomaly*, (GRA), which is defined here as the Bouguer gravity anomaly with an Airy isostatic correction as well as a correction for the dense subducting plate. (Without the slab correction, this is the same as what Sugimura and Uyeda (1973) call the Airy isostatic anomaly.) The gravity residual anomaly is hence a measure of departure from isostatic equilibrium. Comparing the computed topography and GRA with the observed values leads to changes of parameters of viscosity, and the degree of interplate coupling. we show that viscosity structure, interplate coupling, and erosion/deposition are three major factors affecting lithosphere deformation in northeast Japan. The focus of Chapter 2 is the determination of the viscosity structure in northeast Japan.

The characteristics of topography, gravity, intraplate and interplate seismicity is not uniform along the strike of the Japan trench. we consider three regions: off Sanriku to the north (Region 1), off Miyagi (Region 2), and off Fukushima (Region 3) to the south. There are more large ($M > 7.5$) thrust earthquakes off the Pacific coast in region 1 (off Sanriku) than in region 2 (off Miyagi and off Fukushima) of northeast Japan. The aftershock area is also larger in region 1. Region 1 has the highest topography and GRA, while region 2 has the lowest elevation and GRA. Chapter 3 focuses on the effects of interplate coupling on topography, gravity and seismicity assuming the same rheological structure derived in Chapter 2.

In Chapter 4, the analysis is extended to southwest Japan. During the latest Cenozoic period (4-6 Ma), the Philippine Sea plate subducted under the southwest Japan island-arc plate in a direction nearly normal to the Nankai trough. The N-S compressional subduction forces resulted in the formation of the nearly E-W striking warping with a wavelength of about 150-200 km. The magnitude of the undulative deformation is greater than for northeast Japan. Moreover, historically there have been great ($M > 8$) earthquakes in the Nankai Trough region, but none that large in the off-Sanriku region. Based on our modeling for the subduction beneath northeast Japan, strong interplate coupling appears to be correlated with the potential for large interplate earthquakes. we propose that the coupling for southwest Japan is even greater than for northeast Japan. In Chapter 4 it is shown that a plausible viscosity structure and interplate coupling can explain the undulative deformation and formation of the inland sea as well as the potential for great earthquakes.

Two novel features of the modeling used in this study warrant special emphasis: First, this is the first model which provides constraints on the long-term lithosphere rheology and interplate coupling based on their effects on observed present-day topography, gravity, and seismicity patterns. Second, the modeled constraints on interplate coupling are the first alternative to observed recurrence cycles as a method to predict the potential occurrence of large-magnitude interplate earthquakes.

Chapter 2: Compressional Deformation of Island Arc Lithosphere in northeast Japan Resulting From Long-Term Subduction-Related Tectonic Forces: Finite Element Modeling

2.1 Introduction

For at least the past 5 million years, subduction of the western Pacific plate has been steady in a direction approximately perpendicular to the strike of the present mountain system of northeast Japan. Throughout this period, northeast Japan has experienced compressional tectonics with a high rate of deformation, the maximum compression axis lying in a WNW direction, along the direction of subduction (Hashimoto, 1991; Matsuda et al., 1967). Sugimura and Uyeda (1973) suggest that the present-day topography is due mainly to the compressional activities during this period. In this paper we examine that hypothesis using finite-element modeling. In addition to modeling the present-day topography, we model the present-day gravity and seismicity patterns.

2.1.1 Tectonic Setting

The northeast Japan Island arc is divided into two regions: an inner arc and an outer arc. The outer arc includes the Kitakami region, while the inner arc extends from the central Backbone range to the west Japan Sea coast. The central Backbone range runs about north-south through the region. The Quaternary volcanic front is located in approximately the middle of the Backbone range (Fig. 2.1).

Northeast Japan experienced extensional deformation from 25 Ma to 14 Ma with the opening of the Japan Sea. The extension of the Japan Sea stopped at about 14 Ma. A neutral stress regime prevailed with weak extension between 13 Ma and 8 Ma and with weak compression between 8 Ma and 4 Ma. Compressional deformation has dominated since 4 Ma (Sato, 1994; Hashimoto, 1991). The compressional deformation is characterized by reverse faulting and folding of the late Cenozoic strata in the subsidence areas (Matsuda et al., 1967; Sato, 1994). The strike of reverse faults and folds is parallel to the arc. The reconstructed Quaternary stress field from these faults indicates that the maximum principal axis was horizontal and normal to the Japan trench axis, and the minimum principal stress axis was oriented vertically (Sato, 1986, 1994). Focal mechanisms yielded similar results (Wesnousky et al. 1982; Yamazaki et al., 1985). The outer arc region, especially the Kitakami range, was uplifted in the late Cenozoic, which resulted in low relief erosion surfaces, and raised marine terraces (Sugimura and Uyeda, 1973). The amount of uplift of the Kitakami range is about 750 m during the Quaternary (Fig. 2.2). In the western coastal region, subsidence is remarkable; the sedimentation rate in Akita basin has been 620 meters per million years (Sato, 1994).

Rydelek and Sacks (1990) proposed that the subparallel shallow seismic concentration zones striking nearly N-S beneath the central and western coastal areas of northeast Japan may be due to the buckling of the lithosphere driven by the tectonic compression. The undulating structure

of the upper crust was inferred from gravity data, the seismic velocity model (fig. 4 in Segawa and Tomoda, 1976) and estimates of uplift/subsidence inferred from observations (Matsuda, et al., 1967). Due to the large variation of observed heat flow and the corresponding changes in lithospheric rheology from the inner to the outer arc, an analytical solution of simple beam theory cannot be used.

2.1.2 Lithospheric folding

The flexural response of lithosphere under vertical loading and horizontal tectonic forces has been used as a mechanism for the formation of intracratonic and foreland basins (Karner and Weissel, 1990; Lambeck 1983 a, b). Buckling, a periodic undulation, is an end-member of flexural lithospheric deformation processes (McAdoo and Sandwell, 1985; Stephenson, et al., 1990, 1991; Wallace and Melosh, 1994). Karner and Weissel (1990) demonstrated that the folding of a 10-15 km elastic lithosphere can be achieved, after the introduction of sea mount loading, by the amplification of selected wavelengths of earlier lithospheric deformation driven by a horizontal force of 2.0×10^{13} N/m. Lambeck (1983a, b) applied viscoelastic rheology, sedimentary loading and a horizontal tectonic force to achieve folding of the continental lithosphere in central Australia to explain the formation of the intracratonic basins for the last 900 Ma. Erosion and deposition further enhance vertical warping and lower the buckling force (Lambeck, 1983a, b; Karner and Weissel, 1990).

Turcotte and Schubert (1982) modeled the flexure of the oceanic plate in subduction zones. Their model predicts that the deflection will be of the form of a damped sinusoid oscillation, and it matches the bathymetry well. The model explains the upwarping of the oceanic plate adjacent to the trench. We expect that similar upwarping will occur on the continental side. Formally, the model of Turcotte and Schubert (1982) does not produce an undulative deformation on the overriding plate since the shape of the deformed plate is that of a critically damped sinusoid.

However, in northeast Japan, the deformation is strongly influenced by the long-term horizontal compression from the Pacific plate, sedimentation loading in the west Japan Sea coast area, volcanic loading in the central region, and the lateral variation of the lithospheric thickness and rheology.

2.1.3 Approaches

The finite element modeling code TECTON (Melosh and Raefsky, 1980; Wallace and Melosh, 1994) has been adapted to analyze the deformation of folding and faulting of island arc lithosphere resulting from long-term compressional forces and slab drag using appropriate rheologies, lithospheric thickness and faulting systems. A critical requirement we apply in our modeling is that it should be consistent with the observed relationship between topography and gravity.

Our starting model is based on geophysical data in northeast Japan. Our final model allows us to explain the major features of the topography, gravity and seismicity in the region.

2.2 Geophysical data

There are two shallow seismic zones striking slightly east of north in northeast Japan: one in the middle of Honshu Island, and the other in the western coastal area (Fig. 2.3). There is also an aseismic front, defined usually as the boundary between the landward aseismic region and the seaward seismic region, in the mantle wedge between the subducting plate and the crust. The aseismic front is almost parallel to the volcanic front, striking nearly north-south in northeast Japan. There are few earthquakes in the area between the volcanic front and the aseismic front, but many between the aseismic front and the Japan trench.

Figure 2.4 shows profiles of gravity, topography and heat flow in northeast Japan. The gravity data are Bouguer (on land) and free-air (at sea) taken from Kono and Furuse (1989). The gravity data and topographic/bathymetric data were projected along a transect, 20 km wide from 137°E 39.75°N to 145°E 39.5°N (Fig. 2.1). The free-air gravity anomalies were converted to Bouguer gravity anomalies. Airy isostatic gravity was computed from the topography and bathymetric data assuming a crustal thickness of 30 km at the coast (Zhao et al., 1994; Research Group for Explosion Seismology, 1973), and a density of 2.67 g/cm³ for the crust and 3.3 g/cm³ for the upper mantle. The denser subducting Pacific slab produces a positive gravity signature, causing a tilting of the Bouguer gravity anomaly toward the west. Figure 2.5 shows the gravity signature due to the denser subducting Pacific slab beneath northeast Japan. The maximum gravity signature (300 mGal) is near the Japan trench.

The gravity residual anomaly (g_{res}), is obtained from the following equation:

$$g_{res} = g_b - g_s - g_i$$

Where g_b is the Bouguer gravity anomaly, g_s the gravity correction from the denser subducting slab, and g_i the isostatic correction assuming Airy compensation. The gravity residual anomaly indicates whether the region is in or out of isostatic equilibrium (Fig. 2.6). Figure 2.4 shows that the Kitakami range has a maximum positive gravity residual anomaly of 75 mGal.

Heat flow data come from Pollack et al. (1993), and are projected along a transect 100 km wide from 137°E 39.75°N to 145°E 39.5°N (Fig. 2.1). Heat flow data show high scatter, but the average is about 100 mWm⁻² in the inner arc, and decreases to 40 mWm⁻² in the outer arc. The heat flow at the volcanic front is about 150 mWm⁻² (Fig. 2.5c).

2.3 Finite element modeling

Because the strike of folds and faults in northeast Japan is approximately perpendicular to the direction of subduction, a 2-D plane-strain finite-element analysis suffices to define the mechanical behavior of the lithosphere assuming a realistic rheology and boundary conditions. The exact plane-strain element in TECTON (Melosh and Raefsky, 1980; Wallace and Melosh, 1994), is used to analyze the response of the northeast Japan lithosphere to the subduction of the western Pacific plate during the past 5 million years. We modified the code to allow the simulation of stick-slip behavior of faults with different stress drop ratios, and we added the capability of including the effects of erosion/deposition and of time-dependent loading. These allow us to

monitor the long term deformation of island-arc lithosphere with forces from the subduction of the Pacific plate as well as the surface processes of erosion and deposition.

2.3.1 *Modeling Preliminaries*

We discuss here relevant concepts related to gravity and rheology.

Gravity residual anomaly: A critical requirement is that our models match the observed gravity field, in particular the non-isostatic-equilibrium residuals. To evaluate the gravity observations, we use the *gravity residual anomaly*, (GRA), which is defined here as the Bouguer gravity anomaly with an Airy isostatic correction as well as a correction for the dense subducting plate. The gravity residual anomaly is hence a measure of departure from isostatic equilibrium. Mountain ranges in isostatic equilibrium have a negative Bouguer gravity signature, and a zero gravity residual anomaly. However, if the mountain is part of a lithospheric fold (e.g., supported by compressive forces), the upwarping upper mantle with its larger density would cause a more positive Bouguer anomaly and a positive gravity residual anomaly (Fig. 2.6). Appendix A shows how to calculate the gravity residual anomaly from a deformed finite element grid.

Rheology: Material properties of the lithosphere are critically important in the analysis of the long-term lithospheric deformation. Several lithospheric rheologies have been explored to explain flexural behavior: elastic, viscoelastic, and plastic (Turcotte and Schubert, 1982; Watts, 1992; Wessel et al., 1980; Martinod and Davy, 1992, 1994; Lambeck 1983a,b; Zuber, 1987). There is, however, no consensus on the most appropriate rheology for the long-term time scale. In our modeling the stress changes are over a very wide period range because we include earthquake induced faulting. Hence we use a linear visco-elastic rheology.

2.3.2 *Stick-slip faulting*

Repeated earthquake faulting must be incorporated in our modeling because it can contribute to the growth of geological structure over the long term (King et al., 1988). The location of faults and the amount of slipping are controlled by the stress field and the Mohr-Coulomb criterion.

A description of the slippery-node method to simulate faulting was given by Melosh and Williams (1989). Mohr-Coulomb failure criterion is used to determine when fault slips (Appendix B). The proximity to failure (PTF) is the ratio of the observed maximum differential stress to the maximum differential stress predicted by the Mohr-Coulomb criterion. The fault slips whenever the PTF is greater than 1.0. With the original code, numerical instabilities can occur when a locked fault is released and slips. A restoring force at those slippery nodes was used to control the amount of fault slipping in TECTON. When the fault is unlocked (slips), a large artificial restoring force is generated. A reasonably small Winkler force has been introduced to minimize numerical error, following Melosh and William (1989). If the fault is only unlocked once and continuously slips, the error can be ignored. However, in the case of multiple unlocking, the error will build up significantly and affect numerical stability. We avoid this numerical instability

by setting the Winkler force at the time step of the fault's unlocking to be zero. The displacement at the slippery node will then not cause a large restoring force.

For the modified slippery node method, the fault first slips when the PTF exceeds 1.0. The fault slips for only one time step resulting in a stress drop ratio, which can arbitrarily be chosen to vary from 0% to 100%, and then is locked to again allow stress build-up on the fault plane. As soon as the PTF exceeds 1.0 again, the fault will be unlocked (slips). The process repeats for the total model run time.

Using our modified slippery node approach we are able to reproduce the analytic solution from Turcotte and Schubert (1982, pp 359-360, equation 8-53) as shown in Figure 2.7.

2.3.3 Erosion and deposition

Tests show that the expected amount of rearrangement of surface mass by erosion and deposition has a significant effect on the displacement field and stress state of the deformable lithosphere. Ohmori (1978) showed that the erosion rate of mountain range in Japan is about 0.3 mm/year at an elevation of 1000 m. Therefore, in 5 Ma, about 1.5 km of material would be removed from the Backbone range and the Kitakami range. Obviously, the effect of erosion and deposition must be modeled. We modified and implemented for use in TECTON the scheme of erosion and deposition developed by Sato and Matsu'ura (1993). Erosion and deposition cause modification of surface topography as well as loading and unloading on the lithosphere. Erosion is treated as a set of upward forces acting at the top of the plate, while sedimentation is treated as a downward force. An empirical observation is that in Japan the rate of erosion for the mountainous regions is in proportion to the square of the land height (Ohmori, 1978). See Appendix C for details of implementation of erosion and deposition in finite element modeling.

2.4 Application

2.4.1 The starting model

Our finite element models are based on observed estimates of the crustal thickness, the Curie depth, and heat flow, as well as on other estimates of the viscosity structure in northeast Japan.

The thickness of the continental crust in northeast Japan is about 30 km beneath the land area (Research group for explosion seismology, 1977; Zhao et al., 1992). Rydelek and Sacks (1988, 1990) found that an elastic lithosphere of 30 km, and a viscoelastic asthenosphere with a viscosity of 10^{19} Pa s, satisfied deformation data in northeast Japan.

Rock rheology depends on temperature: as rocks get hotter, their viscosity decreases. We therefore use surface heat flow as the major determinant for viscosity structure. We constructed a strength profile of the lithosphere based on heat-flow data and experimentally-based rheology laws (Byerlee, 1967; Carter and Tsenn, 1987; Wilks and Carter, 1990). See Appendix D for details. The depth of the brittle-ductile transition is about 5 km at the inner arc and increases to about 50 km at the east of the outer arc (Fig. 2.8). Because viscosity depends on strain rates or differential stress at a fixed strain rate, the results give only an approximate starting point and require further refining by numerical modeling.

Aeromagnetic data provide additional constraints on the properties of the lithosphere. The spectral analysis of aeromagnetic data has been used to estimate the Curie depth, the depth at which the crustal temperature reaches the Curie point of the dominant magnetic minerals (Okubo and Matsunaga, 1994). The Curie depth is taken to define the isotherm of 450°C in the inner arc (Okubo et al., 1989, 1991). The effective elastic thickness of the continental lithosphere has been correlated with the depth of the 450°C isotherm (Watts, 1992). The Curie depth is about 10 km in the inner arc, 30 km at the aseismic front, and increases to about 50 km near the Japan trench (Fig. 2.8).

In summary, we estimate that the elastic thickness of northeast Japan increases from about 5 to 10 km at the inner arc to about 30 km at the outer arc.

2.4.2 The model

We determine the viscosity structure by varying the model (Fig. 2.8) to find the best fit to the observations. The right (east) boundary is the interface between the subducting slab and the overriding plate. The shape of the interface is based on the results of Suyehiro and Nishizawa (1994) and Umino et al. (1992). The coupled interface is about 50 km deep beneath the coast line. The initial bathymetry is assumed to be 1 km in the Japan Sea and 2.5 km at the trench.

Table 2.1. Material properties of the model

No.	E (Pa s)	Density (kg/m ³)	Viscosity (Pa s)	Poison's ratio
1	6.5x10 ¹⁰	2400	elastic	0.25
2	5.5x10 ¹⁰	2400	elastic	0.25
3	4.5x10 ¹⁰	2400	elastic	0.25
4	5.5x10 ¹⁰	2400	elastic	0.25
5	6.5x10 ¹⁰	2500	elastic	0.25
6	5.5x10 ¹⁰	2500	elastic	0.25
7	4.5x10 ¹⁰	2500	elastic	0.25
8	5.5x10 ¹⁰	2500	elastic	0.25
9	6.5x10 ¹⁰	2600	1.0x10 ²²	0.25
10	5.5x10 ¹⁰	2600	1.0x10 ²²	0.25
11	4.5x10 ¹⁰	2600	1.0x10 ²²	0.25
12	5.5x10 ¹⁰	2600	elastic	0.25
13	6.5x10 ¹⁰	2800	1.0x10 ²²	0.25
14	5.5x10 ¹⁰	2800	1.0x10 ²²	0.25
15	4.5x10 ¹⁰	2800	1.0x10 ²²	0.25
16	5.5x10 ¹⁰	2800	elastic	0.25
17	5.5x10 ¹⁰	3000	2.5x10 ²⁴	0.25

The finite element grid is 800 km long and has 1843 nodes and 1592 elements. The upper layer is elastic, while the lower layers are linearly viscoelastic (Fig. 2.9a, b). Material properties are listed in Table 2.1. Slight differences in Young's modulus and density are included in the model for the oceanic Japan sea crust and the land crust. Because of the high heat flow and low seismic velocity from a tomography analysis (Zhao et al., 1994), Young's modulus is made lower in the volcanic front region. The density below the inner arc plate is 2.8 g/cm^3 corresponding to its lower seismic velocity. The density below the Japan sea and the outer arc is 3.0 g/cm^3 (see Table 2.1). Density increases with depth. Gravitational body forces are included in the model. Over a long-term time scale, i.e., millions of years, the gravitational stress field approaches hydrostatic, because the differential stress will diminish by viscous creep.

2.4.3 Boundary conditions

Surface Loads: The coastal plain of Japan sea is underlain by thick Neogene sedimentary and volcanic rocks (Hashimoto, 1991; Takami, 1988). Those rocks are treated as a surface load. Erupted volcanic rocks at the volcanic front, having an eruption rate of 25 km^3 per million years per km along the strike of the volcanic front (Sugimura and Uyeda, 1973), are treated as a time-dependent surface load. Thus, surface loads of sea water, sediments at the west coast, and the volcanic rocks near the volcanoes are applied on the upper surface.

Tectonic Loads: The left (west) edge of the model is constrained to move in the vertical direction only, and vertical Winkler restoring forces are applied to the bottom of the mesh to simulate isostasy (Wallace and Melosh, 1994; Williams, 1990). Based on the result of Rydelek and Sacks (1990), the viscosity of asthenosphere is taken to be on the order of 10^{19} Pa s . For long-term geological processes, the asthenosphere can be treated as a fluid. Thus, the application of a Winkler force is necessary to simulate the restoring forces. For the right (east) edge, we take into account coupling between the subducting Pacific plate and the overriding plate.

The state of coupling along the interplate boundary is affected by the force system acting on the overriding plate. High pore pressure in the subducted sediments may cause weak coupling at depths shallower than approximately 10 km. Suyehiro and Nishizawa (1994), from observations of shallow slab interface seismicity, suggest that the coupling between the subducting Pacific plate and the overlying plate starts at a depth greater than 10 km.

The vertical forces due to the oblique slab drag are specified. Horizontal compressive forces are implemented as displacement increments (Melosh and Williams, 1989; Williams, 1990; Wallace and Melosh, 1994). Large earthquakes, e.g., the 1968 Tokachi-Oki quake, show tight coupling to about 50 km depth (Hasegawa et al., 1985). Thus, we suggest there is an increase in coupling between the subducting and overriding plates between 10 and 50 km (Fig. 2.9b). The horizontal displacement increment applied at the interplate boundary increases by a factor of two between 10 km and 50 km to simulate the compressional push from the subducting Pacific plate. The slab drag force along the boundary also increases by a factor of two. The average horizontal displacement increment is 1 mm/year, and the average vertical force is $3.75 \times 10^{10} \text{ N/m}$.

2.4.4 Model Discussion

2.4.4.1 Faulting

As the forces increase, we examine the grid to locate regions where the PTF exceeds 1.0 resulting in faulting. To parameterize the failure criterion, we used 1.05 kbar for the cohesion strength and 0.53 for the coefficient of internal friction (Handin, 1969). To save computational time, after calculating the number of time steps required to build up stresses to the failure level, we allow the fault to slip every multiple of this number.

There are two clear high horizontal, compressive stress concentration zones: one in the western coastal area, and the other near the volcanic front area at 1.8 Ma. (Fig. 2.10 a,b). In each zone, either of the two fault planes is likely to slip. We insert slippery nodes into the model in these regions. The dip of the fault is inferred from the observed active faults which are exposed at the earth's surface. Faults are located on both sides of the middle part of the Backbone range: the Senya thrust fault dipping to the east is at the west side of the range, and the Morioka thrust fault dipping to the west is located at the east side of the range. The 1896 Rikuu earthquake activated the Senya fault and the intermediate Kawafune fault (Fig. 2.1). On the western coastal plain, there are thrust faults dipping to the east, e.g., the Kitayuri Thrust (see Fig. 5.5 of Hashimoto, 1991).

In Figure 2.10b there is a highly compressive PTF region at about 575 km from the left-hand side and 20 km deep, and a near surface, highly tensional PTF region at about 600 km. These are artifacts of the model resulting from our simplified viscosity structure: the assumed abrupt change of viscosity from the inner arc to the outer arc as well as a sudden change of slope at 585 km and 22 km deep. Because the processes are thermally activated, the true model should have a more gradual transition in viscosity which would lower the stress concentration. To test the effect of a viscosity gradient on the PTF, we did a model run in which the viscosity of the deep zone (at 575 km, 20 km deep) in the wedge was set to the intermediate value of 2×10^{22} Pa s. The results are shown in the insert in Fig. 2.8b. Comparing the insert with the outlined region for the original model, one sees that this viscosity gradient reduces the magnitude of the PTF in both the deep and near-surface zones.

In a 3-D medium, if a fault slips and reduces the local stress to zero, stress is still transmitted around the fault, so that in the greater region, stress is reduced by an amount less than the total stress drop. We approximate this situation by allowing only a partial stress drop: 30% in the examples cited below. (The exact value was found to be non-critical.) Figure 2.9 shows the geometry of the faults that are introduced in the grid based on the above considerations.

2.4.4.2 Erosion and deposition

We model erosion and deposition by two constraints: erosion/deposition is directly proportional to the square of height/depth (Ohmori, 1978), and the volume of deposited material is matched to the erosion. The erosion rate in the model presented here is the rate obtained by Ohmori (1978): 0.3 mm/year for a height or depth of 1000 m. The erosional and depositional rates are taken to be the same on land and in the coastal area.

2.4.4.3 Time history

The size of the time step varies during a model run. The first period has 100 time steps with a step size of 0.15 year. (A small time step for the initial stage helps stabilize the solution.) The second period has 2000 steps each 600 years long, while the last 3100 steps have a step size of 1200 year. The total number of time steps is 5200, resulting in a total model run duration of about 5.0 Ma.

2.5 Results

We show results for three models with different viscosity structures under the same conditions of coupling, erosion and deposition, and loading. After presenting one of the models in detail (Model B), we compare the computed topography and gravity residual anomalies from each of the three models with the observed values.

2.5.1 Stress, topography, gravity, and fault slip

For the model with a 10 km effective elastic thickness in the inner arc (Fig. 2.9), the horizontal stress averaged over the plate thickness is plotted with respect to time in figure 2.12. Before the fault first slips, the horizontal stress at the inner arc is about 125 MPa. As the fault slips, the horizontal stress drops. The horizontal stress decreases with time, and levels out at about 30 MPa after 2 Ma.

Lithosphere beneath the Kitakami Range upwarped during the past 5 Ma leading to an elevation of about 1000 m (Fig. 2.13a). Displacement shown here is the vertical displacement. The amount of erosion at the Kitakami range is about one-third of the total displacement. The average rate of uplifting of the Kitakami range is 0.2 mm/year. The predicted gravity residual anomaly at the Kitakami range is about 70 mGal (Fig. 2.13b). The west coastal area has been a subsidence center during the past 5 Ma.

Figure 2.13 shows the effect of erosion and deposition. The elevations of the volcanic front and the Kitakami range are greatly reduced by erosion. Equal volumes of eroded material were deposited in the western coastal and the outer-arc trench slope.

The slip rate of the faults can also be obtained from the analysis. From our calculation, the slip rate of the west fault at the central Backbone range is about 0.2 mm/year.

2.5.2 Comparison with observed data

Our criterion is to fit both the topography and gravity data. Figure 2.15 shows comparisons for a range of models of crustal rheology (see fig. 2.14) with observed data. The model-data differences are in the crustal viscosity structure. For model A, the upper 5 km is purely elastic, and the viscosity below 5 km is 10^{19} Pa s, so the effective elastic thickness is 5 km. For model B, the upper 5 km is elastic, and the viscosity is 10^{24} Pa s from 5 km to 10 km, so the effective elastic thickness is 10 km. For model C, the upper 10 km is purely elastic, and the viscosity is 10^{22} Pa s from 10 km to 20 km, so the effective elastic thickness is greater than 10

km. The Japan Sea plate has a different composition and rheology structure; we focus in this study on only the lithospheric deformation from the west coast to the Japan trench. All three models with effective elastic thicknesses of 5, 10 or 10-20 km can be made to fit the topography data, but the 10 km thickness in model B best fits the gravity anomaly residual. The misfit in the elevation of the volcanic front may be due to a slight over-estimate of the Backbone boundary fault slip. However, the elevation of the volcanic front is quite variable, as can be seen from figure 2.1, and the calculated height matches quite well in the adjacent regions. The upper bound of the viscosity for the lower crust (10-20 km) is about 10^{22} Pa s (Fig. 2.15). We conclude that the upper crust has an elastic thickness of about 10 km overlying a lower crust with a viscosity of 10^{22} Pa s or less.

2.5.3 Discussion

Based on the model fits between the calculated and observed topography and gravity residual anomaly, we conclude that the upper crust has an elastic thickness of about 10 km overlying a lower crust with a viscosity of 10^{22} Pa s or less. As discussed above, based on thermal considerations there is probably no discontinuity in viscosity but rather a gradual transition over a few kilometers.

The thickening of the high viscosity zone trenchward of the volcanoes as well as the increased coupling at the interface has a significant effect on the amount of warping and the stress concentration at the volcanic front. In particular, increasing coupling with depth enhances the uplift of the Kitakami range. These mountains are still uplifting at the present time (Fig. 2.2 and Sugimura and Uyeda, 1973). Note that coupling is defined here as the interaction between the subducting plate and the overriding plate. It is not a measure of interplate seismic efficiency, which depends in addition on fault rheology. For a more comprehensive analysis of coupling, see Chapter 3 (Huang et al., 1996).

Matsuda et al. (1980) reported that the maximum vertical displacement along the 1896 Rikku earthquake faults was about 3.5 m. No strike-slip component was observed. They argued that at least one event similar to the 1896 event had occurred in Holocene period because the vertical displacement observed on the present alluvial fan is greater than 3.5 m. They estimated that the average rate of vertical displacement during the last 23,000 year is about 0.2-0.3 mm/year, the same result obtained from our modeling.

Erosion/deposition alters significantly the topography and gravity (Fig. 2.13). Having an erosion rate proportional to the square of elevation change (Ohmori, 1978) as well as a balance between erosion and deposition is probably reasonable, but deposition is necessarily more complicated. Sediment can be deposited in large quantities in a relatively shallow depression if it is in proximity to an eroding source. In our modeling, the sediment distribution is therefore rather approximate. Even so, with an erosion rate of 0.32 mm/year, as suggested by Ohmori (1978), the calculated topography and gravity at 5.0 Ma agree well with the observed topography and gravity (Fig. 2.13).

The short-term interaction between the subducting Pacific plate and the overriding plate can be inferred from present-day seismic activity along the interface. However, long-term coupling along the interplate boundary must be inferred from the gravity and topography data. Gravity and

topography depend upon the stress level in the overriding plate, which in turn provides constraints on the long-term interaction between the subducting plate and the overriding plate.

2.6 Conclusions

A simple elastic/viscoelastic model, subjected to stresses from the subducting oceanic plate, and allowing for faults, volcanic flux, erosion and deposition, is able to reproduce the topography, gravity and seismicity of the Tohoku region in northeast Japan.

From our modeling, the long-term (million of years) effective elastic thickness of the crust is found to be about 10 km in the inner arc increasing to about 50 km nearer the Japan trench. The lateral change of the effective elastic thickness is an important factor controlling the lithospheric deformation. The viscosity of the lower crust is on the order of 10^{22} Pa s or less (Fig. 2.15).

In general, the main factors controlling the deformation of the northeast Japan lithosphere for the last 5 million years are: 1) viscosity structure; 2) coupling at the interplate interface; and 3) erosion and deposition.

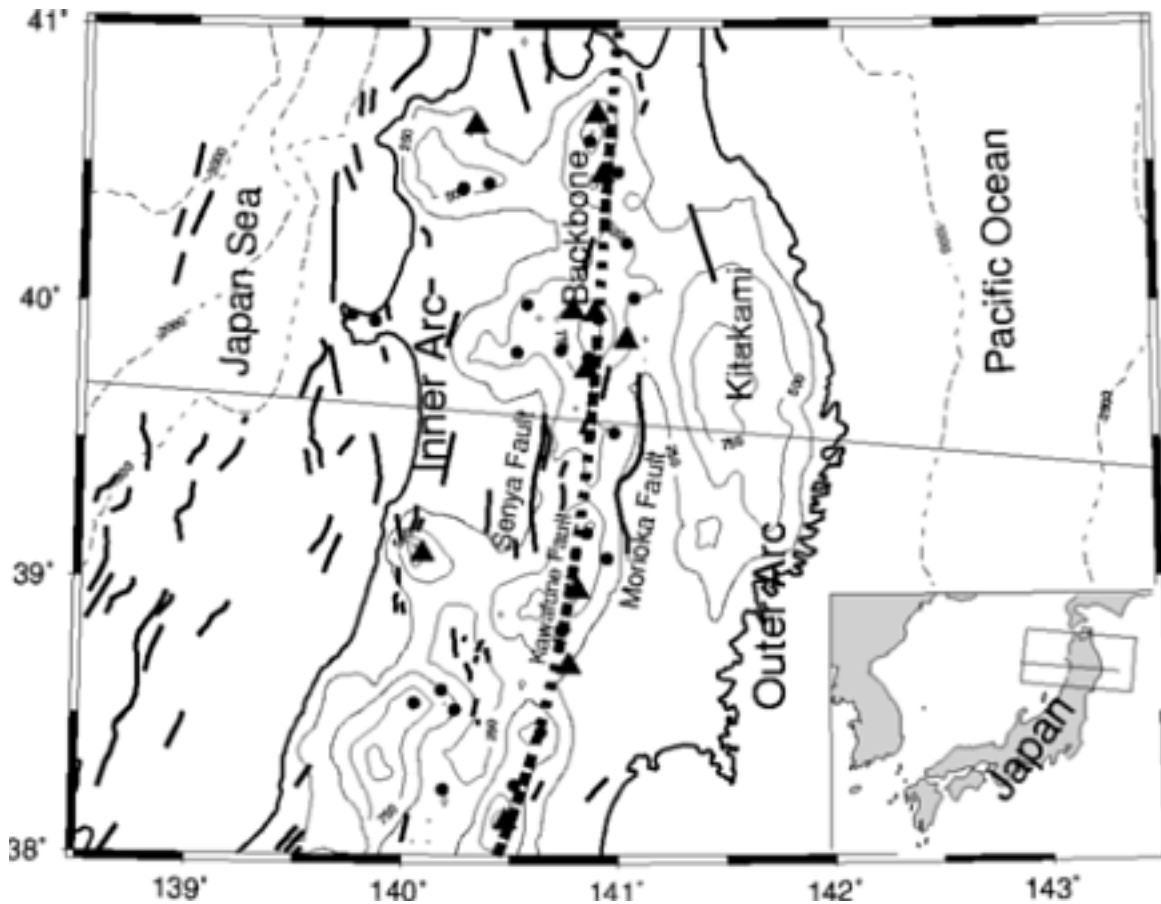


Figure 2.1: Map of the study area in northeast Japan. The central mountain (the Backbone range) runs about N-S. The volcanic front is located approximately in the middle of the Backbone Range. The solid triangles are the active volcanoes. The solid dots represent other Quaternary volcanoes. The thick dashed line indicates the volcanic front. The solid lines are the active faults. The Senya fault and the Morioka fault are located at the west and east sides of the central Backbone range, respectively. The Senya thrust fault and the Kawafune fault were activated during the 1896 Rikuu earthquake. Locations of faults and volcanoes come from the Research Group for Active Faults of Japan (1991). Bathymetry contour intervals are 1,000 m, and elevation contour intervals are 250 m. The inset shows the location of Japan. The study area is outlined by heavy lines, and the thin line indicates the location of the geophysical cross section (Fig. 4).

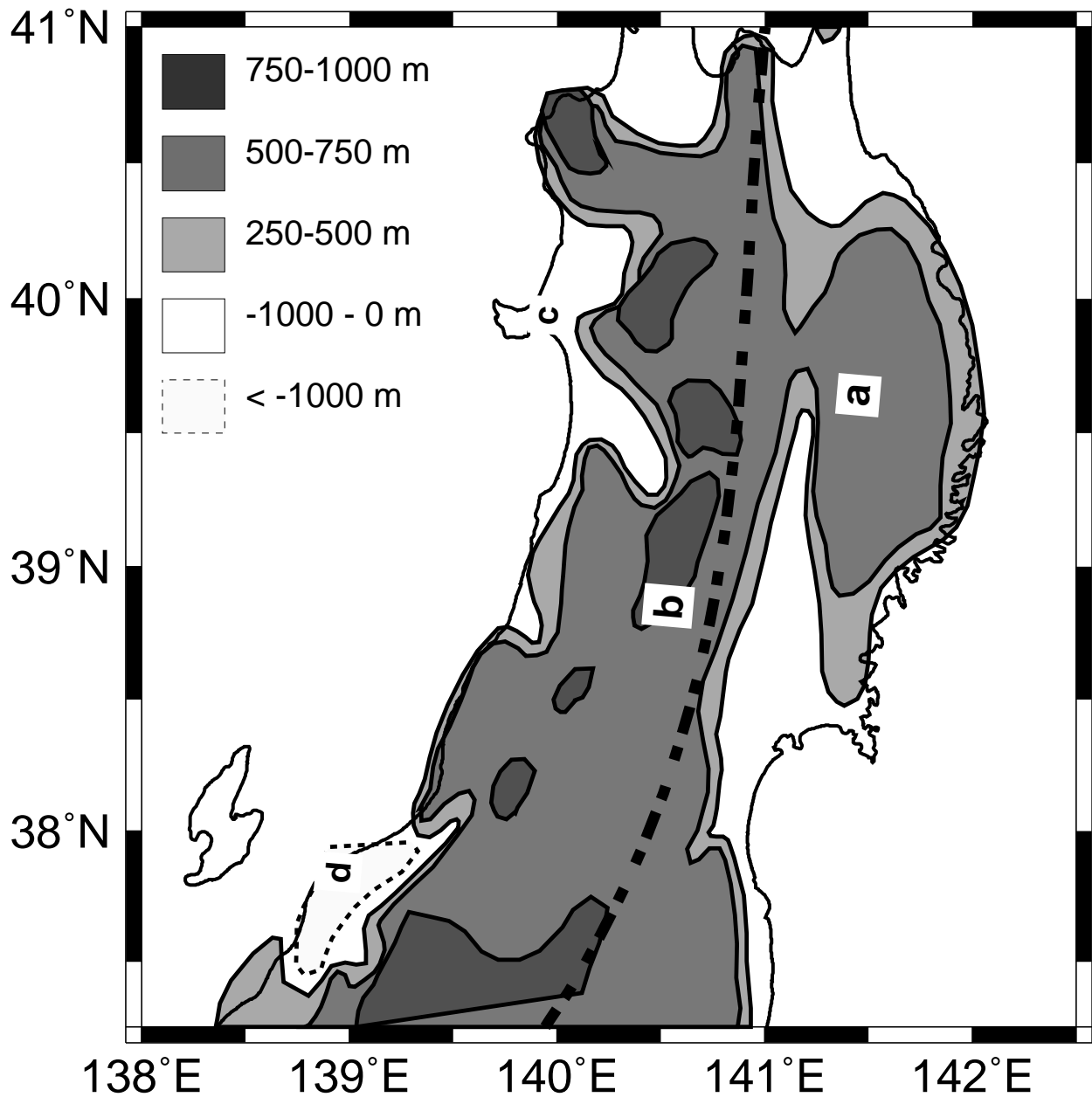


Figure 2.2: Amount of uplift/subsidence during the Quaternary period in northeast Japan (Sugimura and Uyeda, 1973). The Kitakami range (a), and the Backbone range (b) are two major uplift regions. Subsidence occurs in the western coastal area, e.g., the Akita basin (c) and the Niigata basin (d). The dash-dot line is the volcanic front.

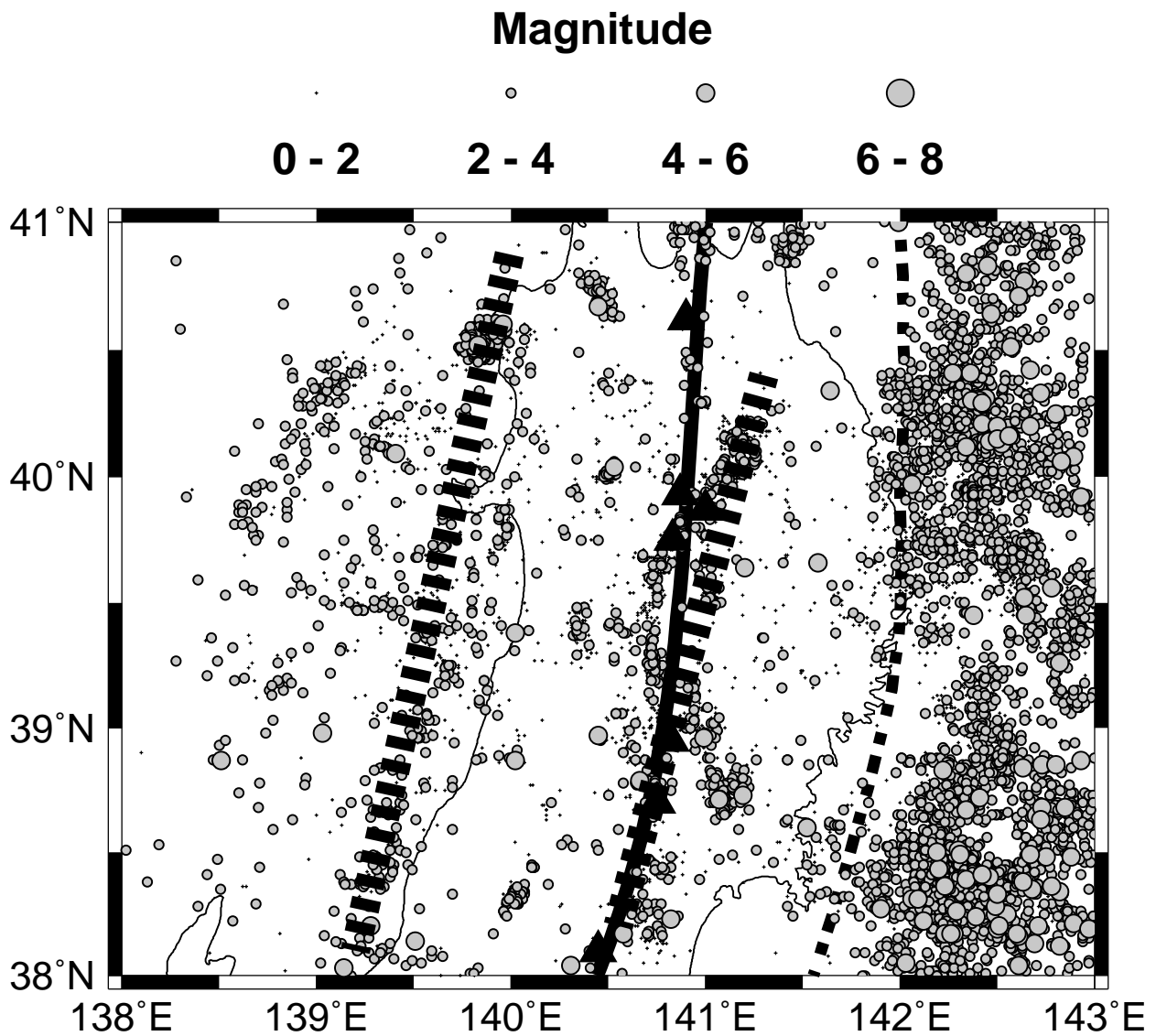


Figure 2.3: Shallow seismicity (<40,km) in northeastern Japan from 1975 to 1982 (after Rydelek and Sacks, 1990). There are two shallow seismicity concentration zones (indicated by thick dashed lines) striking about N-S in northeast Japan: one in the middle of the island, and the other in the western coastal area. The western coastal area has a diffuse distribution of seismicity due to the numerous faults (see Fig. 1). The solid line is the volcanic front. Triangles denote locations of active volcanoes. The dashed line denotes the aseismic front.

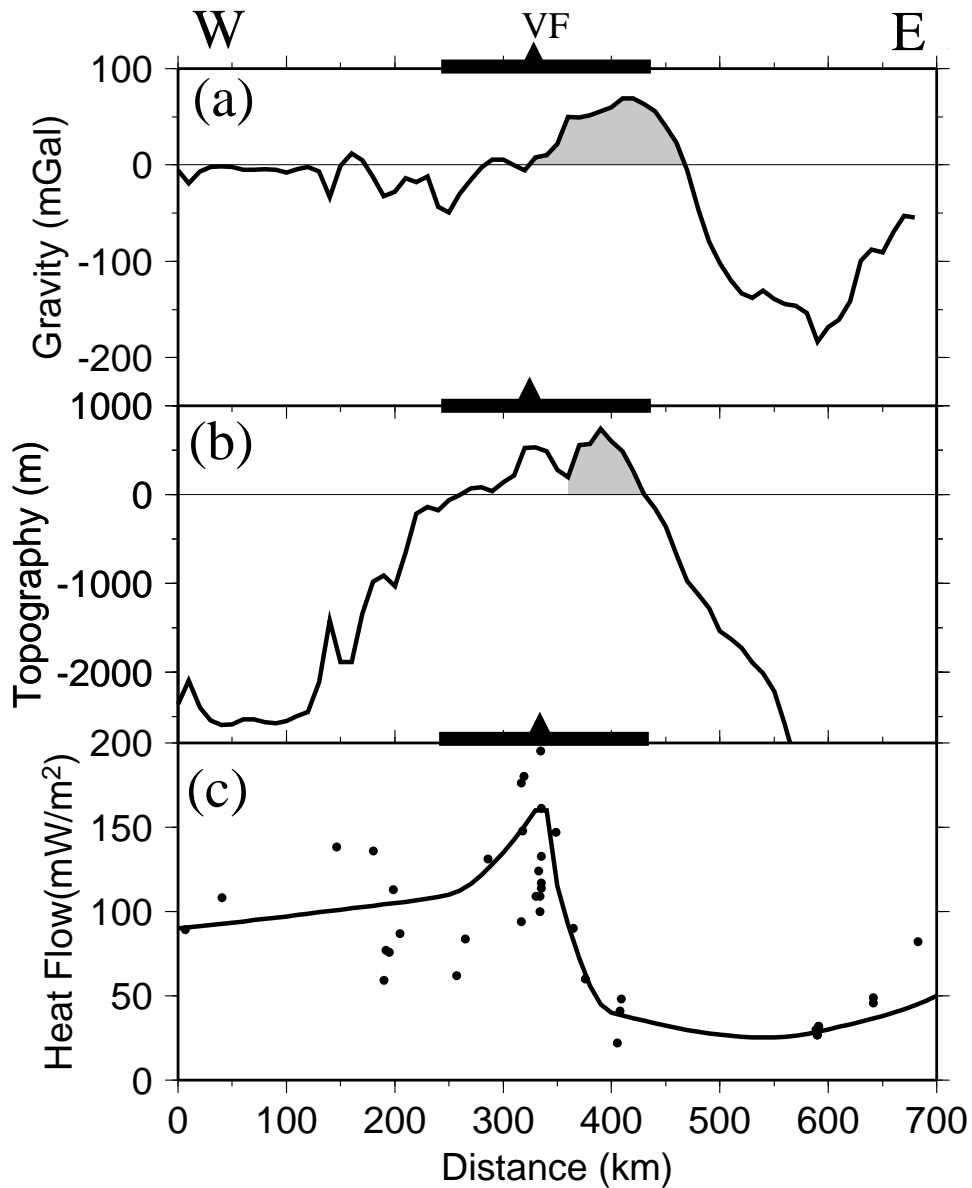


Figure 2.4: Profiles of (a) gravity residual anomaly, (b) topography, and (c) heat flow in northeast Japan. See Figure 2.1 for the location. The projection width is ± 10 km along the profile for the gravity and topography, and ± 100 km for the heat flow. The heat flow data are taken from Pollack, et al. (1993). The gravity residual anomaly comes from Bouguer gravity after correction for the dense subducting plate, and the isostatic gravity assuming an Airy isostatic compensation. The shaded areas highlight topography and gravity in the Kitakami range. **VF** is the Quaternary volcanic front.

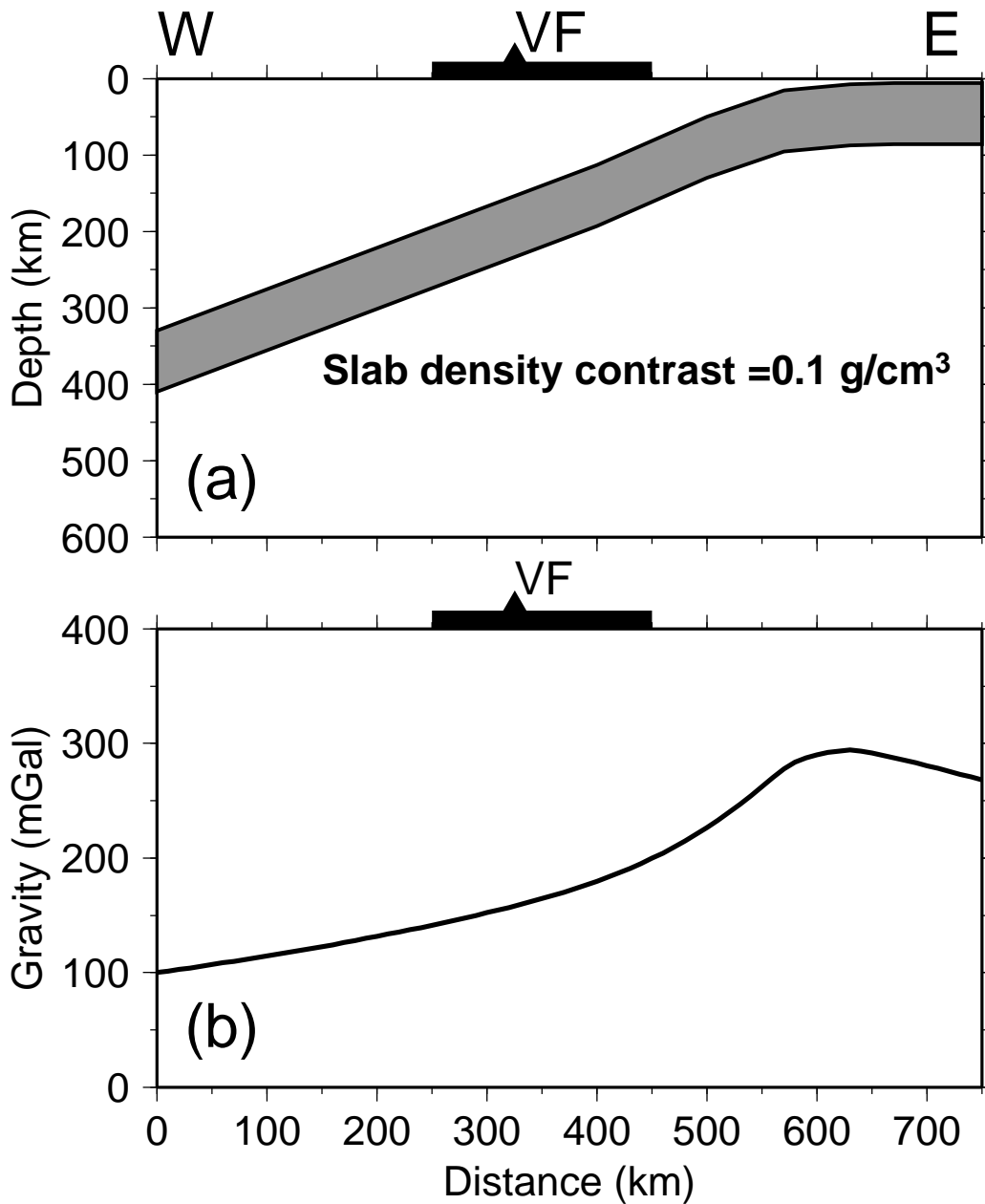
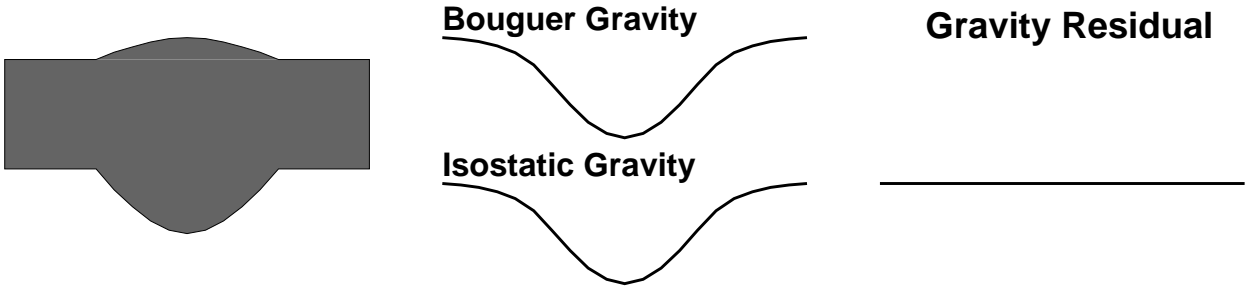


Figure 2.5: The gravitational effect of a dense subducting plate. (a) Geometry of the subducting Pacific plate inferred from seismic studies (Zhao et al., 1994). (b) The gravity signature from the subducting plate. The subducting Pacific plate has a higher density than the overriding plate, which yields a westward tilting positive gravity anomaly. The gravity effect at the trench is about 300 mGal. **VF** denotes the volcanic front.

a) Airy Isostatic Compensation



b) Buckling

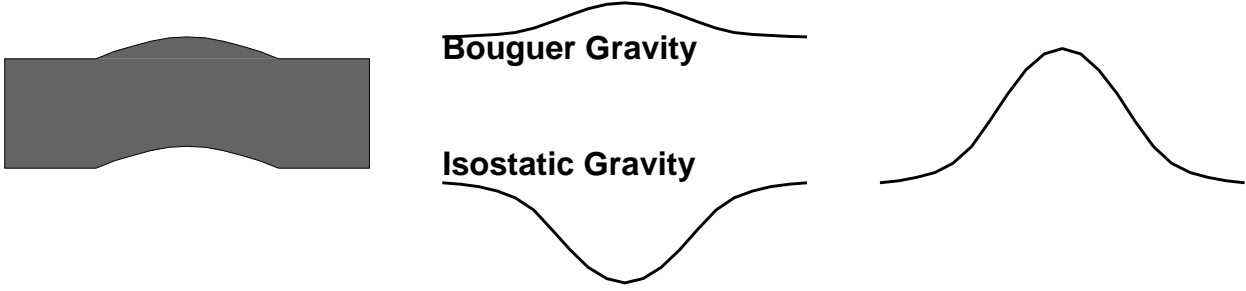


Figure 2.6: Schematic diagrams to illustrate Bouguer gravity, isostatic gravity, and gravity residual of a mountain in two end-member cases: a) Topography is Airy isostatically compensated, giving a negative, and identical Bouguer gravity and isostatic gravity. The gravity residual is therefore zero throughout the region. b) The crust folds due to horizontal compression, so the Bouguer gravity and gravity residual are both positive.

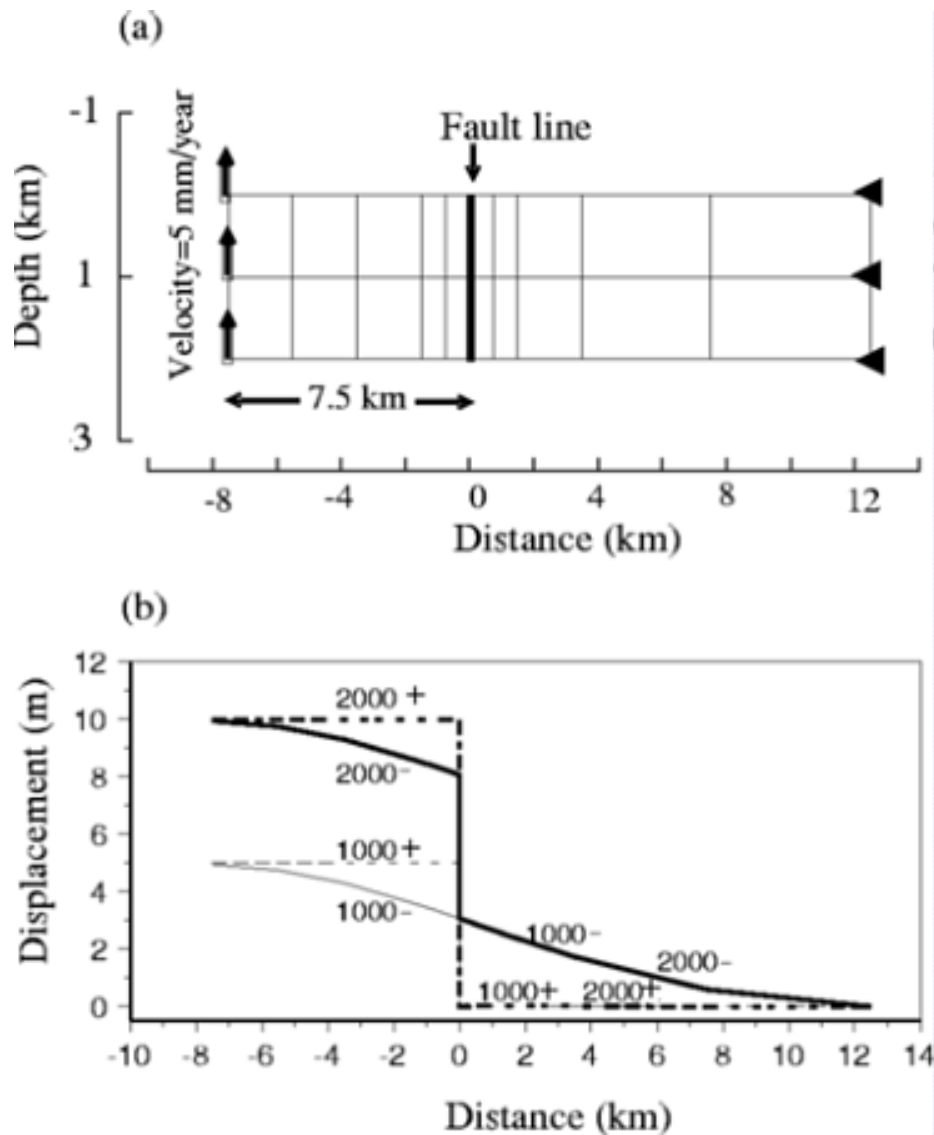


Figure 2.7: A stick-slip faulting test: a) The FEM grid. The plate is 20 km long and 2 km thick. The fault is 7.5 km from the left edge, and the fault plane is vertical. b) Displacement before (solid line) and after (dashed) fault slipping. After 1000 years, friction along the fault is overcome, and the fault slips. The amount of the first slip is 5 m. This reproduced the analytical solution by Turcotte and Schubert (1980). The stress drop is 100%. After the slip, the fault is immediately locked. After another 1000 years (at 2000 years), stress has built up to the level allowing fault slipping again. The fault slips 5 m again, thus the accumulated slip between the left wall and the right wall is 10 m after 2000 years.

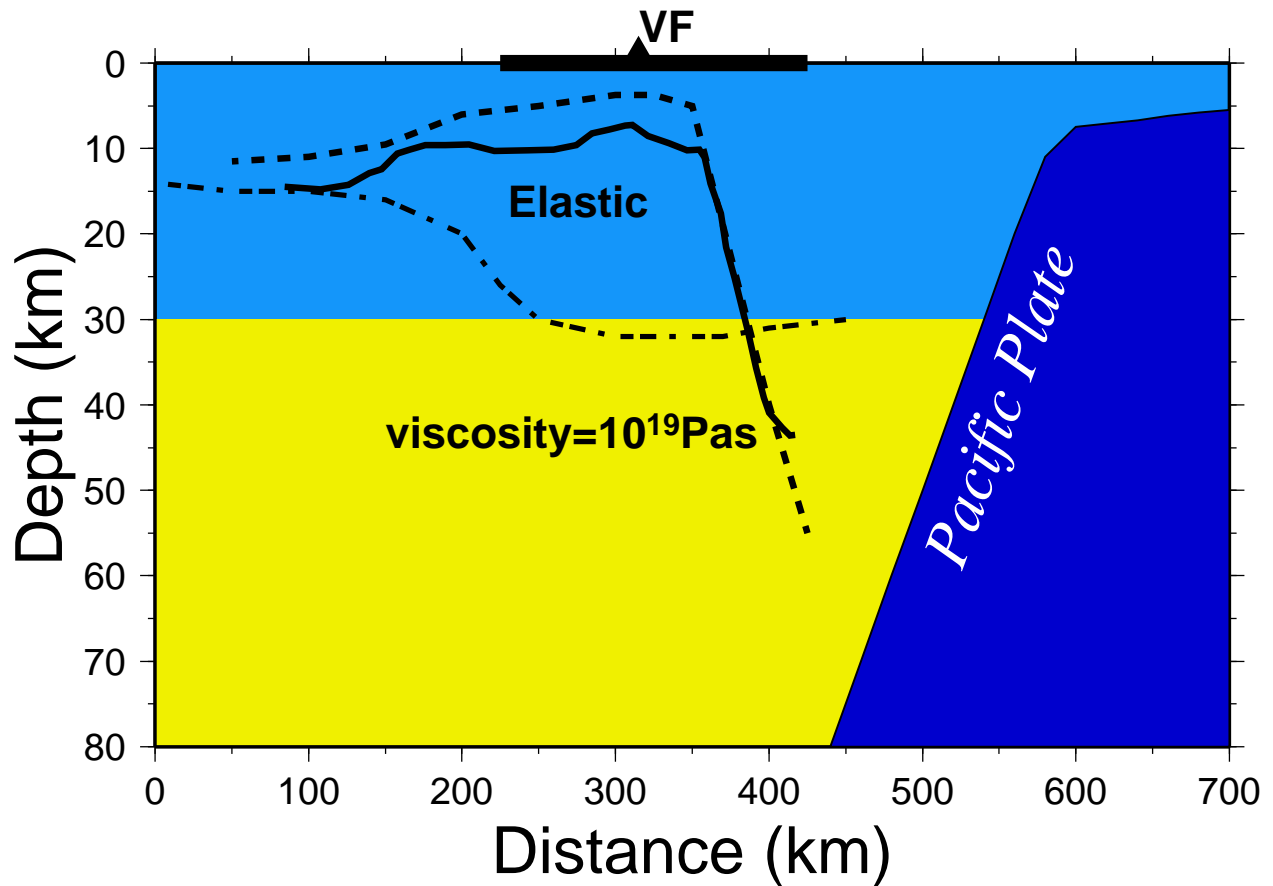


Figure 2.8: Starting model for the finite element analysis: the depth of brittle/ductile transition (dashed line), the Curie depth (solid line), crustal thickness (dashed-dot line), as well as viscosity of the mantle. The Curie depth is taken to be the isotherm of 450°C in the inner arc (Okubo et al., 1989, 1991), and this is assumed to be the effective elastic thickness of the continental lithosphere (Watts, 1992). The depth of the brittle-ductile transition comes from the lithospheric strength profile derived from heat flow data and the laboratory-based flow laws.

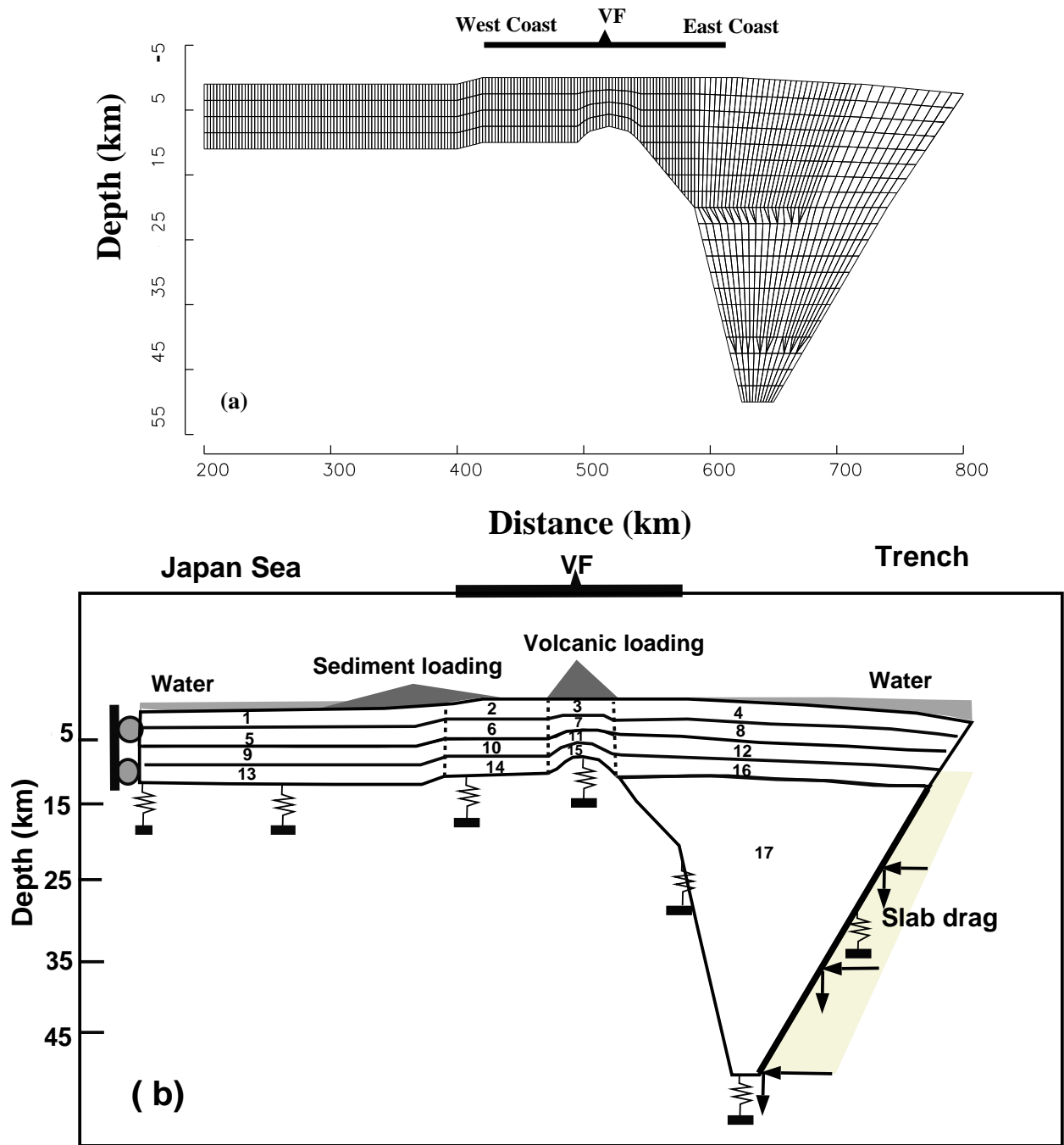


Figure 2.9: a) The FEM grid. b) Material properties and boundary conditions (see text and table 2.1).

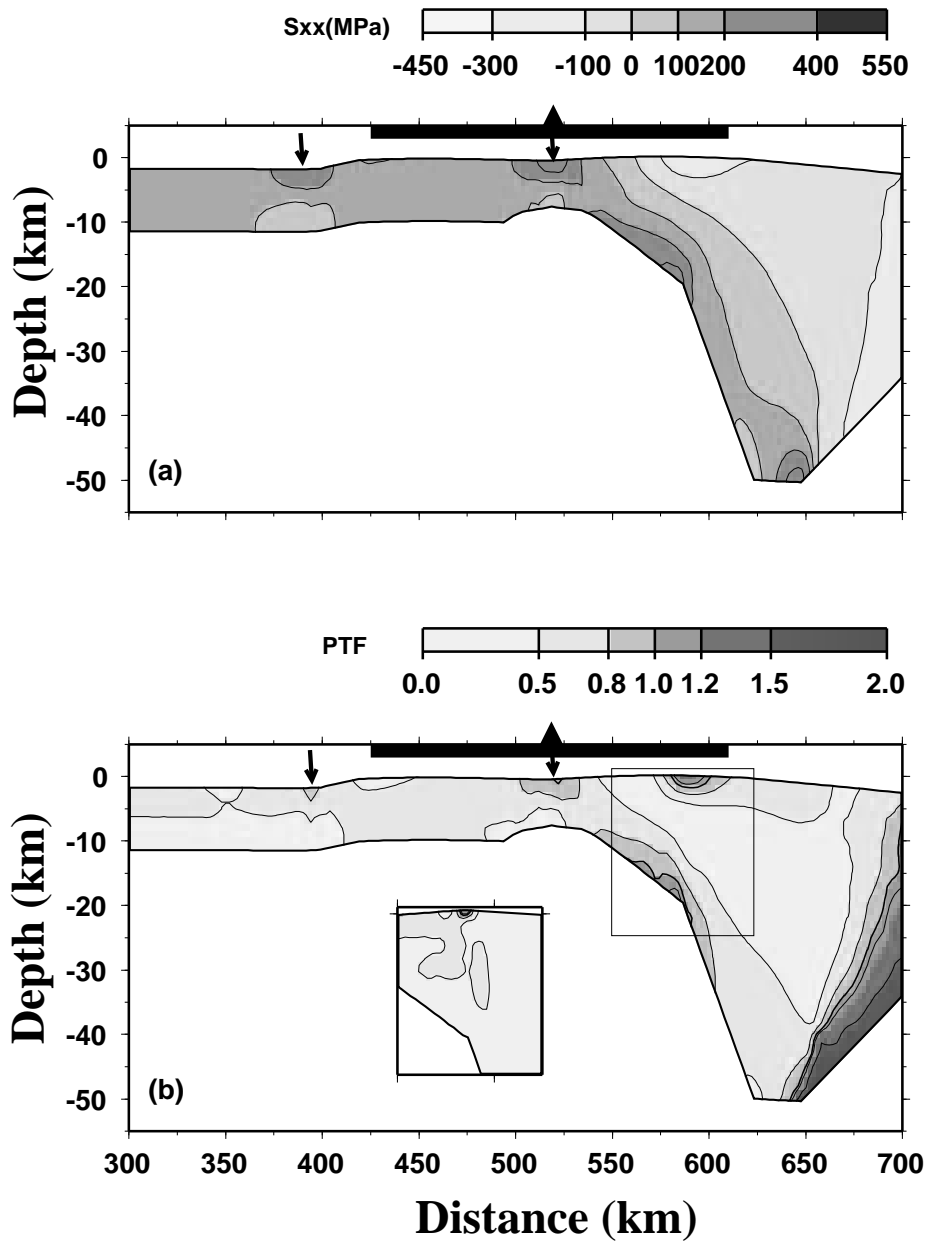


Figure 2.10: a) Horizontal stress at 1.8Ma, just before faulting. b) Proximity to failure (PTF) at the same time. The horizontal stress and PTF are both highest at the western coast and near the volcanic front (indicated by arrows). The insert in Fig. 8b shows the effect on the PTF of using an intermediate value for the viscosity in the deeper parts of the wedge. See text for further details.

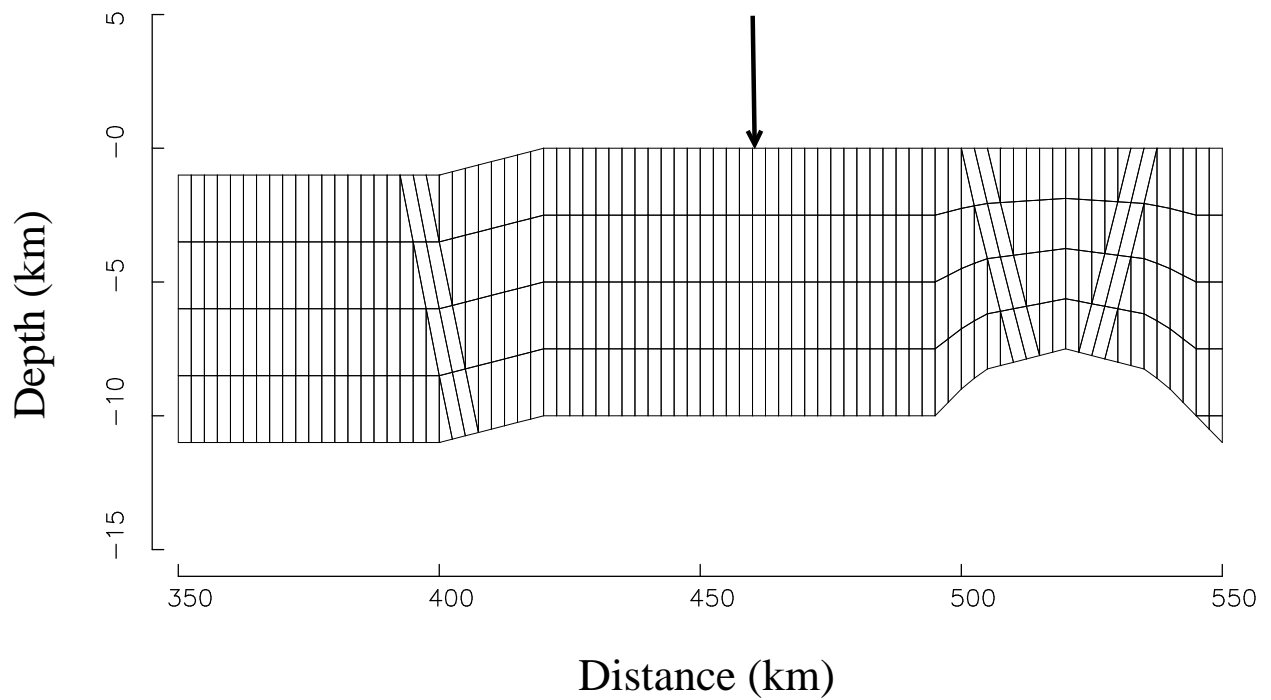


Figure 2.11: Orientation of the faults in the model. All faults cut through the plate. Fault dips are determined from the faults exposed on the earth surface. The arrow shows the reference point for the measure of the average horizontal stress shown in Figure 2.10.

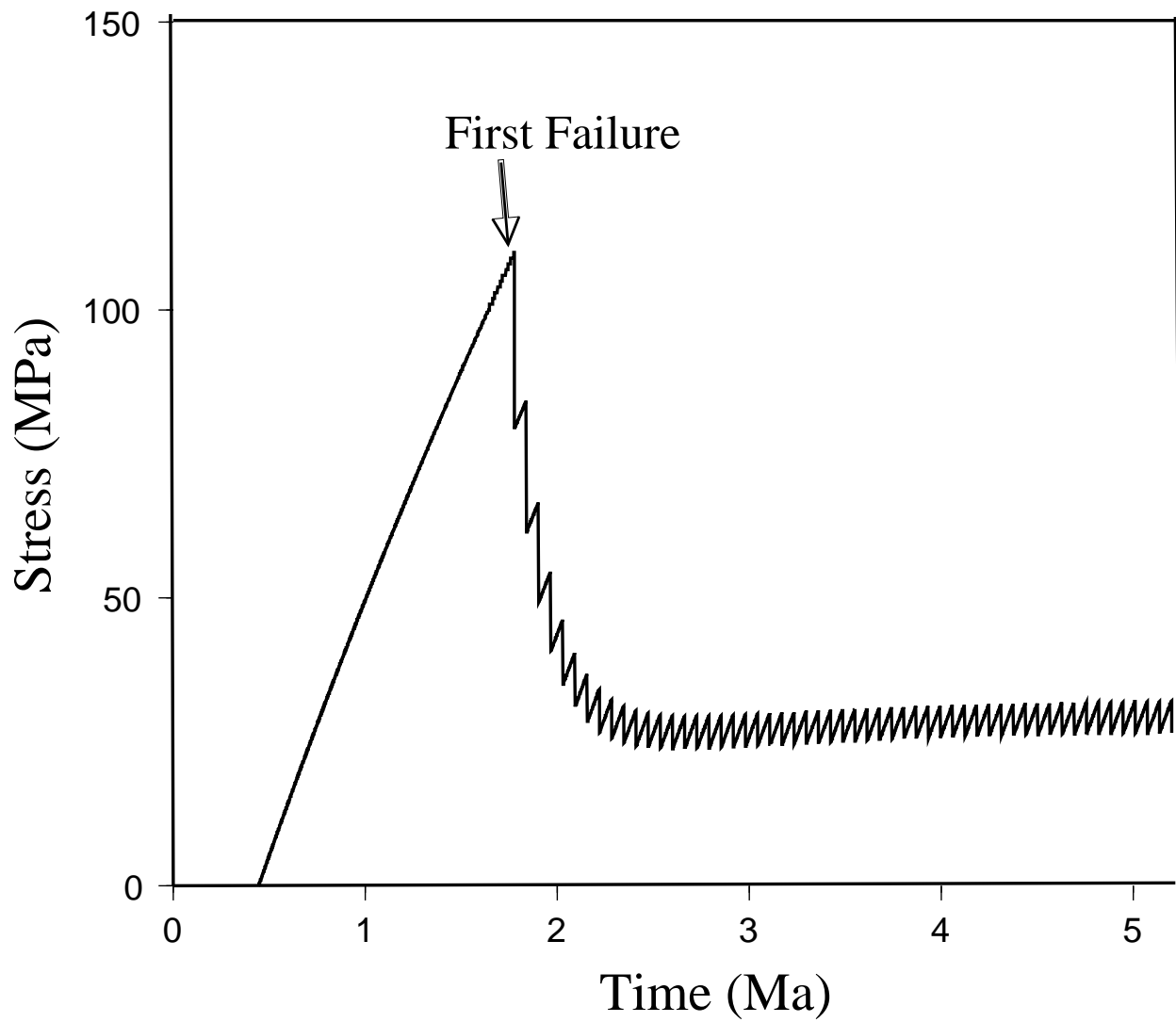


Figure 2.12: Horizontal stress averaged along the plate thickness versus time at the location between the western coast and the volcanic front shown by the arrow in Figure 2.11. The sawtooth pattern is caused by the sticky-slip faulting.

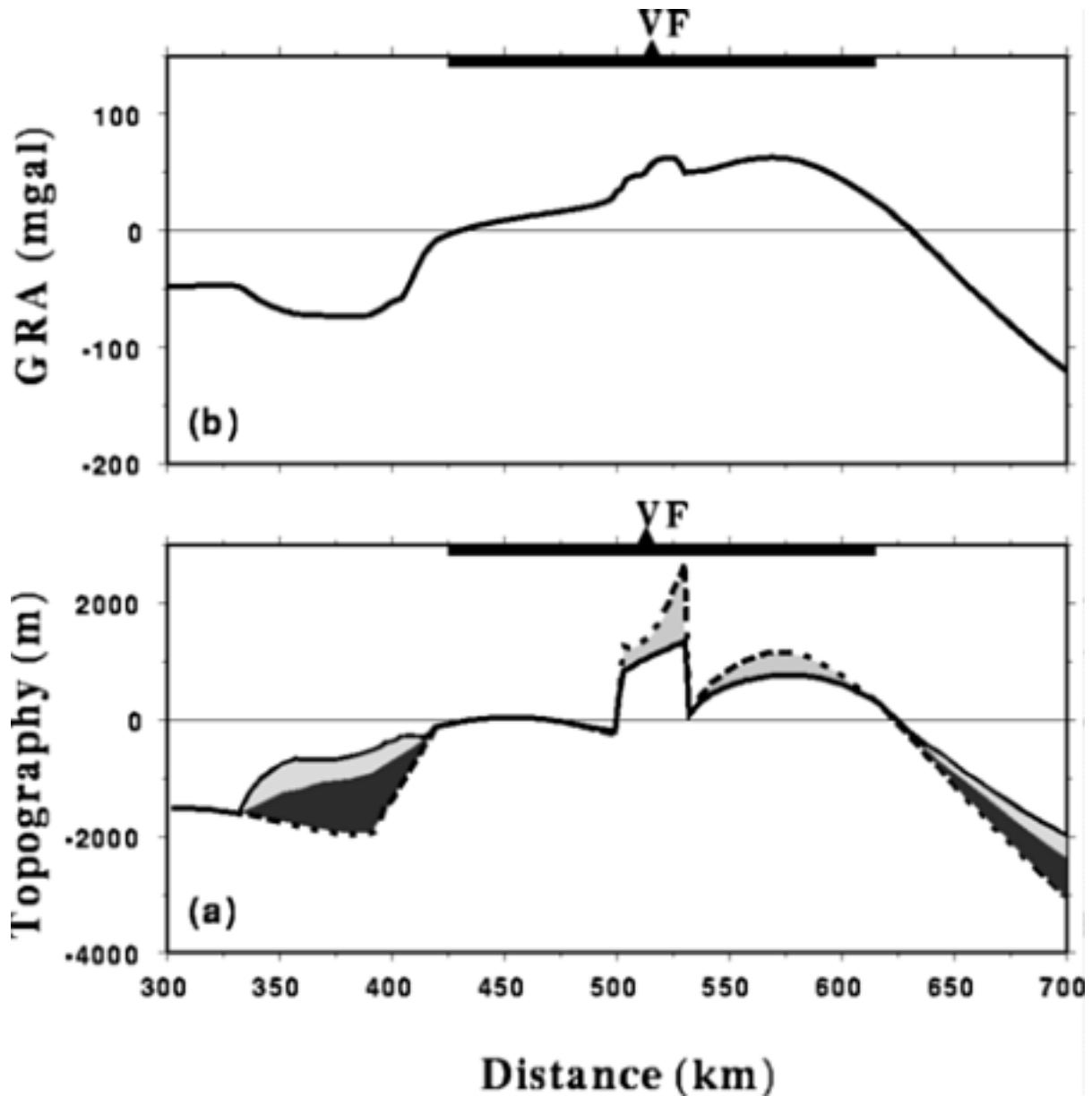


Figure 2.13: Calculated topography and gravity residual anomaly of the model in Figure 2.7 as well as model B of Figure 2.12. a) topography after 5.0 Ma. The dashed line is the accumulated displacement. The solid line indicates resulting surface topography after erosion/deposition. b) gravity residual anomaly after 5.0 Ma. Dark-gray shading indicates previous sedimentary loading. Medium-gray shading denotes the amount of erosion. Light-gray shading represents the amount of sedimentation.

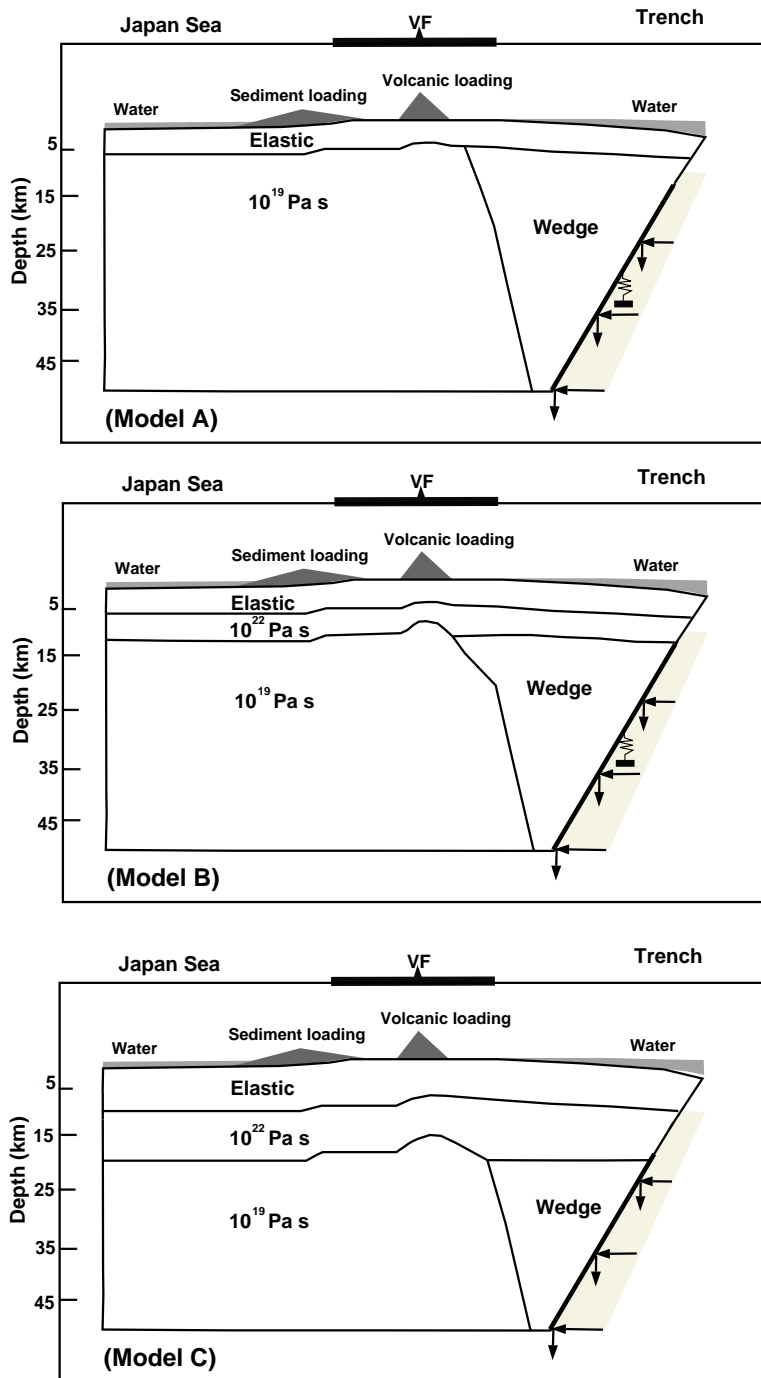


Figure 2.14: Three models with different thickness of the elastic lithosphere. The lower crust has a viscosity of 10^{22} Pa s. The mantle wedge has a viscosity of 2.5×10^{24} Pa s. The boundary conditions are the same for all models.

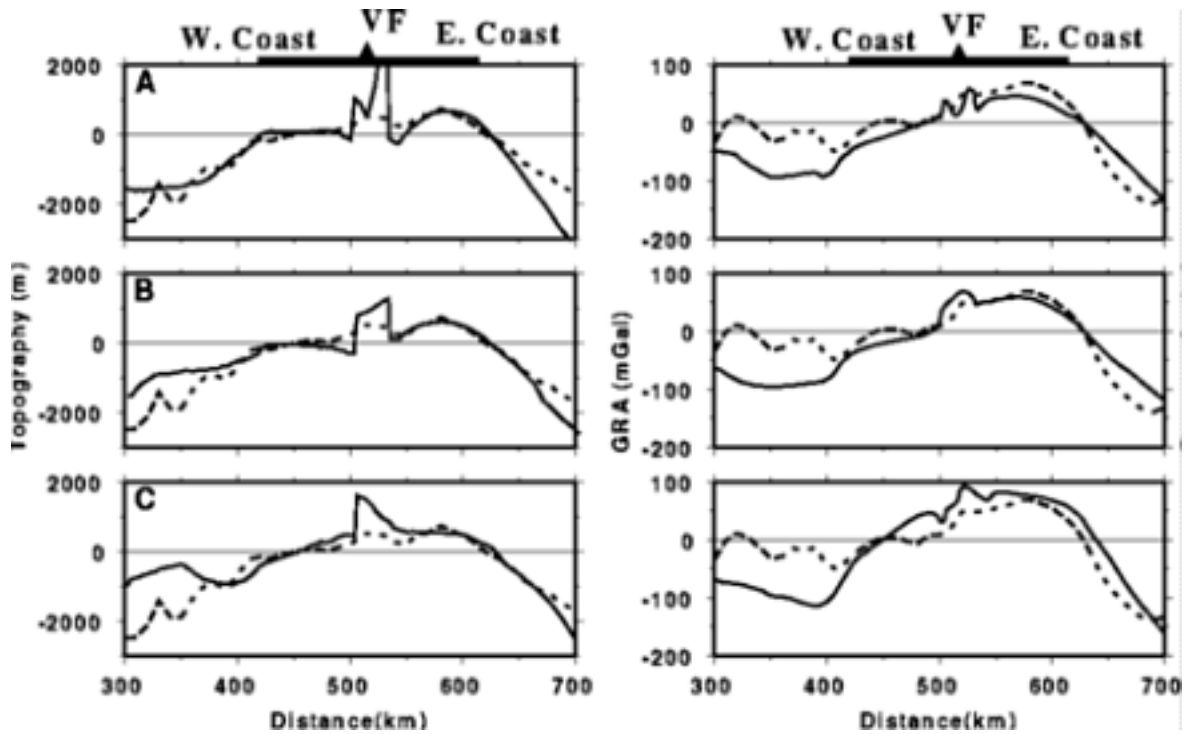


Figure 2.15: Comparison of topography (left) and gravity residual anomaly (right) with observations among three viscosity structures: (A) topography and gravity residual anomaly for a 5 km elastic upper crust and a lower crust (5–10 km) with a viscosity of 10^{19} Pa s; (B) topography and gravity residual anomaly for a 5 km elastic upper crust and a lower crust (5–10 km) with a viscosity of 10^{24} Pa s; (C) topography and gravity residual anomaly for a 10 km elastic upper crust and a lower crust (10–20 km) with a viscosity of 10^{22} Pa s. The dashed line is the observed value. The solid line is the calculated value. Comparisons were focused on the region from the western coast to the Japan trench, distances 400 km to 700 km.

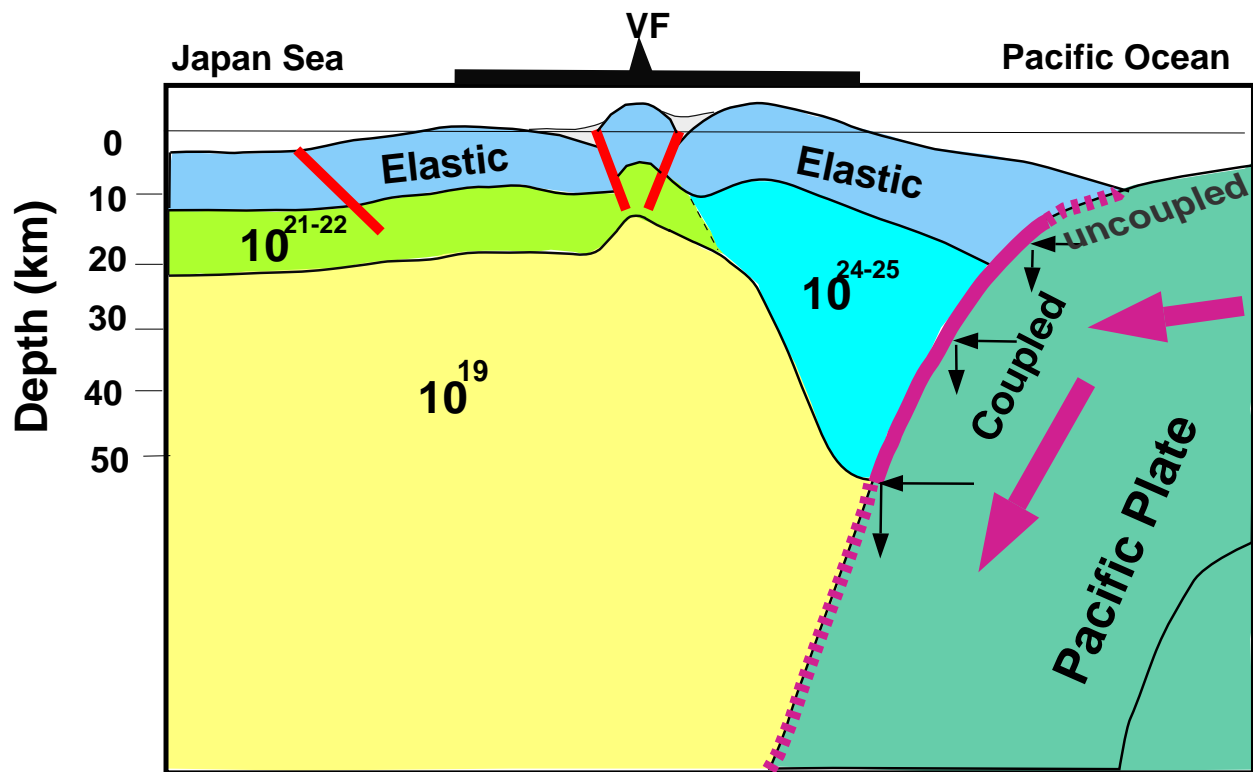


Figure 2.16: A schematic rheological structure of the lithosphere in northeast Japan derived from the finite element modeling. The interface between the subducting plate and the overriding plate is decoupled for the upper 10 km (dashed line). Increasing the coupling with depth by a factor of two plays an important role in the building of the Kitakami range. The effective elastic thickness is 10 km in the inner arc and increases to 50 km near the trench. The lower crust in the inner arc has a viscosity of 10^{22} Pa s or less.

Chapter 3: Topographic and Seismic Effects of Long-Term Coupling Between the Subducting and Overriding Plates Beneath Northeast Japan

3.1. Introduction

Northeast Japan is in a tectonic setting in which the motion of the subducting Pacific plate has been in a direction approximately perpendicular to the strike of the Island for at least the past five million years. As a result, compressional deformation dominates during this period (Sato, 1994; Matsuda et al., 1967; Hashimoto, 1991). Northeast Japan is moving landward at 0.93 cm/yr along an azimuth of 320 degrees (table 1 in Scholz and Campos, 1995).

The volcanic front divides the northeast Japan island arc into two regions striking near N-S: an inner arc in the west and an outer arc in the east (Fig. 3.1). The outer arc includes the Kitakami range and the Abukuma range, while the inner arc extends from the central Backbone range to the Japan Sea coast. The central Backbone range runs approximately north-south through the region, and includes the Quaternary volcanic front. The western coast and the adjacent Japan sea have numerous Quaternary thrust faults, all subparallel to the strike of the Japan trench. The aseismic front is along the eastern coast, and it is taken to be the landward limit of the seismicity from the mantle wedge apex above the subducting plate (Yoshii, 1979). We consider three regions: off Sanriku to the north (Region 1), off Miyagi (Region 2), and off Fukushima (Region 3) to the south. (See Fig. 3.1.)

Interplate and intraplate earthquakes define the geometry of the subducting plate. It has been observed that the occurrence of the interplate thrust-type earthquakes are not uniform along the strike of the Japan trench. There are more great ($M > 7.5$) thrust earthquakes off the Pacific coast in region 1 (off Sanriku) than in region 2 (off Miyagi and off Fukushima) of northeast Japan (Hasegawa et al., 1983, 1985, 1994; Kawakatsu and Seno, 1983). The aftershock area is also larger in region 1 (Fig. 3.2). The lower bound of the seismogenic thrust zone is at a depth of about 50-60 km beneath northeast Japan (Fig. 3.2).

The number and size of interplate thrust-type earthquakes presumably depend on the strength of coupling between the subducting and overriding plates. This paper focuses on a quantitative analysis of differences in the degree of coupling in the different zones.

3.2. Coupling

Coupling is defined here as the interaction between the subducting and overriding plates. The external tectonic forces can be resolved at the interplate interface into horizontal and vertical components. (See Fig. 3.3.)

Finite element modeling of short-term (decades) coupling in the Japan Island has been done by Shimazaki (1974), Hashimoto (1981, 1984, 1985), and Sato (1988). Shimazaki (1974) used the finite element method to analyze relationships between the strength of coupling and pre-seismic crustal movements in Hokaido Japan during the period from 1900 to 1955. Shimazaki concluded

that at depths shallower than 23 km there is effectively no coupling, and from 23-90 km the coupling is strong. Sato (1988) modeled 3-D fields of stress and displacement in the southern and northern regions of northeast Japan for the past 60 years assuming three different modes of coupling: uniform, increasing with depth, and decreasing with depth. In Sato's model, the depth range for coupling is from the trench axis to the depth directly beneath the aseismic front, and a normalized coupling factor (seismic coupling factor) is used to define the strength. In a series of papers on kinematic dislocation models (Matsu'ura and Sato, 1989; Sato and Matsu'ura, 1988, 1992, 1993), the drag force from the subducting oceanic plate was implemented as an increase of displacement discontinuity along the intraplate interface, and a "coupling degree" was specified to take into account the strength of coupling between the two plates. Sato and Matsu'ura also considered the effect of erosion/deposition, as well as accretion of oceanic sediments, in their analyses of both short-term and long-term crustal deformation in northeast and southwest Japan.

We assume that the lower boundary of the coupled zone is defined by the deepest extent of large, interplate, thrust-type earthquakes ($M > 7$), which is shallower than about 50 km in northeast Japan (Hasegawa et al., 1983, 1994). It has long been recognized that there is a shallow earthquake-free zone parallel to the Japan trench axis extending from the axis to some depth (Byrne et al., 1988; Kawakatsu and Seno, 1983). This aseismic zone has been explained as resulting from high fluid pressure and water subducted with the Pacific plate (Huene et al., 1989, 1994; Wang, 1980; Byrne et al., 1988). From a recent study using a network of ocean bottom seismometers, Suyehiro and Nishizawa (1994) found that the earthquake-free zone ends at a depth of about 10 km. Thus, interplate earthquakes appear to be confined to the depth range 10-50 km (Fig. 3.2).

3.3. Basic modeling concepts

These concepts are described in detail in Chapter 2. Here we give only a brief overview.

3.3.1 Modeling approach

Because the strike of folds and faults in northeast Japan is approximately perpendicular to the direction of subduction, a 2-D plane-strain finite element analysis suffices to define the mechanical behavior of the lithosphere assuming a realistic rheology and boundary conditions. We have adapted the finite element code TECTON (Melosh and Raefsky, 1980; Wallace and Melosh, 1994) to analyze the deformation of folding and faulting of island arc lithosphere resulting from long-term compressional forces and slab drag using an appropriate rheological structure and faults. We modified TECTON (v5.2) to incorporate a simulation of stick-slip faulting, erosion and deposition as well as time-dependent loading. This allows us to monitor the long term deformation of the island-arc lithosphere with forces resulting from the subduction of the Pacific plate as well as from the surface processes of erosion and deposition. A critical requirement we apply in our modeling is consistency with observed, present-day topography and gravity.

A starting model was built based on the published estimates of crustal thickness, Curie depth, viscosity from heat flow analysis, as well as other estimates of viscosity structure (Zhao et al., 1994, Okuba, et al., 1989, 1991, 1994; Rydelek and Sacks, 1988, 1990; Huang et al., 1996).

Several lithospheric rheologies have been explored to explain flexural behavior: elastic, viscoelastic, and plastic (Turcotte and Schubert, 1982; Martinod and Davy, 1992; Lambeck 1983). In our modeling, the stress changes are over a very wide period range because we include earthquake induced faulting. We therefore assume a linear Maxwell visco-elastic rheology. We vary the viscosity structure and the interplate coupling to optimize the model fit to the observed topography, gravity, and seismicity patterns.

3.3.2 Stick-slip faulting

Repeated earthquake faulting must be incorporated in our modeling because it can contribute to the growth of geological structures over the long term (King et al., 1988). A description of the slippery-node method to simulate faulting was given by Melosh and Williams (1989). The location of faults and the amount of slipping are controlled by the stress field and the Mohr-Coulomb criterion. The proximity to failure (PTF) is the ratio of the observed maximum differential stress to the maximum differential stress predicted by the Mohr-Coulomb criterion. The fault slips whenever the PTF is greater than 1.0. TECTON was modified to model stick-slip faulting, and to minimize numerical errors resulting from large displacements associated with slipping.

3.3.3 Erosion and deposition

Tests show that the expected amount of rearrangement of surface mass by erosion and deposition has a significant effect on the displacement field and stress state of the deformable lithosphere. Ohmori (1978) showed that the erosion rate of mountain ranges in Japan is in proportion to the square of land height and is about 0.3 mm/year at the elevation of 1000 m. Therefore, in 5 Ma about 1.5 km of material would be removed from the volcanic front and the Kitakami range, so erosion and deposition must be modeled. We modified and implemented in TECTON the scheme of erosion and deposition developed by T. Sato & M. Matsu'ura (1992, 1993). Erosion and deposition modify both the surface topography, and also the loading and unloading of the lithosphere.

3.4 Geophysical Data in northeast Japan

There are sharp contrasts among the three regions of study (Fig. 3.1). Region 1 has high topography, a high gravity residual anomaly (GRA), and active seismicity; region 2 has low topography, a low GRA, and weak seismicity; and region 3 has moderately high topography, a moderate GRA and weak seismicity.

3.4.1 Earthquakes

Interplate Earthquakes: The occurrence of large interplate earthquakes changes from the north to south. 38°N is approximately the southern boundary for observed great ($M > 8$) earthquakes

(Hasegawa, et al., 1983). The aftershock area is also larger in region 1 than in regions 2 or 3 (Fig. 3.2).

Intraplate Seismicity: Seismicity in the period from 5/1985 to 4/1995 with locations using at least eight stations, is shown in two profiles for region 1 and 2 (Fig. 3.4). Earthquakes can be grouped into those shallower than 40 km in the western coastal and land areas, the deep earthquakes in the mantle wedge apex, and the earthquakes in the upper and lower seismic planes in the subducting plate. The aseismic front is nearly parallel to the volcanic front. There is a prism-like region bounded by the ground surface, the aseismic front (AF) and the upper boundary of the subducting plate in region 1 (Fig. 3.4a). However, such a prism-like distribution is physically smaller or perhaps even missing in region 2 (Fig. 3.4b).

3.4.2 Gravity and Topography

The characteristics of topography and GRA change with latitude.

Region 1: The gravity data are Bouguer (on land) and free-air (at sea) taken from Kono and Furuse (1989). Gravity data and topographic/bathymetric data were projected along a transect **AA'**, 20 km wide from 39.75°N/137°E to 39.5°N/145°E (Fig. 3.1). It has long been noted that the Kitakami range has a pronounced positive Bouguer anomaly, which indicates that it is out of isostatic equilibrium. The average GRA at the Kitakami range is about +75 mGal. The average elevation of the Kitakami range is about 750 m (Fig. 3.5a, b).

Region 2 : There is no mountain range in the outer arc, but the GRA is about +30 mGal in the eastern coastal area (Fig. 3.5c, d). Thus, the outer arc region is still not in a state of isostatic equilibrium. The volcanic front does not have a high GRA. The older (Cretaceous) volcanoes in the inner arc have a positive GRA (+30 mGal). Note the lateral change of gravity along the strike of the island arc in the western coastal area (Fig. 3.5d). The GRA along profile **CC'** differs from that along **BB'**, which may be due to the geological complexity in the adjacent Japan sea. Moreover, there is also a complex and wide distribution of faults in the western coastal area. We therefore focus on the effects of different assumed coupling on the observables in the outer arc, and we do not try to match the detailed structure off the west coast.

Region 3 : The average elevation of the Abukuma range is slightly less than the Kitakami range, and the width of the Abukuma range is much less than the Kitakami range. The GRA is smaller in the Abukuma range (Fig. 3.5e, f).

3.4.3 Heat Flow and the Curie Depth

Heat flow data are similar in the three regions (Furukawa and Uyeda, 1989; Pollack et al., 1993). Heat flow is high (about 100 mWm⁻²) in the inner arc and low (about 40 mWm⁻²) in the outer arc. The Curie depth is about 10 km in the inner arc and increases to 30 km near the east coast (Okubo, et al., 1989, 1991, 1994).

3.5. Implementation of Coupling in Finite Element Modeling

Coupling is implemented as a boundary condition, and represents a long-term force system, acting along the interface between the subducting and overriding plates. Forces acting on the interface can be resolved into horizontal and vertical components. The horizontal push from the Pacific plate is implemented as a displacement increment (Melosh and Williams, 1989; Wallace and Melosh, 1994). The displacement increment is mathematically equivalent to the force on the interface (Sato and Matsu'ura, 1992).

We use two scalar quantities to define the coupling strength between the subducting and overriding plates: the *Coupling magnitude*, C_0 , and the *Coupling ratio*, C_r .

C_0 is a measure of the strength of the coupling and is defined as the coupling at the median depth of the coupled interface (Fig. 3.6). C_0 is a normalized quantity of forces acting on the interface, which is taken as 1 for the forces to match the observed topography and gravity of profile AA' in region 1. Notice that C_0 is not a measure of seismic efficiency, such as the seismic coupling factor used in Sato (1988).

C_r is used to describe the depth dependence of the coupling along the interface. As shown in Figure 3.6, the coupling can be either uniform over the depth range of the coupling zone or change with depth. For simplicity, we assume a linear geometry for the interface, and coupling starts from some minimum depth. From Figure 3.6,

$$C_r = C_2 / C_1$$

and

$$C_2 - C_0 = C_0 - C_1,$$

where C_2 is the coupling magnitude at h_2 , the bottom of the coupled zone, and C_1 the coupling magnitude at h_1 , the top of the coupled zone.

Thus, if $C_r=1$, the coupling equals C_0 over the interface. If $C_r >1$, coupling increases with depth. If $C_r <1$, coupling decreases with depth.

3.6. Modeling

In northeast Japan, region 1 has the highest topography and GRA, while region 2 has the lowest elevation and GRA. We accordingly model these two regions to study the extreme cases of coupling in northeast Japan.

The finite-element modeling procedure, as well as the starting and final models for region 1, are described in detail by Huang et al. (1966). The procedures are essentially the same for region 2. The two regions differ in some aspects of the model, the boundary conditions and the inclusion of faulting. In this section we describe briefly the procedures and models, with an emphasis on the differences for the two regions.

3.6.1 Modeling Preliminaries

We model erosion and deposition with two constraints: erosion/ deposition is directly proportional to the square of height/depth (Ohmori, 1978), and the volume of deposited material is matched to that of the erosion. The erosion rate in the model presented here for both regions is 0.3 mm/year for a height or depth of 1000 m. This is the rate obtained by Ohmori.

The size of the time step varies during a model run. The first period has 100 time steps with a step size of 0.15 year. A small time step for the initial stage helps stabilize the solution. The second period has 2000 steps, each 600 years long, while the last 3100 steps have a step size of 1200 year. The total number of time steps is 5200, resulting in a total model duration of about 5.0 Ma (4,920,015 years).

Table 3.1. Material properties of the model for both the southern region and the northern region

No.	E (Pa s)	Density (kg/m ³)	Viscosity (Pa s)	Poison's ratio
1	6.5x10 ¹⁰	2500	elastic	0.25
2	5.5x10 ¹⁰	2400	elastic	0.25
3	4.5x10 ¹⁰	2400	elastic	0.25
4	5.5x10 ¹⁰	2400	elastic	0.25
5	6.5x10 ¹⁰	2600	elastic	0.25
6	5.5x10 ¹⁰	2500	elastic	0.25
7	4.5x10 ¹⁰	2500	elastic	0.25
8	5.5x10 ¹⁰	2500	elastic	0.25
9	6.5x10 ¹⁰	2700	1.0x10 ²²	0.25
10	5.5x10 ¹⁰	2600	1.0x10 ²²	0.25
11	4.5x10 ¹⁰	2600	1.0x10 ²²	0.25
12	5.5x10 ¹⁰	2600	elastic	0.25
13	6.5x10 ¹⁰	2900	1.0x10 ²²	0.25
14	5.5x10 ¹⁰	2800	1.0x10 ²²	0.25
15	4.5x10 ¹⁰	2800	1.0x10 ²²	0.25
16	5.5x10 ¹⁰	2800	elastic	0.25
17	5.5x10 ¹⁰	3000	2.5x10 ²⁴	0.25

Figures 3.7 and 3.8 show the finite-element models for regions 1 and 2 respectively. (Fig. 7 only shows part of inner arc.) For both, we used a finite element grid which is 1000 km long with 1843 nodes and 1592 elements. The models differ only in the area between the volcanic front (VF) and the western coast. Based on the similarities in thermal properties, material properties are the same for both regions and are given in Table 3.1. For region 1, Huang et al. (1996) find the elastic thickness in the inner arc to be 10 km, increasing to 40-50 km in the outer arc close to the subducting plate. One major difference between the two regions is the existence of older (Quaternary), extinct volcanoes in the western coast area (Geological Survey of Japan, 1992). The elastic thickness of the plate under the extinct volcanoes is assumed to be similar to that under

the presently active volcanoes, and is therefore slightly thinner than the adjacent areas with no volcanoes.

3.6.2 Boundary conditions

3.6.2.1 Region 1

A detailed discussion of the boundary conditions is given in Chapter 2. Surface loads of sea water, sediments at the west coast, and the volcanic rocks given near the volcanoes are applied to the upper surface (Fig. 3.7). The left (west) edge of the model is constrained to move in a vertical direction only, and vertical Winkler restoring forces are applied to the bottom of the mesh to simulate isostasy. For the right (east) edge, we take into account coupling between the subducting Pacific plate and the overriding plate.

Tight coupling exists only from 10 km to about 50 km depths. The vertical forces due to the oblique slab drag are specified; and the horizontal displacement increment is specified to simulate horizontal push from the subducting plate. We considered four cases of coupling along the interface: decreasing coupling ($C_r=1/1.5$), uniform coupling ($C_r=1$), 1.5-fold increasing coupling ($C_r=1.5$), and two-fold increasing coupling ($C_r=2$). The coupling magnitude C_0 is given as: $C_0=1$, $C_0=0.5$, and $C_0=0.25$ respectively for the three cases.

3.6.2.2 Region 2

The southern region has subsided about 1000 m during the Neogene (Fig. 3.5-6, Research Group for Quaternary Tectonic Map, 1973; and Sugimura and Uyeda, 1973). The coastal plain of the Japan sea is underlain by thick Neogene sedimentary and volcanic rocks, especially in the Niigata Basin (Tamaki, 1988). These rocks are treated as a surface load. Erupted volcanic rocks at the volcanic front, having an eruption rate of 25 km³/km/ma, are included as a time-dependent surface load. There is a wide area of Pre-Quaternary volcanic arc between the western coast and the Quaternary volcanic arc. This is also treated as surface loading (Fig. 3.8b).

The tectonic loading is as in region 1. For this region we consider three cases of depth dependence for coupling along the interplate interface: uniform coupling ($C_r=1$), and two cases of increasing coupling ($C_r=1.2$ and $C_r=2$). We also consider three cases of coupling magnitude: $C_0=1$ (a horizontal velocity of 1 mm/year, and an equivalent average vertical force of 3.75×10^{10} N/m), $C_0=0.5$ (a horizontal velocity of 0.5 mm/year and a average vertical force of 1.875×10^{10} N/m), and $C_0=0.25$ (a horizontal velocity of 0.25 mm/year and an average vertical force of 0.937×10^{10} N/m).

3.6.3 Faulting

3.6.3.1 Region 1

As discussed in Chapter, there are two high horizontal stress concentration zones: one on the western coastal area and the other near the volcanic front area at 1.8- Ma. In each zone, either

of the two fault planes is likely to slip. We insert slippery nodes into the model in these regions. The dip of the fault is inferred from the observed active faults which are exposed at the earth's surface (Matsuda et al, 1980). Figure 3.7 shows the geometry of the faults that are introduced in the grid.

3.6.3.2 Region 2

As the stress increases, we examine the grid to locate regions where the failure threshold (according to the Mohr-Coulomb criterion) is reached. To parameterize the failure criterion, we used 1.05 kbar for the cohesion strength, and 0.53 for the coefficient of internal friction (Handin, 1969). By 3.0 Ma we can identify three well-defined high horizontal stress concentration zones: one in the western coastal area, another below the extinct volcanoes between the west coast and the volcanic front, and the other near the volcanic front area for a model in which $C_r=1.2$ and $C_0=0.25$ (Fig. 3.9). As in our modeling for region 1, we insert slippery nodes into the model in these zones at that time (Fig. 3.10). The dip of the fault is inferred from the observed active faults which are exposed at the earth's surface. On the western coastal plain there are many thrust faults dipping to the east (Research Group for Active Faults of Japan, 1991), so an easterly dipping fault was introduced. We postulate a 30% partial stress drop as we did in region 1.

In Figure 3.9b there is a highly compressive PTF region at about 575 km from the left-hand side and 20 km deep, and a near surface, highly tensional PTF region at about 600 km. These are artifacts of the model resulting from our simplified viscosity structure: the assumed abrupt change of viscosity from the inner arc to the outer arc as well as a sudden change of slope at 585 km and 22 km deep. Because the processes are thermally activated, the true model should have a more gradual transition in viscosity which would lower the stress concentration. We have shown how a more gradual viscosity transition lowers the magnitude of the PTF in those zones (Huang et al., 1996), and do not consider them further in this thesis.

3.7 Results

3.7.1 Region 1

For a constant coupling ratio of 2 ($C_r=2$), we examine the effect of coupling magnitude. As the coupling magnitude increases, topography and GRA increase (Fig. 3.11). $C_0=1$ and $C_r=2$ best fit the topography and gravity residual anomaly in northeast Japan.

For a constant coupling magnitude ($C_0=1$), we compare the topography and gravity signatures accumulated over the past 5 million years with different states of coupling: increasing coupling, uniform coupling and decreasing coupling. For a 2-fold increasing coupling with depth ($C_r=2$), the topography and the GRA highs at the Kitakami range match the observed data very well (Fig. 3.12a). A 1.5-fold increasing coupling produce slightly lower topography and GRA at the Kitakami range (Fig. 3.12b). Uniform coupling does not reproduce the characteristic topography and GRA in the outer arc region (Fig. 3.12c). For a 1.5-fold decreasing coupling ($C_r=1/1.5$), topography and GRA are a poor match the observed data (Fig. 3.12d).

3.7.2 Region 2

For $C_r=1.2$, we examine the effect of different C_0 on topography and gravity. Figure 3.13 shows results for C_0 values of 1, 0.5, and 0.25. The left panels of figure 3.13 show the result of topography, and the right panels show the calculated GRA. Topography and GRA for the land area decrease as coupling magnitude decreases.

$C_0=1$ is unacceptable because the predicted topography and GRA are both too high. Both $C_0=0.5$ and $C_0=0.25$ produce acceptable fits for topography and GRA. $C_0=0.25$ produces a slightly better match for topography and GRA near the outer arc region.

Next we hold C_0 at 0.25 and assess the effect of different assumed C_r . Figure 3.14 shows the topography and displacement of the plate under uniform coupling ($C_r=1$), 1.2-fold increasing coupling ($C_r=1.2$), and 2-fold increasing coupling ($C_r=2$). Not much difference is seen in the western coast area. A 2-fold increasing coupling produces a slightly higher topography and gravity residual in the outer arc region. Both $C_r=1.2$ and $C_r=1$ result in quite acceptable matches for the topography and gravity in the outer arc region.

From the above comparison, $C_r=1.2$ and $C_0=0.25$ best fit the observed data. Since our model (including rheology and boundary conditions) is too simple to reproduce the complexity of the geology in the western coast and the Japan sea, our results predict the trend of the change in topography and gravity in the west, but do not match smaller scale details very well. Dealing with the complications of the crustal deformation in the Japan sea is beyond the scope of this study.

In summary, topography and gravity at the outer arc are very sensitive to the strength and distribution of coupling along the interplate interface. When C_0 is large, the effect of C_r is more obvious. Having an increasing coupling with depth appears to be a critical factor for the formation of the Kitakami range in the outer arc region.

3.8. Discussion

We discuss first how the coupling inferred from our modeling correlates with interplate seismicity. The seismicity of the overriding plate is related to both the rheology and the interplate coupling. After a discussion of the aseismic front, we discuss the interplate coupling for the two regions.

3.8.1 Interplate Seismicity and Coupling

We have shown the effect of coupling on the formation of geological structure, e.g., the Kitakami and Backbone ranges. Coupling along the interplate interface affects the topography and gravity signature. Region 1 has a stronger coupling in terms of both a higher coupling magnitude and a higher coupling ratio: Best fits to the data are found for $C_0 = 1$ and $C_r = 2$ in region 1, while $C_0=0.25$ and $C_r=1.2$ in region 2. As we mentioned above, large interplate earthquakes would appear to require strong coupling between the subducting and overriding plates. Only region 1 has large, shallow, interplate thrust earthquakes.

We did not model region 3 (the Abukuma range and off Fukushima). From Figure 3.1, the Abukuma range is much narrower and lower than the Kitakami range and has a different

geological history (Geological Survey of Japan, 1968; Miyashiro, 1961). In addition, the GRA, an indicator of stress, is much smaller in the Abukuma range, and is not much greater than that in region 2. We infer from these observations that the coupling stresses in region 3 are below those of regions 1 and 2. Figure 3.5 shows a comparison of topography and GRA for the three regions.

3.8.2 Aseismic Front and seismicity in the outer arc

The aseismic front has been defined as the seaward edge of the aseismic mantle wedge beneath the island arc (Yoshii, 1979). Kawakatsu and Seno (1983) defined a seismic slip front as the landward limit of the thrust zone which defines the edge of the seismic coupling zone at the thrust zone along the interface between the subducting and overriding plates. They found that the seismic slip front is coincident with the aseismic front. Accurate depth determinations for shallow events outside a seismic network are difficult, and in Figure 4 we used only well recorded events, observed on more than 8 stations. However, Umino et al. (1995) have located events in this region using a recently identified *sP* phase which gives better depth constraint, and found all events on the interplate boundary. More recently, Umino (personal communication, March 1996) has found *sP*-constrained events in the wedge region. Therefore, we accept that the seismicity patterns shown in figure 3.4 are reliable.

3.8.3 Intraplate Seismicity

Intraplate seismicity in the overriding plate also correlates with the coupling along the interface between the subducting and overriding plates. As discussed above, when the PTF is greater than 1, there is slip on a fault and earthquakes occurs. We now discuss the PTF values and the observed intraplate seismicity near the apex of the mantle wedge in northeast Japan (Fig. 3.15).

Region 1 is a strongly coupled region ($C_r=2$, $C_0=1$). A prism-like region of high PTF ($PTF>1$) develops in the mantle wedge of the outer arc region (Fig.3.15a). This high PTF region is highly correlated with the observed distribution of small and large intraplate earthquakes in the region between the earth's surface and the interplate interface (Fig. 3.15a).

Fig. 3.15b shows the overlay of seismicity and the potential fracture zone ($PTF >1$) in region 2. The region has weak coupling ($C_r=1.2$, $C_0=0.25$), and the PTF is always below 1 in the mantle wedge and most of the crust. There is only one shallow area near the surface (in the distance range 650-800 km) which has a high PTF.

The seismic zone in the overriding plate may be used to infer the strength of coupling at the interplate interface. In region 1, the development of a prism of seismicity in the wedge is related to the potential for large or great interplate earthquakes on the subduction interface; while a lack of intraplate seismicity in the wedge is related to there being only smaller earthquakes along the subduction zone (Fig. 3.16).

The mechanics causing the variations of coupling is beyond the scope of this study.

3.9. Conclusions

Two key parameters defining the state of interplate coupling are coupling magnitude (C_0) and coupling ratio (C_r). Satisfying the constraints from topography and gravity, C_0 in region 1 is about 2-4 times greater than that in region 2, and C_r is about 1.5-2 times greater than C_r in region 2. C_0 and C_r for region 3 is inferred to be between the above two cases.

The coupling affects topography and gravity for the overriding lithosphere, as well as its strength, seems to be correlated with the occurrence of large interplate earthquakes and the number of microearthquakes. A prism-like seismogenic zone is predicted by our models in the crust and mantle wedge apex of the northern area, but no such seismogenic zone is predicted for the outer arc area in region 2. Tight coupling yields high topography and gravity residual anomaly in the east-coast area, while loose coupling yields lower topography and gravity residual anomaly in the outer arc (Fig. 3.16).

In region 3, the Abukuma range is much narrower and lower than the Kitakami range. The gravity residual anomaly, is much smaller in the Abukuma range, and not much above that in region 2. Thus, the coupling stresses in region 3 are between those of regions 1 and 2.

The lack of great earthquakes in the southern region could be explained by long recurrence times. Based on our analysis, we have an alternative explanation: that the weaker coupling in the southern region indicates a lack of seismogenic potential which leads to a low probability for large earthquakes in that region.

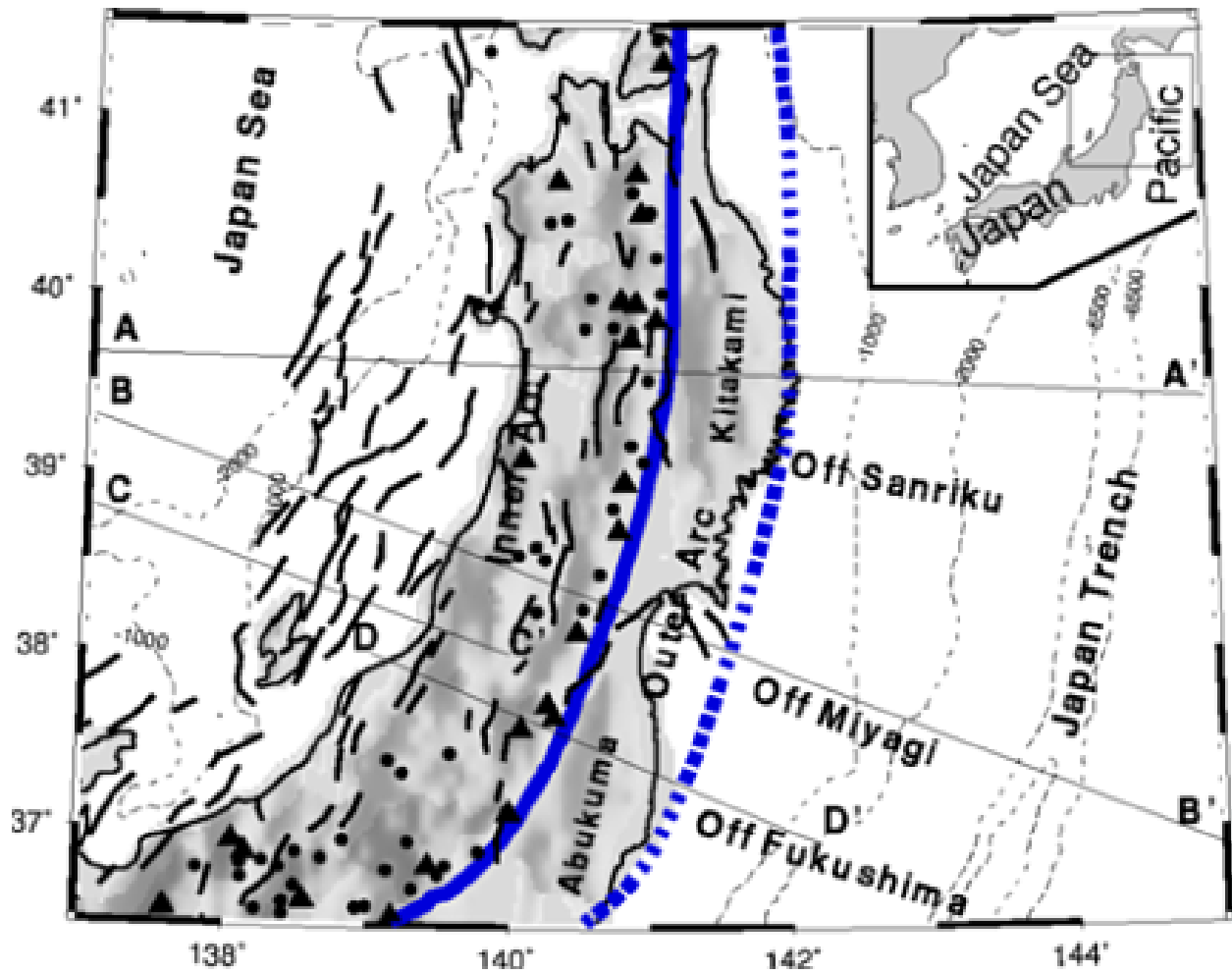


Figure 3.1: Study area in northeast Honshu, Japan. The thick solid line represents the volcanic front. The thick dashed line shows the aseismic front. Solid triangles indicate active volcanoes. The solid circles show the other Quaternary volcanoes. Short solid lines are for the Quaternary faults. **AA'** and **BB'** are for cross sections from the Japan sea to the Pacific ocean. Profile **AA'** is in region 1 (off Sanriku); and **BB'** is in region 2 (off Fukushima). Profile **CC'** is about parallel to **BB'**. Profile **DD'** is in region 3 (off Fukushima). Locations of faults and volcanoes come from the Research Group for Active Faults of Japan (1991). Bathymetry contour intervals are 1000 m, and elevation contour intervals are 250 m. The inset shows the location of Japan, and the outline of the study region.

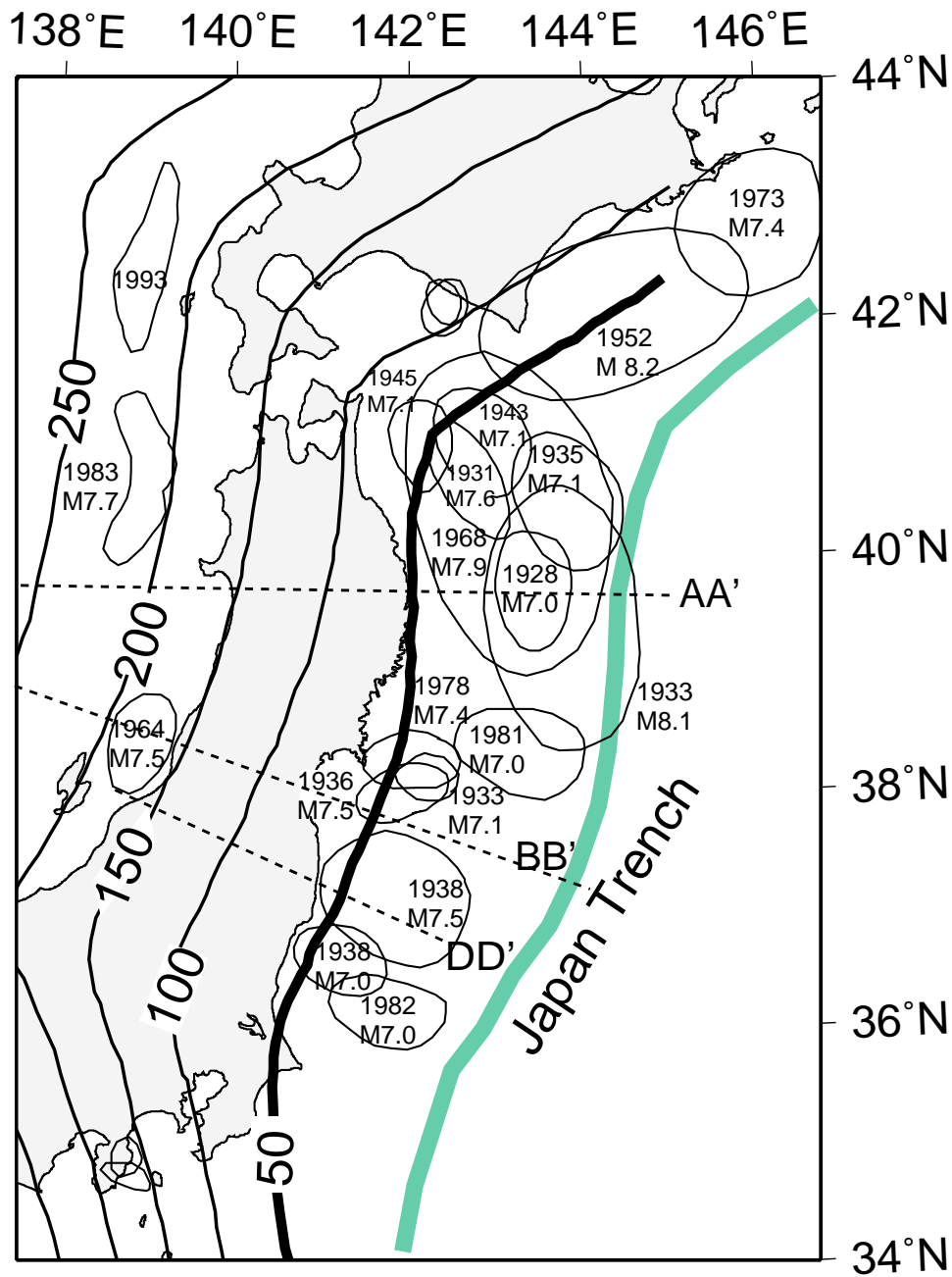


Figure 3.2: Aftershock area for the shallow (<60km) interplate earthquakes with magnitude 7 or greater for the period from 1962 to 1983, as well as the 1993 western Hokkaido earthquake. The contour lines show the depth to the upper seismic plane of the subducting Pacific plate (after Hasegawa et al., 1985 and Tanioka et al., 1993). Three dashed lines denote profile AA', BB' and DD' in region 1, 2, 3, respectively. Note that the aftershock area at latitudes 40°N and 38°N terminate at about 50km depth.

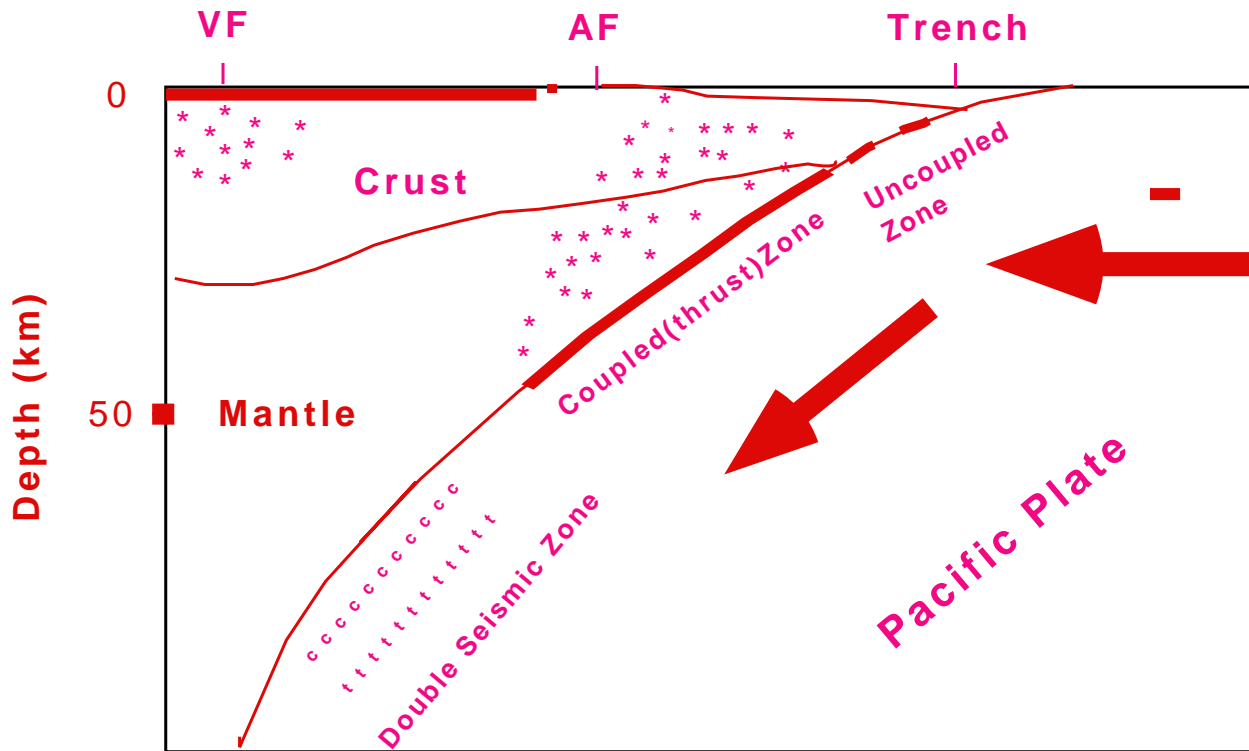


Figure 3.3: A schematic cross section to illustrate coupling between the downgoing oceanic plate and the overriding continental plate. The coupling extends down to about a 50 km depth beneath northeast Japan (Hasegawa et al., 1983, 1985, 1994). **VF** and **AF** indicate the volcanic front and the aseismic front, respectively. The stars represent intraplate seismicity in the overriding plate. **c** in the subducting plate indicates the upper seismic plane (compressional), and **t** represents the lower seismic zone (tensional). The large, thick arrow denotes the subduction of the oceanic plate.

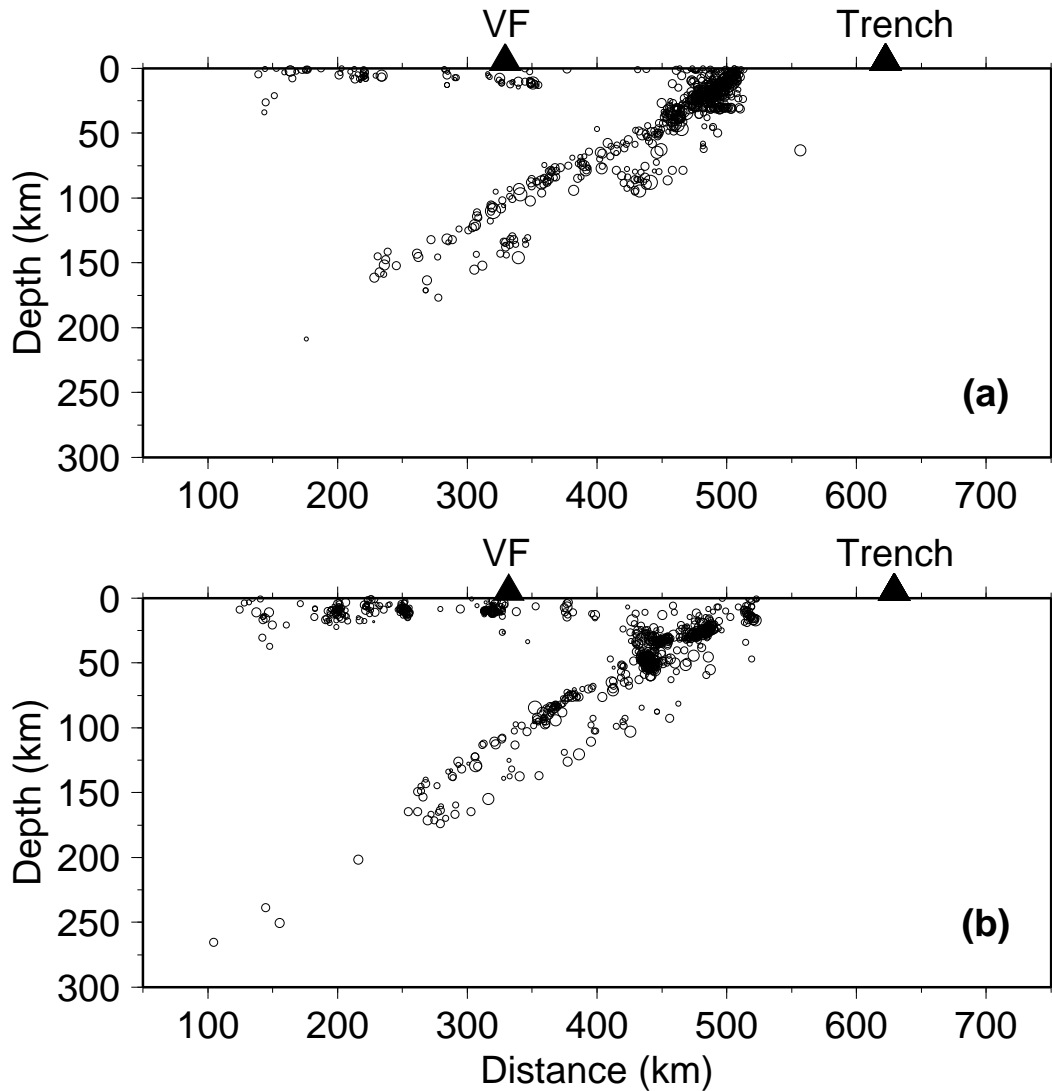


Figure 3.4: (a) Cross section of shallow earthquakes (<60 km) in the overriding plate's crust and mantle wedge, and earthquakes in the subducting plate along **AA'** in region 1. (b) Cross section of the earthquakes along **BB'** in region 2. The projection width is ± 5 km along the profile. Figure 3.1 shows the location of the profiles. **VF** denotes the volcanic front.

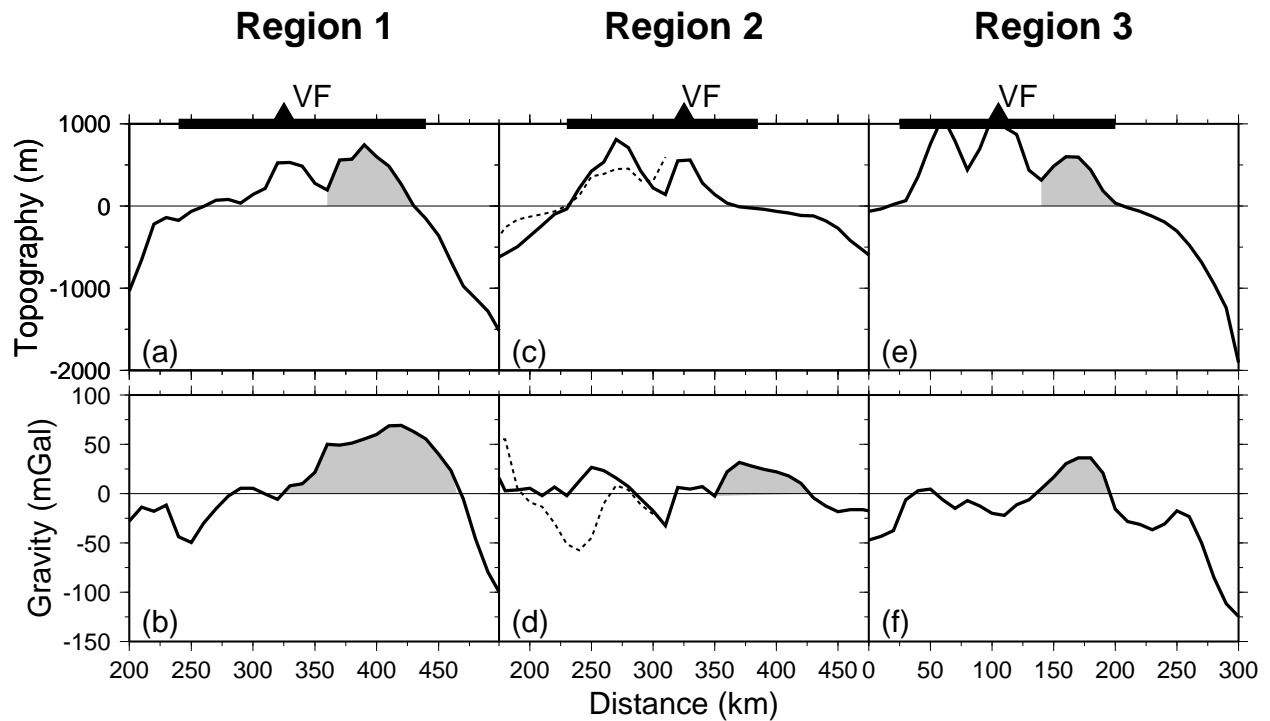


Figure 3.5: Topography and GRA in northeast Japan. (a, b) profile of topography/bathymetry and GRA in region 1. (c, d) profile of topography/bathymetry and GRA in region 2. The dashed line shows the GRA along profile **CC'** (50 km south of **BB'**). (e, f) profile of topography/bathymetry and GRA in region 3. The width for the projection are ± 10 km for the topography and gravity.

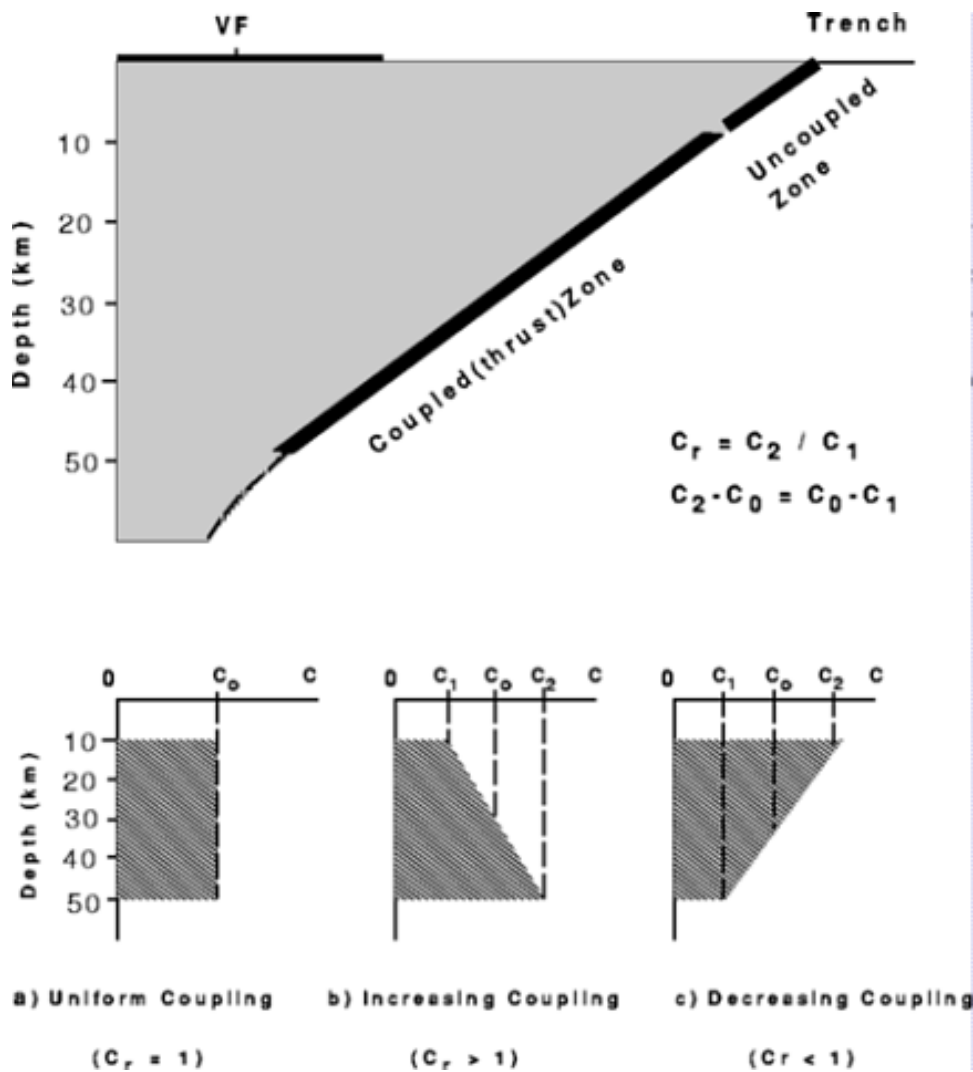


Figure 3.6: Depth dependence of coupling between the subducting and overriding plates (see text for details).

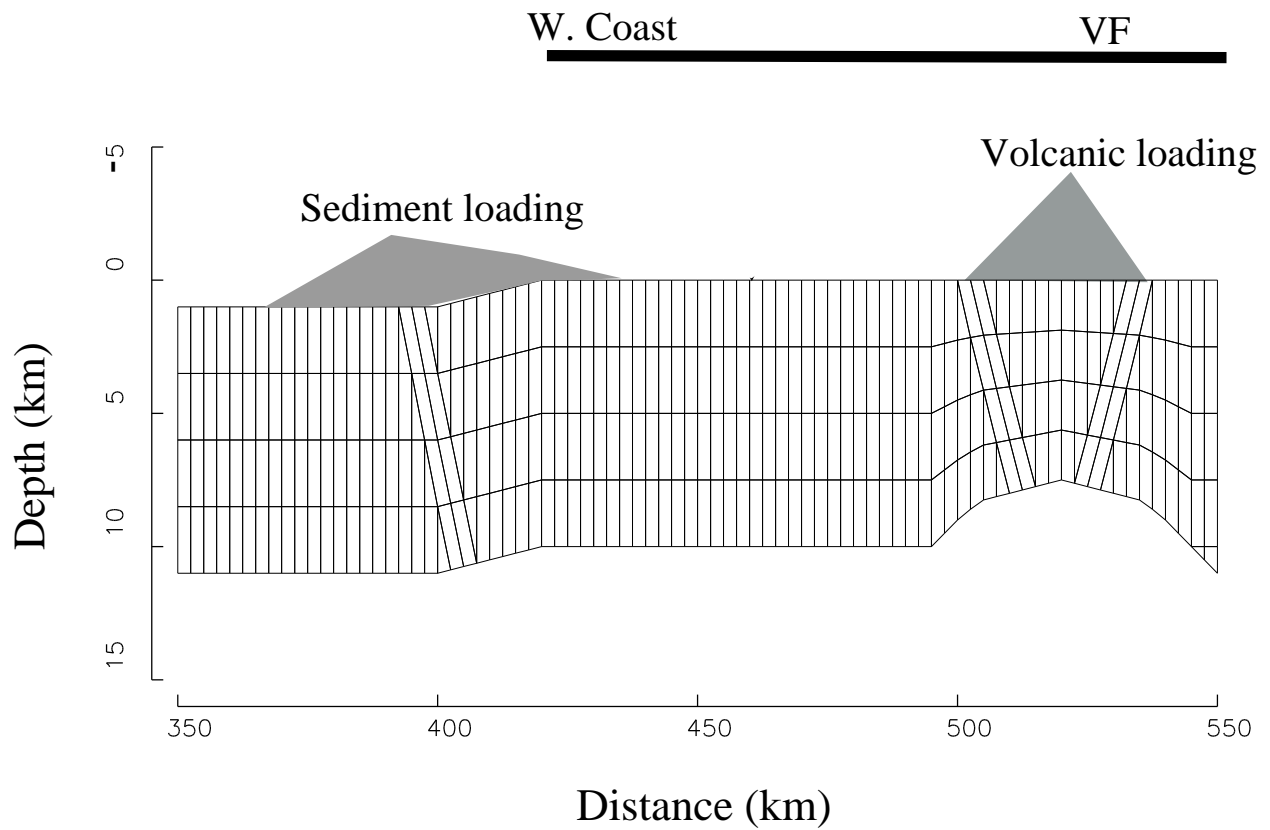


Figure 3.7: Zooming in on the model in region 1. There is volcanic loading at the volcanic front and sediment loading in the western coastal area. The model is similar to that for region 2 (Fig. 8) except there are no extinct volcanoes in the inner arc. Faults are inserted where the PTF determination indicates failure is likely.

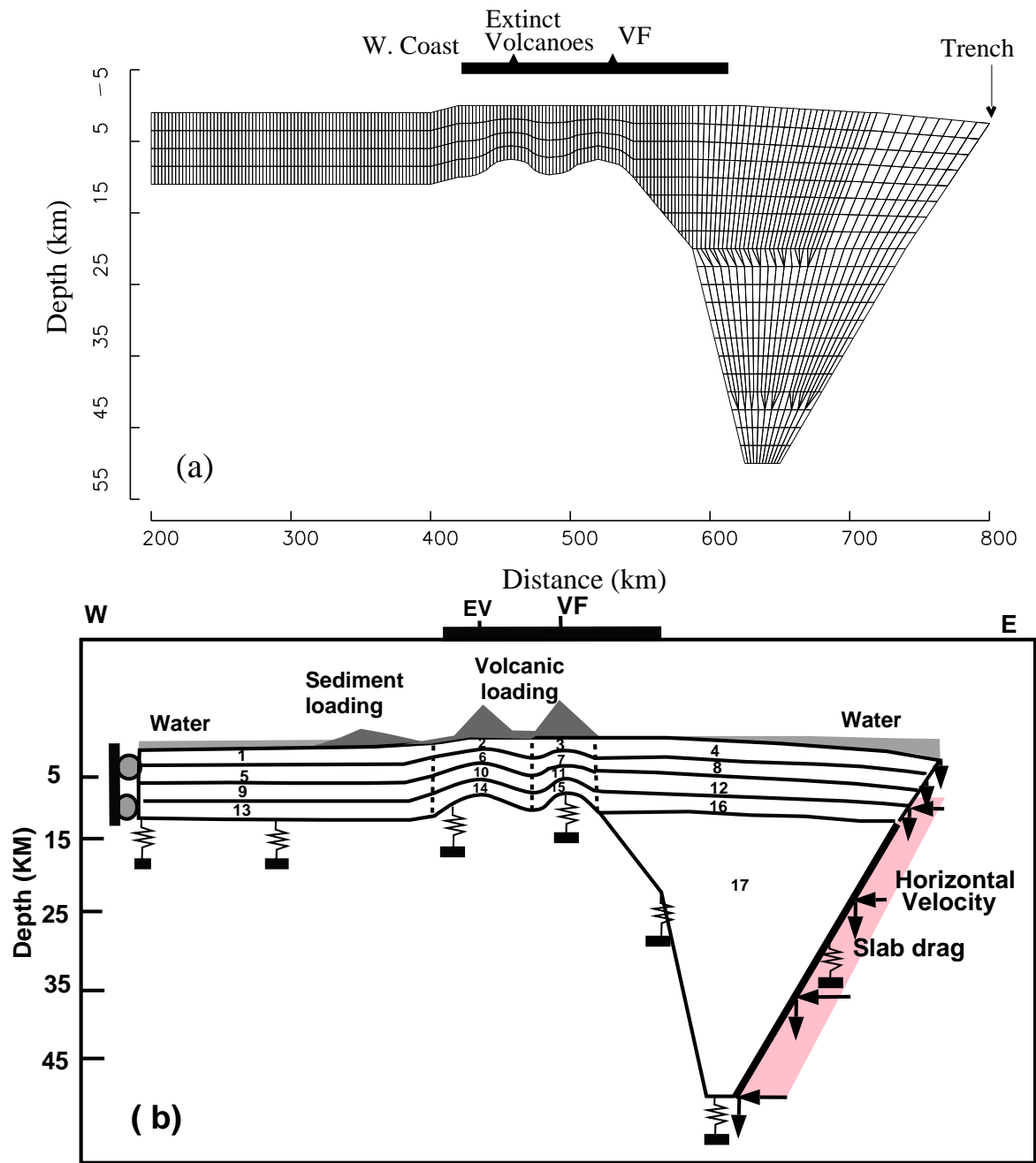


Figure 3.8: Finite element model for region 2. (a) The model grid. (b) The boundary conditions and the material properties of the model (see text for details).

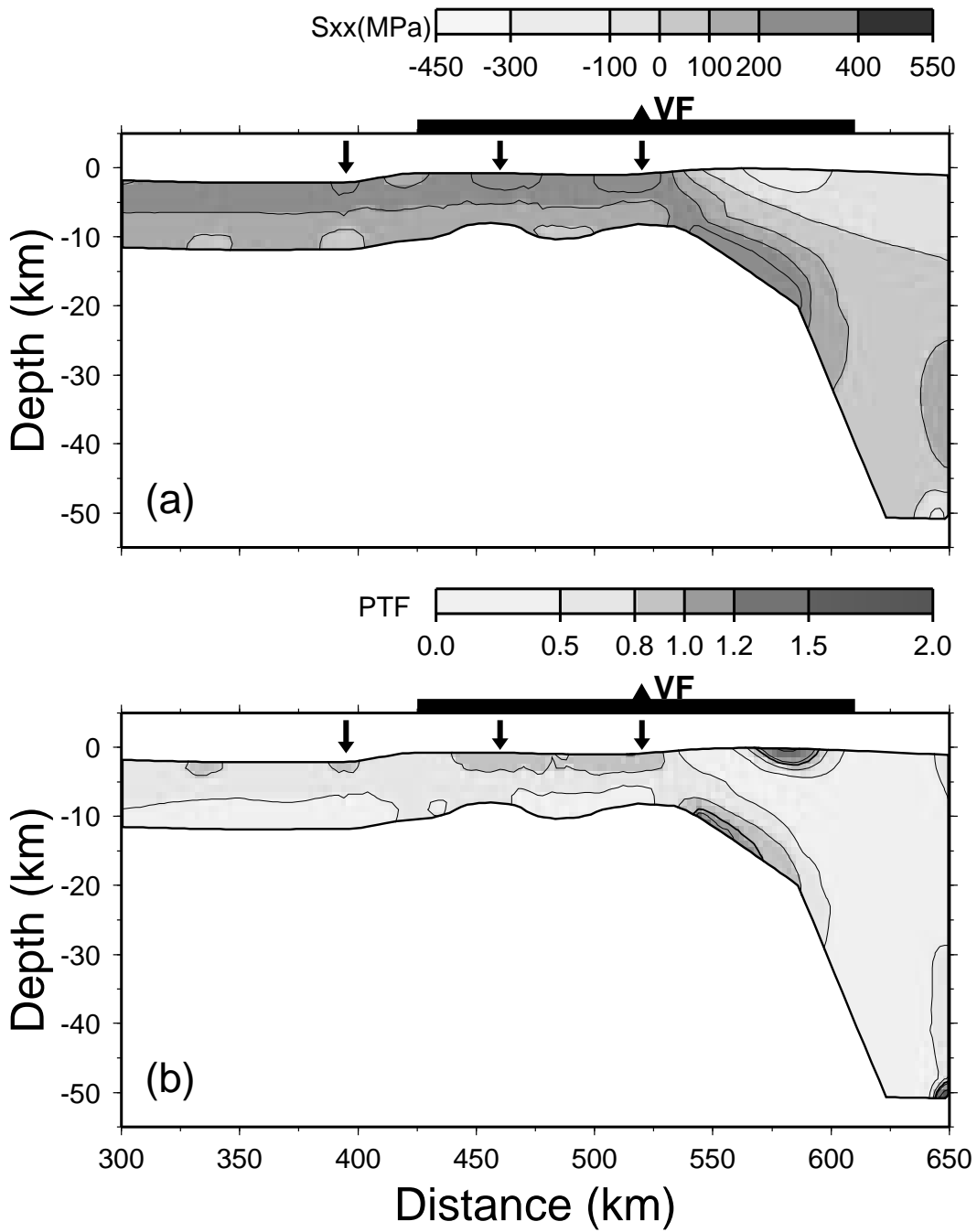


Figure 3.9: Horizontal stress (a) and PTF (b) just before faults initiate. $C_r=1.2$, $C_0=0.25$ for the model. The horizontal stress and PTF are both highest at the western coast, below the extinct volcanoes between the west coast and the volcanic front, and near the volcanic front (indicated by arrows).

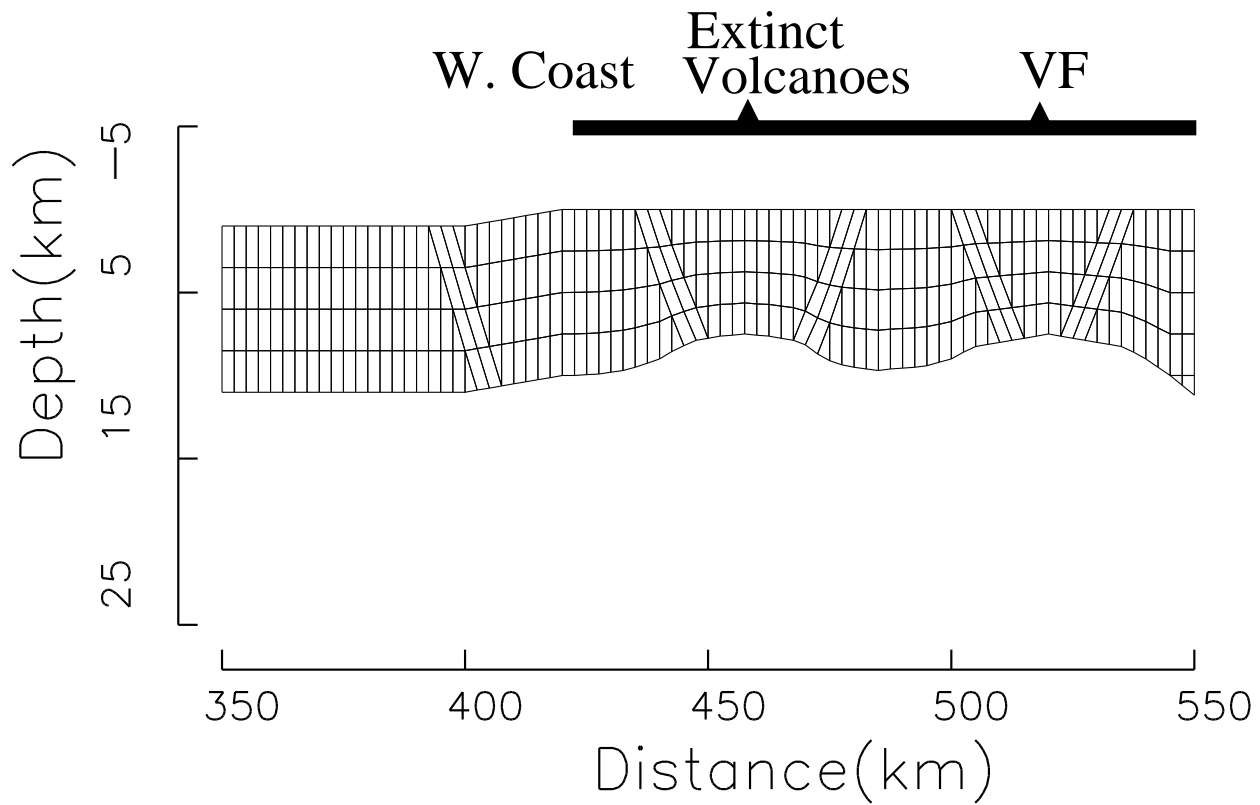


Figure 3.10: Zooming in on the model to show the derived faults and their orientations in region 2.

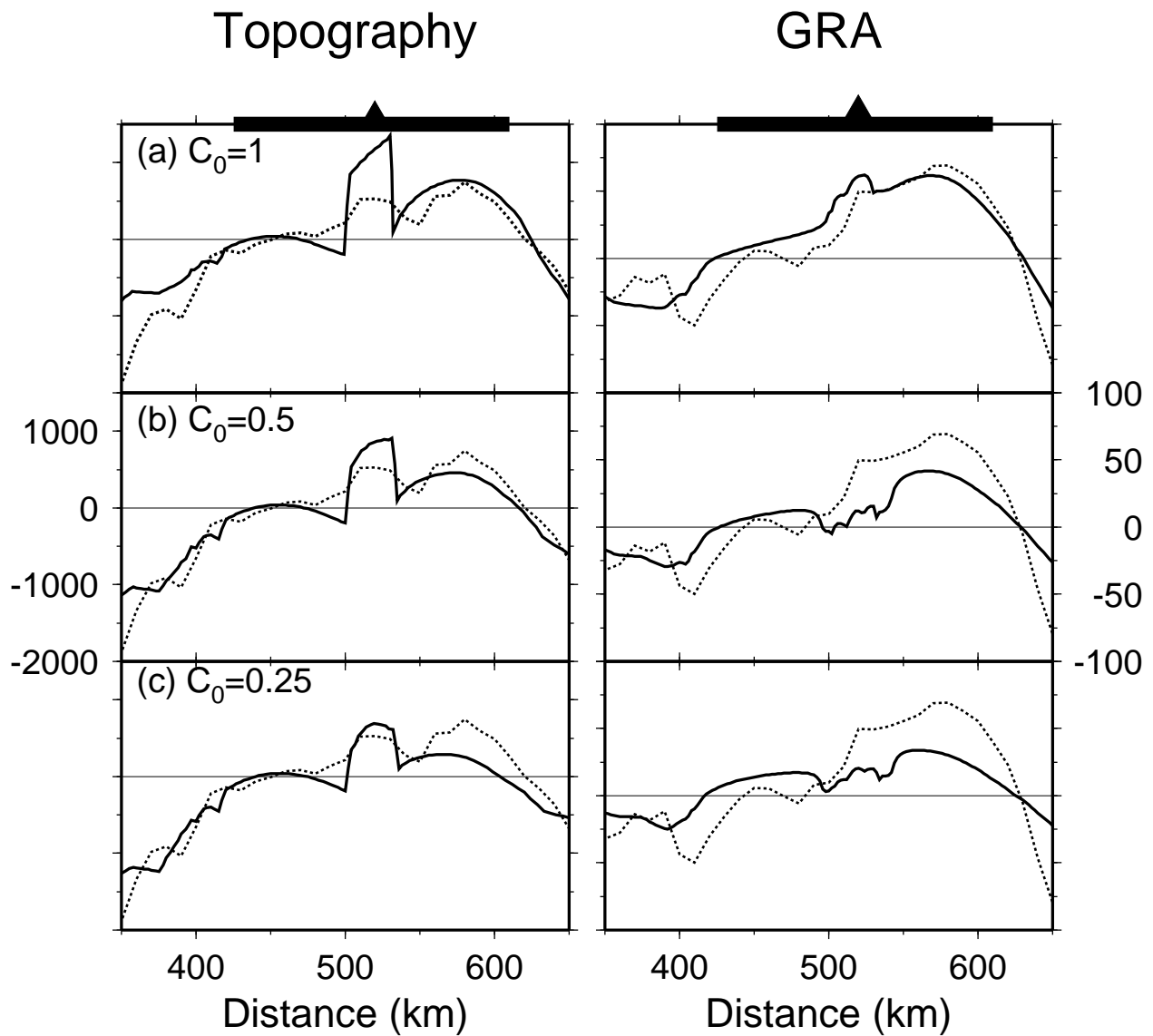


Figure 3.11: Effect of coupling strength in region 1: (a) $C_0=1$; (b) $C_0=0.5$; (c) $C_0=0.25$. Solid lines represent the computed values. Short-dashed lines show the observed values along profile AA' (Fig.1). $C_r = 2$ for all cases. Strong coupling, $C_0=1$, best fits the observed topography and GRA.

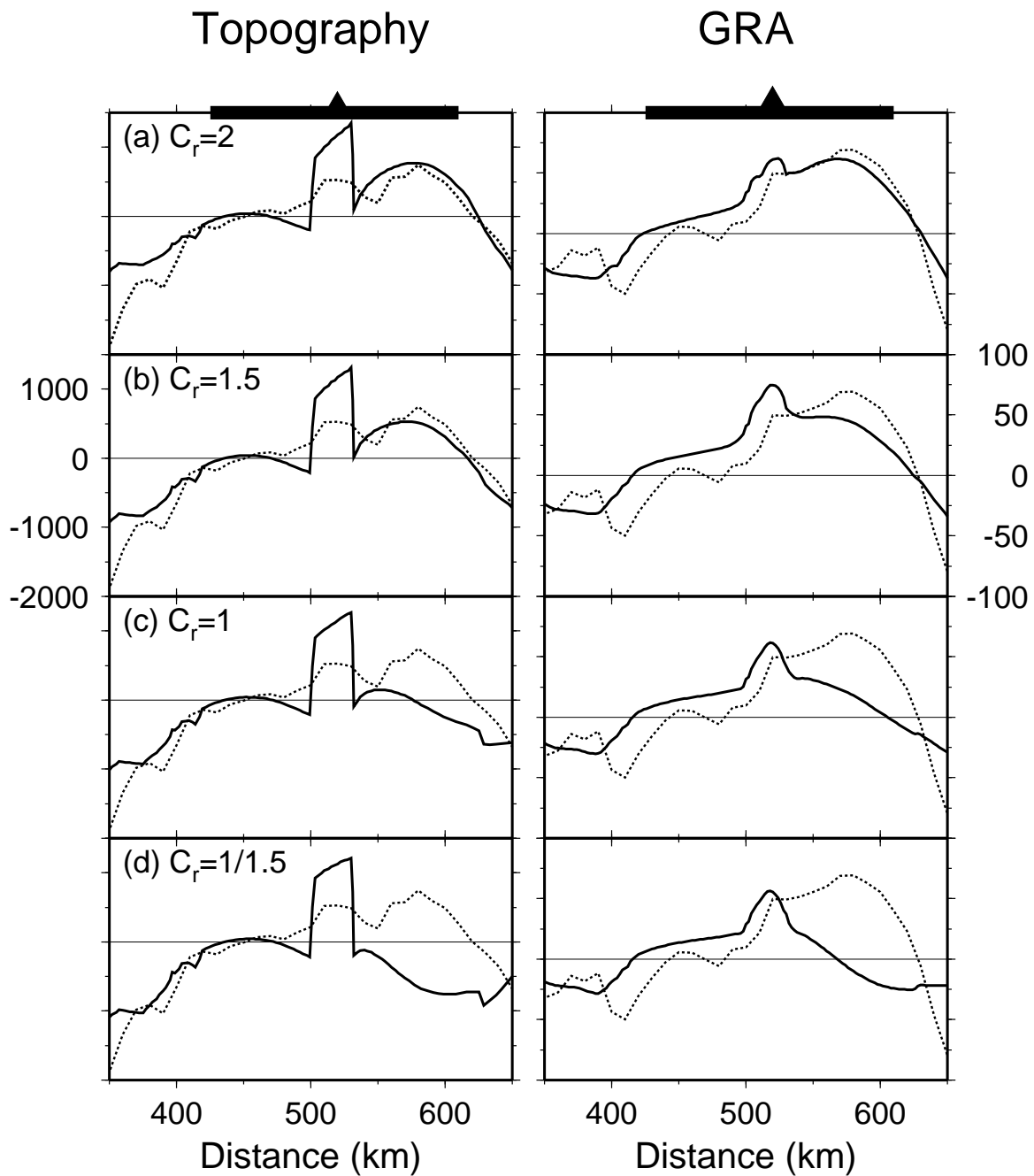


Figure 3.12: For $C_0=1$, the effect of coupling ratio on topography and GRA in region 1; (a) $C_r=2$; (b) $C_r=1.5$; (c) $C_r=1$; (d) $C_r=1/1.5$. Solid lines represent the computed values. Short-dashed lines show the observed values along profile **AA'**. Note that $C_r=2$ best fits the topography and gravity in the eastern coastal range, i.e., the Kitakami range.

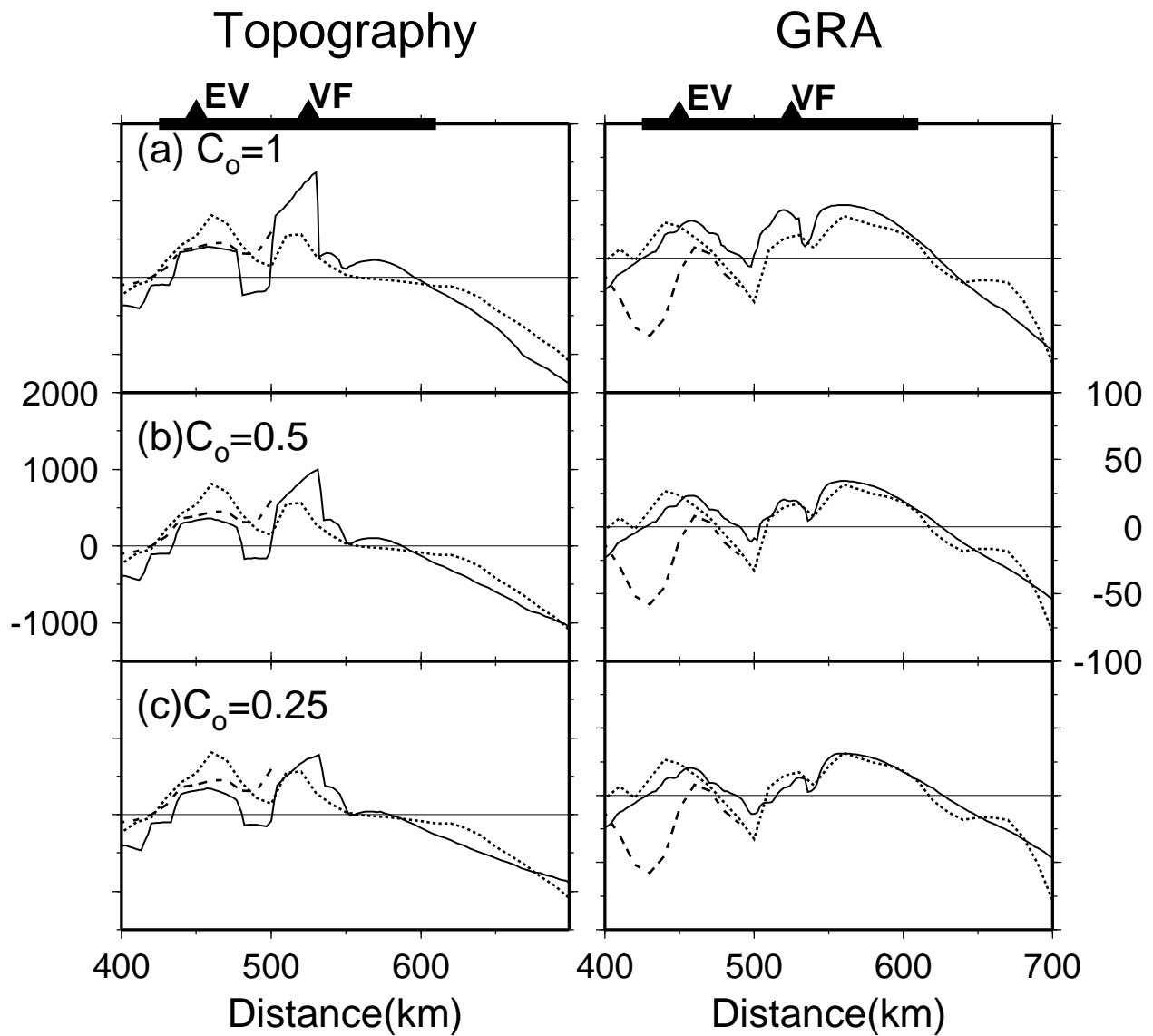


Figure 3.13: Effect of C_0 on topography (left) and gravity (right) in region 2: C_r is 1.2 for all three cases. (a) $C_0=1$; (b) $C_0=0.5$; (c) $C_0=0.25$. Solid lines represent the computed values. Short dashed lines show the observed values along the profile BB' (Figure 3.1). The long dashes represent the data along profile CC' . Note that for strong coupling ($C_0=1$), both the predicted topography relief and gravity residual are too large.

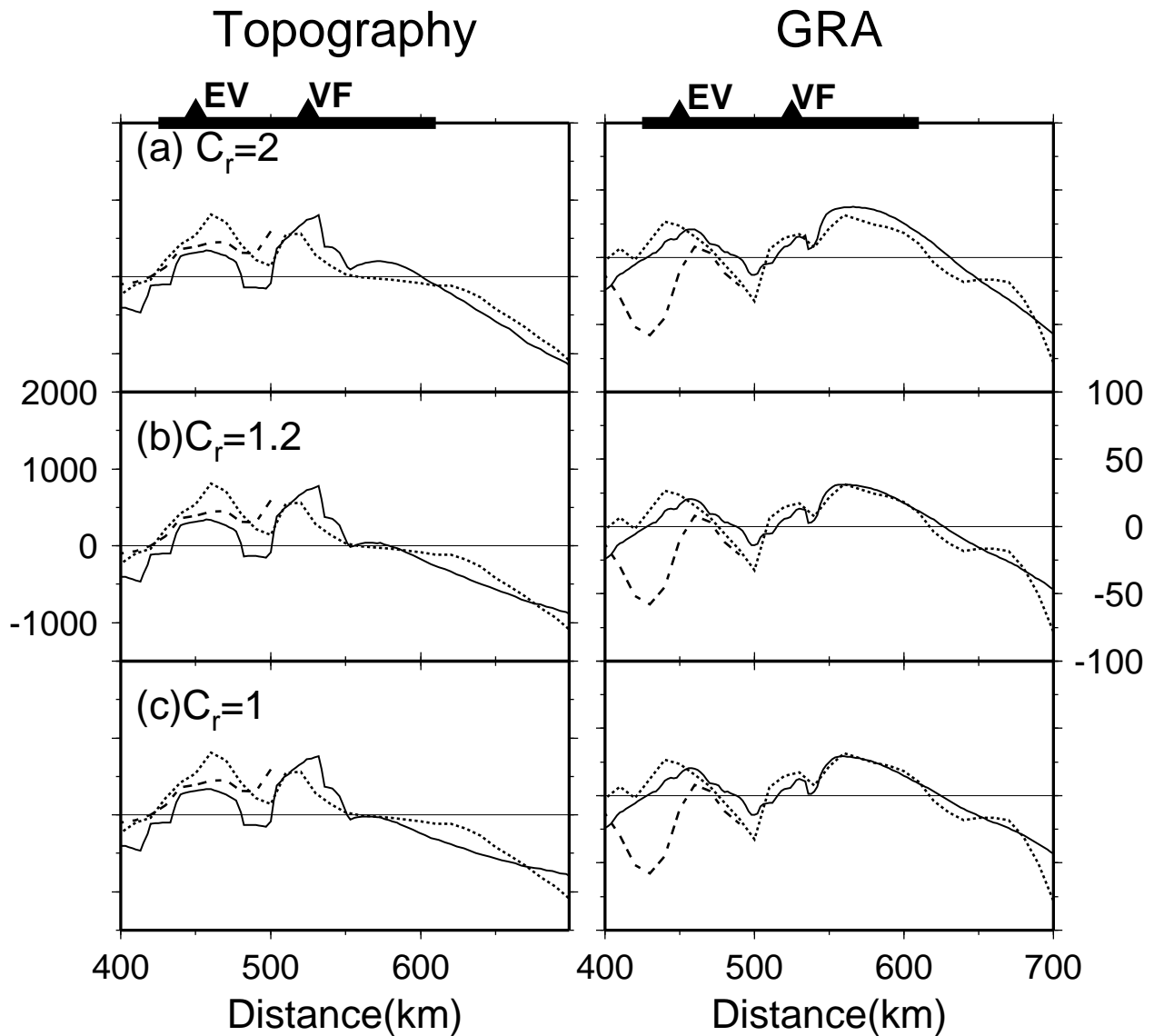


Figure 3.14: Effect of C_r on topography (left) and gravity (right) in region 2: In all cases, $C_0=0.25$. (a) a 2-fold increasing coupling ($C_r=2$). (b) a 1.2-fold coupling ($C_r=1.2$). (c) uniform coupling ($C_r=1$). Solid lines represent the computed values. Short-dashed lines show the observed values along the profile **BB'**. The long-dashed lines represent the data along profile **CC'** (Fig. 3.1), which is about 50 km south of the profile **BB'**.

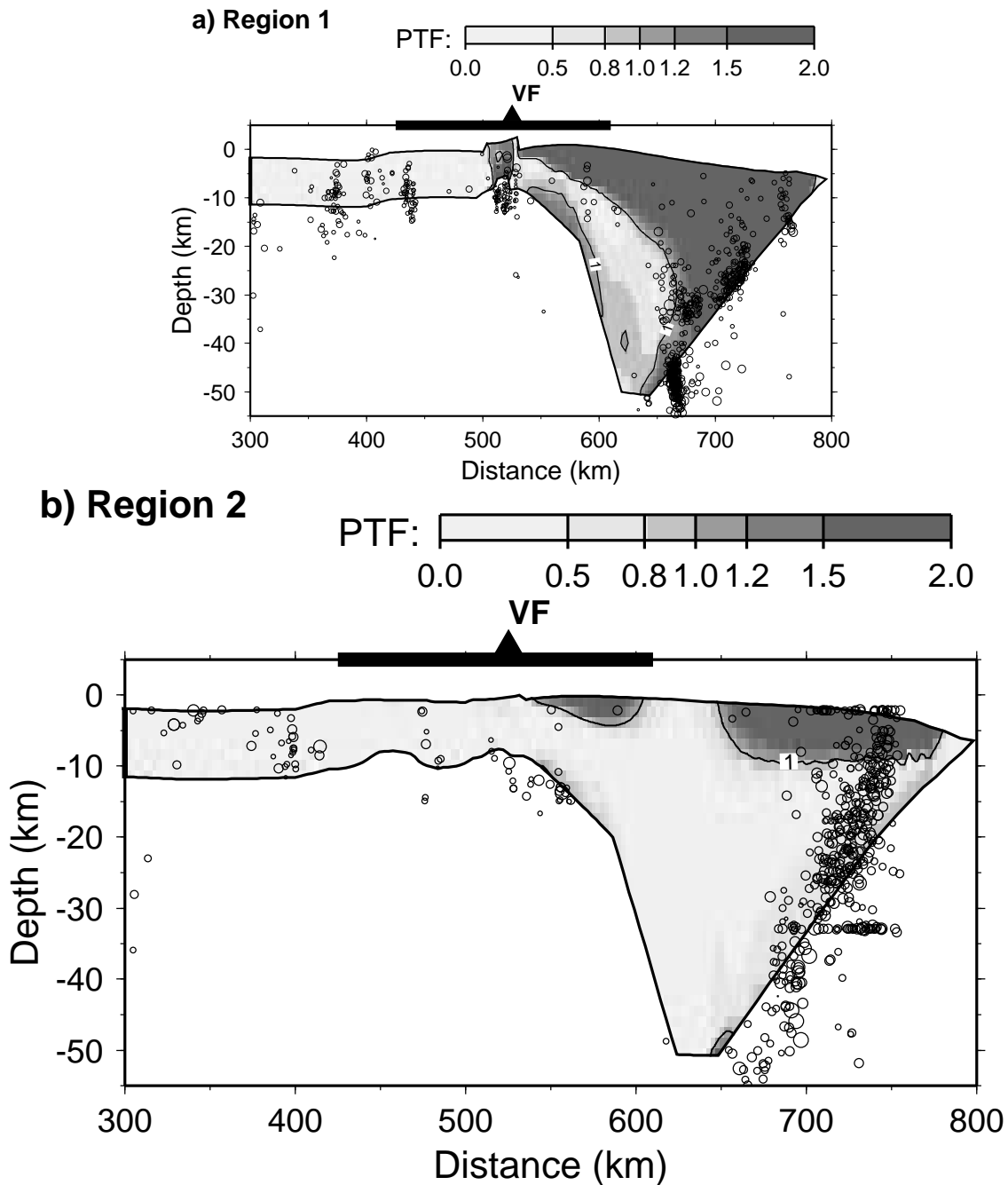


Figure 3.15: Overlaying of PTF and intraplate seismicity at 5 Ma for (a) the model in region 1, (b) the model in region 2. We use the same interplate boundary geometry for both models, but the dip of the interplate boundary in region 2 is less steep, as can be seen from the mis-alignment with the interplate seismicity. The contour lines indicate failure threshold (PTF=1). **VF** denotes the volcanic front. Circles represent intraplate earthquakes.

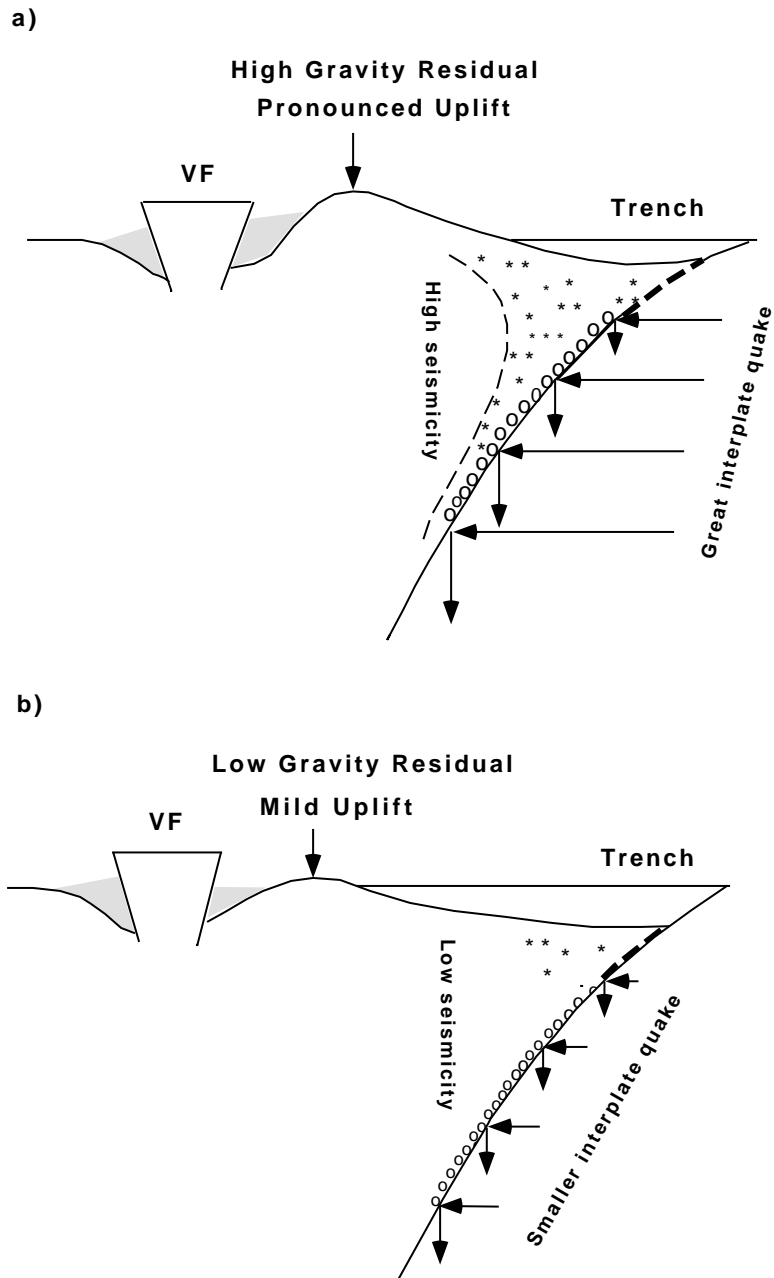


Figure 3.16: Schematic profiles in northeast Japan showing the state of coupling between the subducting and overriding plates, and its relationship to topography, gravity residual anomaly and seismicity of the crust and mantle wedge apex. Stars indicates intraplate seismicity in the overriding crust and mantle wedge. Circles are for interplate (thrust-type) earthquakes. (a) strong coupling in region 1. (b) weak coupling in region 2. **VF** denotes the volcanic front.

Chapter 4: Large Scale Deformation of Island Arc Lithosphere beneath Southwest Japan in the Latest Cenozoic: Finite Element Modeling

4.1. Introduction

In southwest Japan, there is an undulative structural trend sub-parallel to the strike of the Nankai Trough, with a wavelength of about 150-200 km. Compressional deformation dominated in the latest Cenozoic, mostly in the last 2 Ma. The pressure axis of the deeper inland earthquakes is in near N-S direction, which is perpendicular to the structural trend (Hashimoto, 1991). The compressional deformation reflects the long-term subduction of the Philippine sea plate at the Nankai Trough. Note that the compressional axis of shallow seismicity is approximately east-west, which may be caused by the subducting Pacific plate. Effects of the compressional forces from Pacific plate are outside the scope of this study.

The study area in southwest Japan includes the Japan sea, Chugoku, the Setouchi inland sea, Shikoku and the outer arc slope region (Fig. 4.1). There are five subparallel undulative zones from north to south (Hashimoto, 1991): a) a subsidence zone of the northern coastal area, where volcanic activity has occurred since the Miocene; b) an uplift zone at Chugoku, which includes the Quaternary volcanic front (mountain elevation about 500 m); c) a subsidence area in the inland Setouchi sea (water depth very shallow -- less than 50 m); d) an uplift zone in Shikoku, bordered by the Median Tectonic Line along its northern margin as the outer arc of southwest Japan and uplifted more than 1000 m during the late Cenozoic; e) a subsidence zone, the outer arc slope, extending south to the Nankai trough.

Southwest Japan lacks some typical features of island arcs such as those found in northeast Japan. Although there are abundant Miocene volcanic rocks spread over southwest Japan from the Chugoku region to the Kii Peninsula, there are no active volcanoes in this region (Sugimura and Uyeda, 1973; Hirahara, 1981); the late Quaternary volcanic activity exists only in the north Chugoku region.

The tectonic history of the southwest Japan in the Late Cenozoic can be divided into two stages (Hashimoto, 1991; Sugimura and Uyeda, 1973): 1) Miocene, which is a relatively quiet time with little crustal movement or subduction of the Philippine plate at the Nankai trough. 2) about 4 Ma to present, mostly Quaternary, characterized by subduction of the Philippine Sea plate at the Nankai trough. This subduction formed compressional, undulative deformation with a strike parallel to the Nankai trough. The present-day relief of these zones has been mostly formed in the Quaternary (Hashimoto, 1991). The Median Tectonic Line (MTL), with a lateral displacement rate of 0.5-1.0 cm/year, was caused by the oblique, E-W, component of the subduction of the Philippine plate (Fitch, 1972).

Several studies have been conducted to investigate the relationship between the uplift of the outer arc area and the subduction of the Philippine plate (e.g., Thatcher, 1984; Savage and Thatcher, 1992; Sato and Matsu'ura, 1988, 1992; Yoshioka and Hashimoto, 1989). The uplift of the coast of southwest Japan following the 1944 Tonankai ($M_s=8.0$) and 1946 Nankaido ($M_s=8.2$) earthquakes was reasonably well predicted by a simple dislocation model of subduction

(Thatcher, 1984; Savage and Thatcher, 1992). Yoshioka and Hashimoto (1989) utilized a finite-element modeling method to study the correlation between intraplate seismic activity and interplate great earthquakes along the Nankai trough. Sato and Matsu'ura (1988, 1992) used a single-plate subduction model to explain the crustal deformation in southwest Japan for three different time scales: the cyclic occurrence of interplate earthquakes (about 115 years), the steady relative uplift of the marine terraces related to eustatic sea-level fall over the last 10^5 years, and the gradual evolution of the island arc system in the last 4 million years. The lithosphere-asthenosphere system is represented by a stratified viscoelastic half space under gravity, steady-slip motion over the whole plate boundary, and perturbations associated with the periodic occurrence of great earthquakes. Erosion, deposition, and the accretion of oceanic sediment at plate boundaries were also considered in their models.

In this paper we further examine the conjecture that the E-W striking undulative deformation in southwest Japan is a direct result of the steady subduction of the Philippine plate. Our model takes into account coupling along the interplate interface, erosion and deposition, as well as the effect of the Quaternary volcanoes in the northern coast. Utilizing finite-element modeling, we find a plausible rheological structure can explain the long-term lithospheric deformation, especially, the formation of the inland sea and the uplift of the outer zone (Shikoku).

4.2. Geophysical data

4.2.1. Topography, Gravity, and Heat flow

A critical requirement is that our models match the observed gravity field, in particular, the non-isostatic equilibrium field. The *gravity residual anomaly* (GRA) is herein defined as the difference between the Bouguer gravity anomaly and the isostatic gravity anomaly calculated from topography, assuming Airy compensation, with a correction for the denser subducting oceanic plate (Huang et al. 1996a,b). The GRA is a measure of departure from isostatic equilibrium. A positive GRA indicates that topography is supported by a regional compressional stress.

The gravity data are Bouguer (on land) and free-air (at sea) taken from Kono and Furuse (1989). Gravity data and topographic/bathymetric data were projected along transect **AA'** and **BB'**, each 10 km wide and perpendicular to the Nankai Trough (Fig. 4.2). Figure 4.2 illustrates the topography and the GRA in southwest Japan. The gravity high at the outer arc is associated with a topographic high. The Philippine plate is much younger than the northeast Pacific plate with possibly buoyant subduction under southwest Japan (Sacks, 1983). The rigid part of the Philippine plate is about 50 km thick (Hirahara, 1981). The density contrast between the subducting rigid plate and the surrounding asthenosphere is assumed to be 0.1 g/cm^3 (Kono and Furuse, 1989; Mishina, 1990). The lower panel of figure 4.3 shows the geometry of the subducting plate, and the upper panel indicates the Bouguer gravity contribution.

Heat flow in the northern Chugoku region is higher (up to 2 HFU) because of the volcanic activity during the late Quaternary. The inland sea and the outer zone have lower heat flow, averaging 1-1.5 HFU. The Nankai trough has high heat flow, 2 -2.5 HFU. The heat flow in the trough is much greater than that in Japan trench because of the younger and hotter Philippine plate (Fig. 4.4).

4.2.2. Interplate seismicity

Two great earthquakes occurred recently along the Nankai trough: the 1946 Nankaido earthquake and the 1944 Tonankai earthquake (Fig. 4.5). The amount of slip is about 5 m along the subduction interface, and the slip direction makes a large angle with the strike of the Nankai trough. The oblique component contributes to the strike slip of the MTL. Other great earthquakes occurred in 1605, 1707, and 1854. The size and location of the aftershock zones for these great earthquakes are indicators of strong coupling along the interface between the subducting Philippine plate and the overriding southwest Japan plate.

4.3. Finite Element Modeling

4.3.1. Modeling Preliminaries

These modeling concepts are described in detail in Chapter 2 and Chapter 3. Here we give only a brief overview.

We have adapted the finite-element modeling code TECTON (Melosh and Raefsky, 1980; Wallace and Melosh, 1994) to analyze the deformation of folding of island arc lithosphere resulting from long-term subduction-related compressional forces using an appropriate rheological structure and faults. We modified TECTON (v1.5) to incorporate a simulation of stick-slip faulting, erosion and deposition as well as time-dependent loading. This allows us to monitor the long-term deformation of the island-arc lithosphere with forces resulting from the subduction of the Pacific plate as well as from the surface processes of erosion and deposition. Critical requirements we apply in our modeling are consistency with observed, present-day topography and gravity and explanation of seismicity patterns.

A starting model was built based on the published estimates of crustal thickness and estimates of viscosity structure (Hirahara, 1981; Hashimoto, 1982; Sacks, 1983). In our modeling, we assume a linear Maxwell visco-elastic rheology. We vary the viscosity structure and the interplate coupling to optimize the model fit to the observed topography, gravity, and seismicity patterns.

4.3.2 Model

The starting model is based on studies of crustal structures in southwest Japan (Hirahara, 1981; Sacks 1983; Geological Survey Japan, 1992). Surface and tectonic loading are imposed at the appropriate boundaries. We vary the viscosity structure and the interplate coupling to optimize the model fit to the observed topography and GRA.

The average dip of the main thrust between two plates is about 10 degrees, and the seismogenic thrust only extends under the Shikoku region to a 30 km depth (Fig. 4.5). The deeper part of the interface between the overriding plate and the subducting Philippine plate is not seismogenic. The study of three dimensional seismic structure by Hirahara (1981) reveals a flat

subducting Philippine plate beneath southwest Japan. The seismogenic part of the interface plays an important role in the deformation of the overriding plate.

The 2-D model is 800 km long, and 30 km thick (Fig. 4.6a). There are 3546 nodes and 3274 elements. A thinning of elastic layer in the Chugoku region is related to the volcanic activity in the Quaternary period. Figure 6b shows the finite-element grid of the model in the outer-arc area. Material properties are shown in Table 4.1. Viscosity of the lower crust (region 2, in Fig.4.6a) is varied in order to find a suitable viscosity of the lower crust which best fits the observed topography and gravity data. We consider four cases of viscosity (Model 1 to 4) as shown in Table 4.2. Gravitational body forces are included in the model. Over a long-term time scale, i.e., millions of years, the stress field approaches hydrostatic, because the differential stress will be diminished by viscous creep.

Table 4.1. Material properties of the model

Region	E (Pa s)	Density (kg/m ³)	Viscosity (Pa s)	Poison's ratio
1	5.5x10 ¹⁰	2600	elastic	0.25
2	5.5x10 ¹⁰	2600	1.0x10 ²²	0.25
3	5.5x10 ¹⁰	2600	1.0x10 ²²	0.25

Table 4.2. Viscosity of the lower crust (area 2 in figure 4.6).

Model	Viscosity (Pa s)
Model 1	1.0x10 ²¹
Model 2	1.0x10 ²²
Model 3	1.0x10 ²³
Model 4	1.0x10 ²⁴

3.3 Boundary Conditions

Surface Loads: Volcanic activity during the late Cenozoic in northern Chugoku provides a time-dependent loading on the plate. The rate of volcanic eruption is about 25 km³/km/Ma (Sugimura and Uyeda, 1973).

Tectonic Loads: The left (north) edge of the model is constrained to move in the vertical direction only, and vertical Winkler restoring forces are applied to the bottom of the mesh to simulate isostasy (Wallace and Melosh, 1994, Williams 1990, Huang et al., 1996a,b). The asthenosphere has a viscosity of 10¹⁹ Pas or less (Mizoue et al., 1983; Seno et al., 1993; Rydelek and Sacks, 1988, 1990). For the time scale of interest (5 Ma), the asthenosphere behaves as a

fluid. Therefore, the Winkler force approximately simulates an isostatic restoring force. For the right (south) edge, the vertical forces due to the oblique slab drag are specified. As discussed in the previous studies (Huang et al., 1996a,b), we also specify a horizontal displacement increment or velocity to simulate the horizontal pushing from the subducting plate. The displacement and force along the right (south) boundary are applied over the depth range 10-30 km. We consider three cases of coupling conditions along the interplate interface: uniform coupling with depth ($C_r=1$), 1.5-fold increasing coupling with depth, deeper region has greater coupling ($C_r=1.5$), and 2-fold increasing coupling with depth, deeper region has greater coupling ($C_r=2$). We also considered three cases of coupling magnitude: $C_0=1$ (a horizontal velocity of 1 mm/year), $C_0=1.5$ (a horizontal velocity of 1.5 mm/year) and $C_0=2.0$ (a horizontal velocity of 2 mm/year). The corresponding vertical force acting on the east edge is 3.75×10^{10} N ($C_0=1$), 5.625×10^{10} N ($C_0=1.5$), and 7.5×10^{10} N ($C_0=2.0$) at the central node of the coupled zone (Fig. 4.6).

4.3.4 Time history

The size of the time step varies during a model run. The first period has 100 time steps with a step size of 0.15 year. (A small time step for the initial stage helps stabilize the solution.) The second period has 2000 steps each 600 years long, while the last 2900 steps have a step size of 1200 year. The total number of time step is 5000, resulting in a total model run duration of 4.68 Ma.

4.4. Results

4.4.1 Effect of Lower-Crust Viscosity

As discussed in the next section, best results are found for a value of 1.5 for the coupling magnitude (C_0) and 2.0 for the coupling factor (C_r). With a different lower-crust viscosity, we compare the observed topography and gravity residual anomaly in **A-A'** and **B-B'** with the predicted values. Viscosity of the lower crust increases from 10^{21} to 10^{24} Pa s (Table 4.2). From figure 4.7, we observe that topography and GRA in the Shikoku region decreases as the viscosity of the lower crust increases. Viscosities of 10^{23} Pa s and 10^{24} Pa s are unacceptable because the resulting elevation in Shikoku is too low. A viscosity of 10^{21} Pa s or 10^{22} Pa s is acceptable.

4.4.2 Varying the Depth Dependence of Coupling

We first hold the coupling magnitude, C_0 , constant at 1.5 to assess the effect of different assumed coupling factor, C_r . Figure 4.8 shows the topography and gravity residual anomaly with uniform coupling ($C_r=1$), 1.5-fold increasing coupling ($C_r=1.5$), and 2-fold increasing coupling ($C_r=2$). Little difference is seen for the north coast area (Chugoku). $C_r=1$ does not match the topography and gravity high in the Shikoku region. $C_r=1.5$ slightly underestimates the topography and GRA in the outer arc region. $C_r=2.0$ results in acceptable matches for the topography and GRA in the outer arc region.

4.4.3. Varying the Coupling Magnitude

Next, with $C_r=1.5$, we examine the effect of different C_0 on topography and GRA. Figure 4.9 shows results when C_0 varies from 1 to 2. Topography and GRA in the land area decrease as coupling magnitude decreases. $C_0=1$ is unacceptable because the predicted topography and gravity are both too high. Although $C_0=2$ matches the observed data quite well, $C_0=1.5$ is a better match for topography and GRA near the outer-arc region.

4.4.4 Summary

From the above comparison, $C_r=1.5$ and $C_0=1.5$ with a lower-crust viscosity of 10^{22} Pa s or less fit best the observed data. The simple model explains the trend of topography and GRA in Shikoku and the inland sea.

4.5 Discussion

4.5.1. Topography and Gravity in the Outer-Arc Slope

Although we have tried different combinations of viscosity in the lower crust, and force system along plate interface, topography and GRA in the outer arc slope adjacent to the Nankai trough do not match the observed values very well. The mismatch may be due to a more complicated sediment deposition and accretion of oceanic sediment on the outer arc slope along Nankai trough.

4.5.2 Topography and Gravity in Shikoku Region

The mountain range in Shikoku, was uplifted about 1 km during the last 5 million years. The uplift rate is about 0.2 mm/year. From the tide gauge records, a steady interseismic uplift rate was obtained over the interseismic interval (about 115 years). The maximum uplift rate is about 4 mm/year. Thus, the long-term uplift rate of the outer arc is an order of magnitude smaller than the uplift rate during the recurrence interval of the great interplate earthquakes. The discrepancy is related to the difference between steady-state subduction and slip during interplate earthquakes, as well as ignoring the effect of the Medium Tectonic Line (MTL). The discontinuity along the MTL could cause more uplift at the Shikoku region.

In the Chugoku region, topography was underestimated by the model, although the predicted GRA matches the gravity very well. This may be due to the simple assumption of the complex geological structure related to earlier volcanic activity. Probably the elastic thickness under the volcanic line is smaller than that in this model. The present GRA is partially due to the positive density contract under the volcanoes in the model (see figure 6a and Table 4.1).

4.5.3 Interplate seismicity and coupling

We have shown that interplate coupling seems to correlate well with the interplate seismicity in northeast Japan (Huang et al., 1996b). Coupling along the interplate interface affects the topography and gravity signature. Southwest Japan has a higher coupling magnitude, $C_0=1.5$ vs. $C_0 = 1$ in the off-Sanriku region of northeast Japan. As we discussed in Huang et al. (1996b), great interplate earthquakes appear to require strong coupling between the subducting and overriding plates. Southwest Japan has great, shallow interplate thrust earthquakes ($M>8.0$ every 150 years), which supports our suggestion.

4.6. Conclusions

Based on a simple rheology model for the overriding plate and a force system involving the subducting Philippine plate, we are able to explain the formation of Shikoku and the inland sea. The viscosity of the lower crust is determined to be no more than 10^{21} Pa s. Coupling magnitude is 1.5, and coupling ratio is 2.0. Interplate coupling in southwest Japan is greater than that in off-Sanriku of northeast Japan ($C_0=1.0$, $C_r=2.0$, Huang, et al., 1996a,b).

The inland sea is caused by shallow flexural warp adjacent to the upwarps of the Shikoku and Chugoku regions under the long-term subduction forces.

Strong interplate coupling is a key factor controlling the deformation of the island arc lithosphere in southwest Japan.

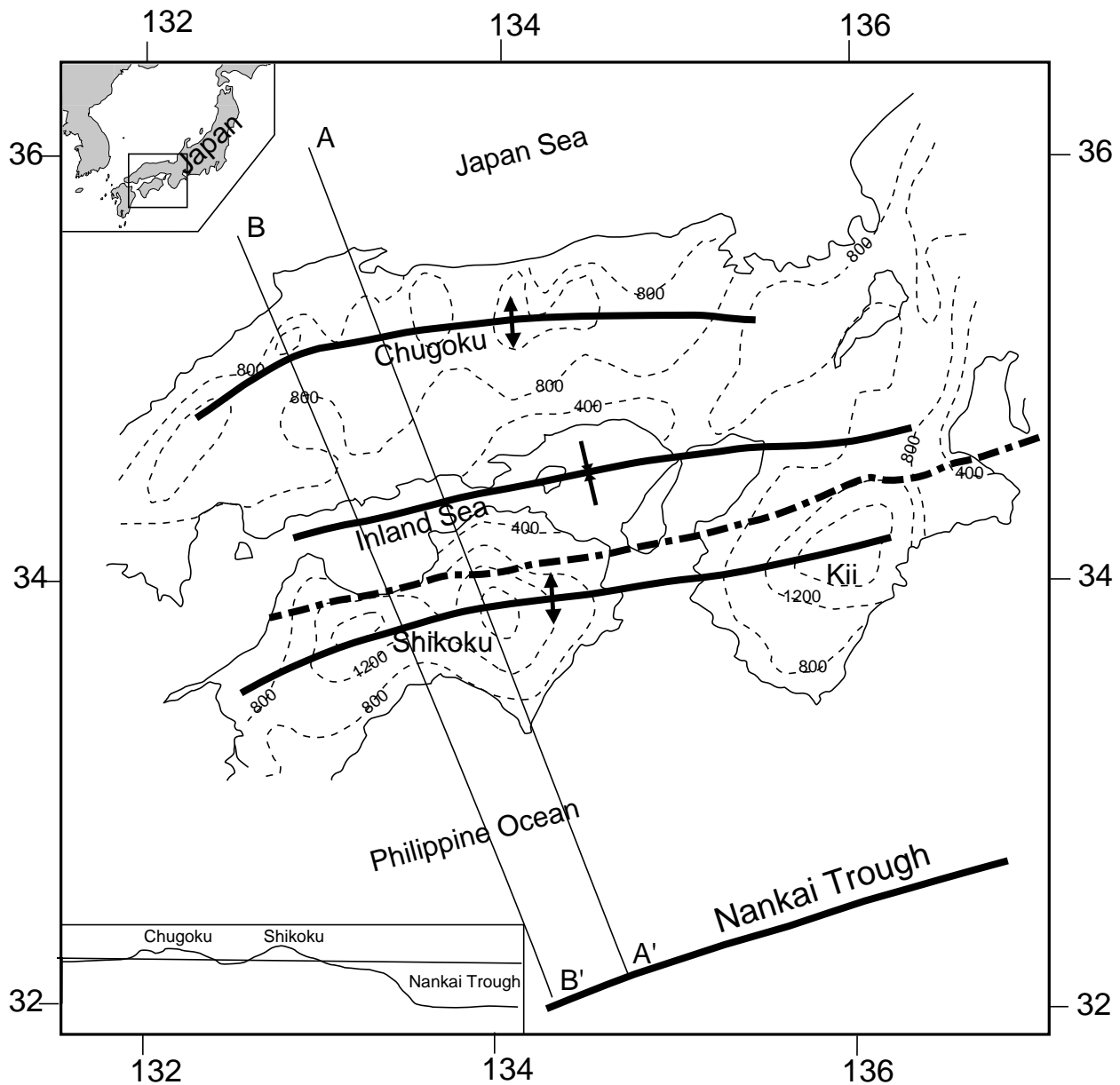


Figure 4.1: Study area of southwest Japan. The thin solid line is the coastal line. The thin dashed line denotes the elevation contours, and the contour interval is 400 m. Thick line shows the axes of uplift zones (with outward arrows) and subsidence zone (with inward arrows). The thick, dot and dashed line denotes the Medium Tectonic Line (MTL). Two profiles **AA'** and **BB'** are about perpendicular to the Nankai trough. The left upper inlet shows the location of southwest Japan, and the left lower inset shows a simplified elevation profile from the north coast to the south coast. (adapted from Fig. 10.10 of M. Hashimoto, 1991.)

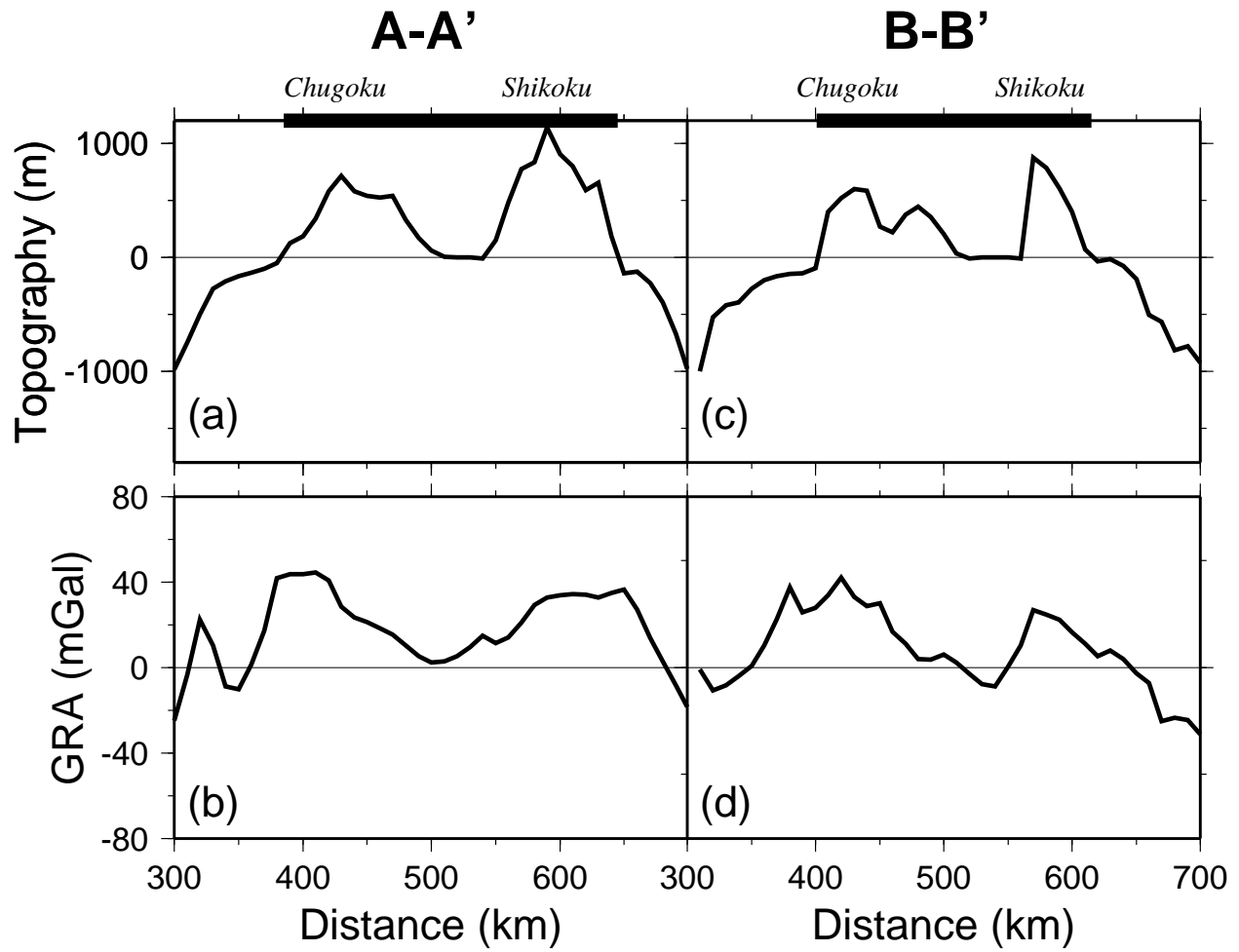


Figure 4.2: Topography and gravity residual anomaly (GRA) profiles along **A-A'** (a,b) , and **B-B'** (c,d) in southwest Japan. Both Shikoku and Chugoku have high topography and high gravity residual anomaly (GRA).

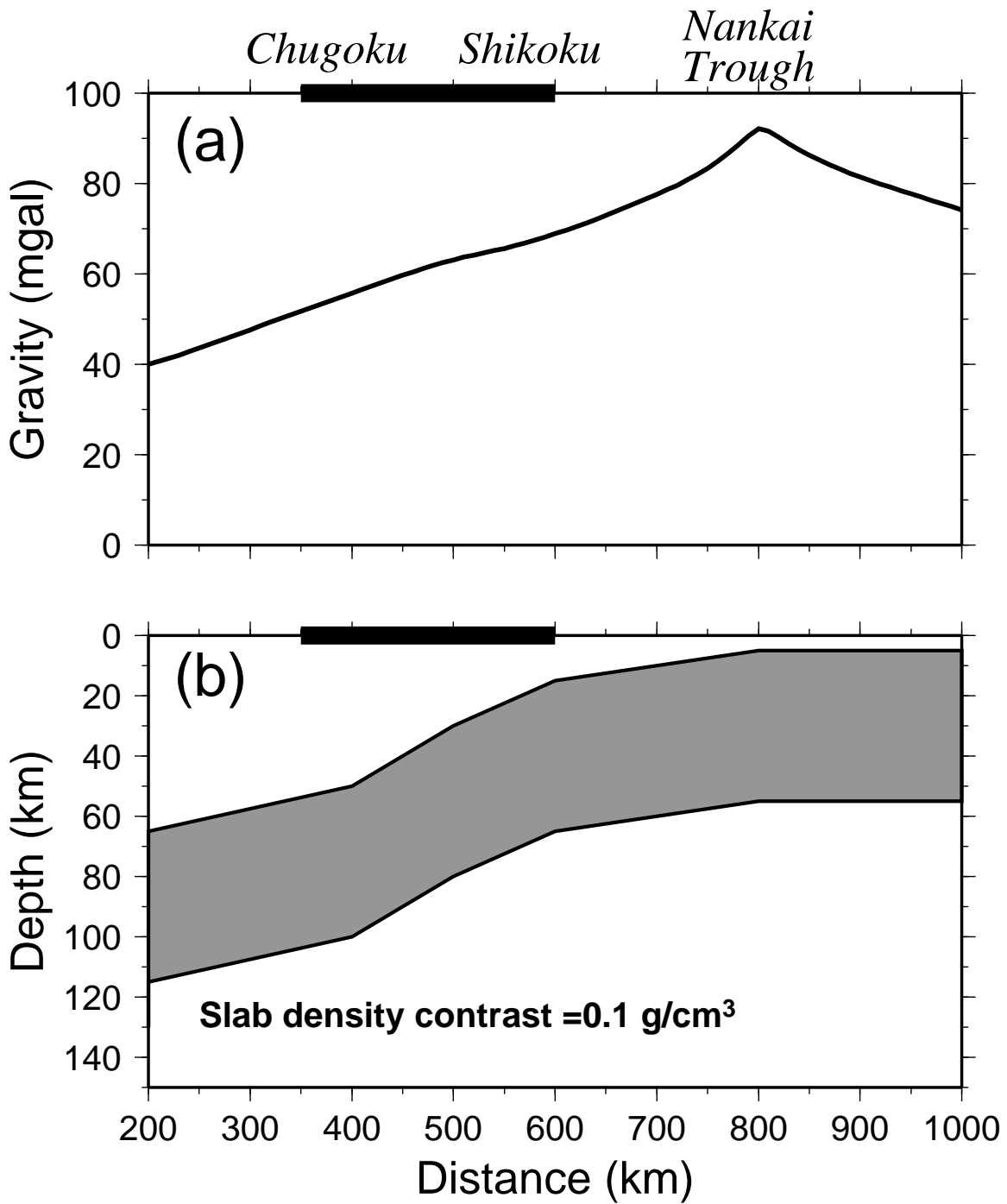


Figure 4.3: The gravitational effect of the dense subducting Philippine plate. (a) The gravity signature from the subducting plate; (b) Geometry of the subducting plate. The density contrast between the subduction plate and the adjacent asthenosphere is 0.1 g/cm³.

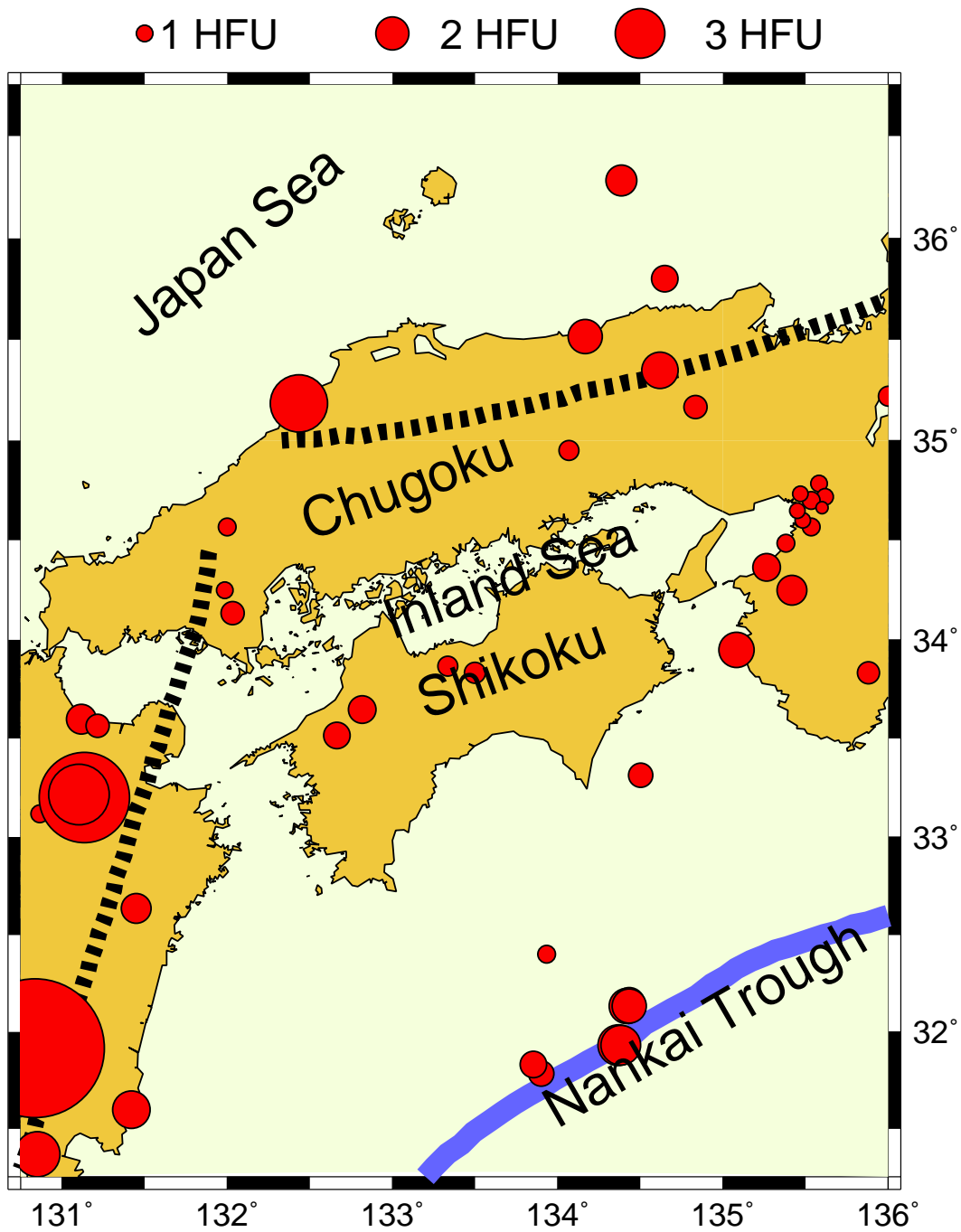


Figure 4.4: Heat Flow in southwest Japan. The solid circle represents location of heat flow measurements, as well as its magnitude. The thick, dashed line indicates the active volcanic line in the late Quaternary. The thick, solid line indicates the Nankai trough.

1944 + 1946 Fault Model

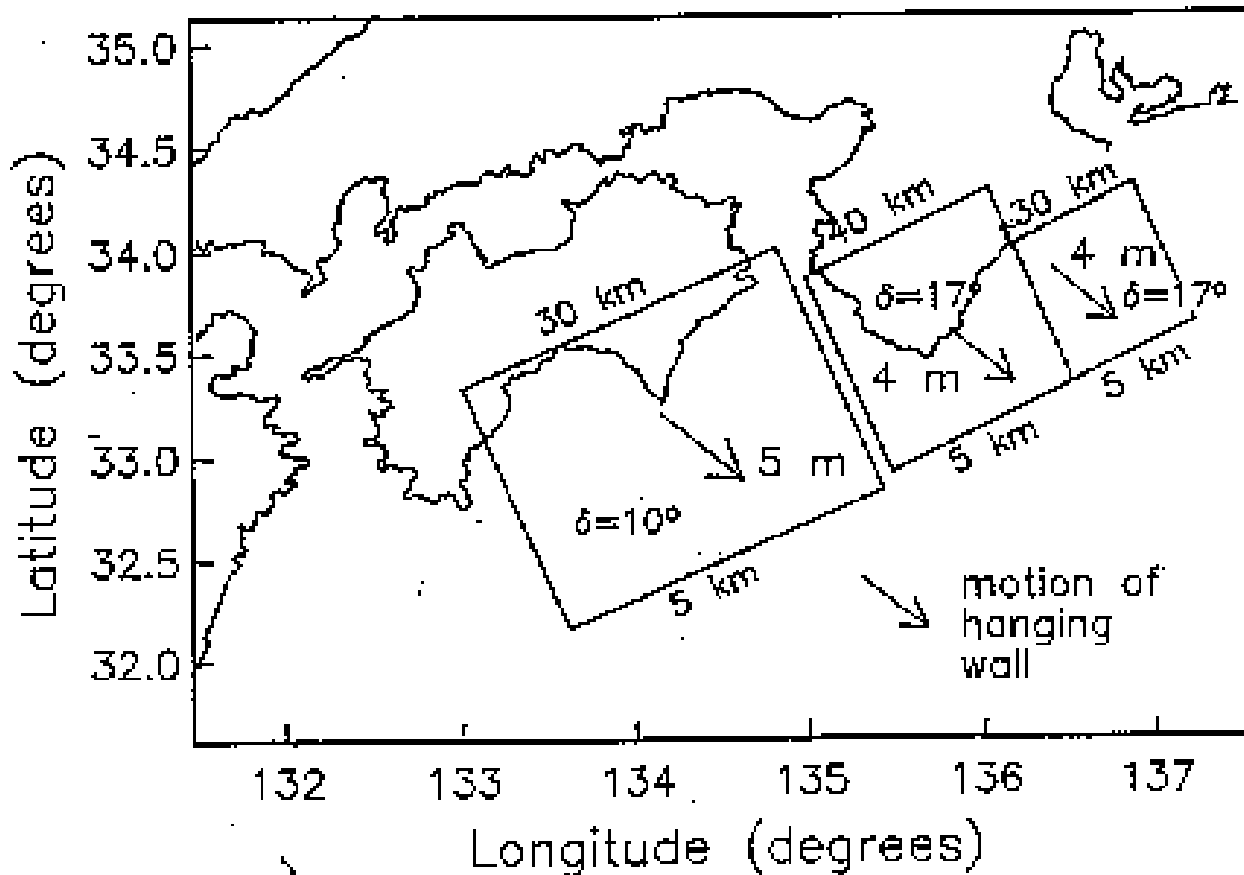


Figure 4.5: Fault model of the combined 1944 and 1946 Philippine Sea interplate events. The top and bottom fault depth, dip, and slip, are indicated. The dips are constrained by microseismicity (Mizoue, M., Nakamura, M., Seto, N., Ishiketa, Y., and Yokota, T., 1983), and the slip directions agree with the relative plate motion direction determined by Seno, T., Stein, S., and Gripp, A. (1993).

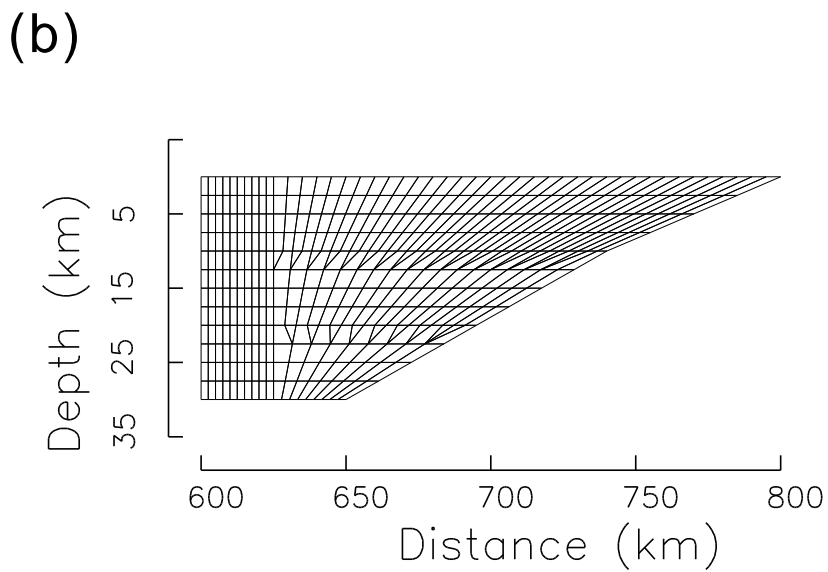
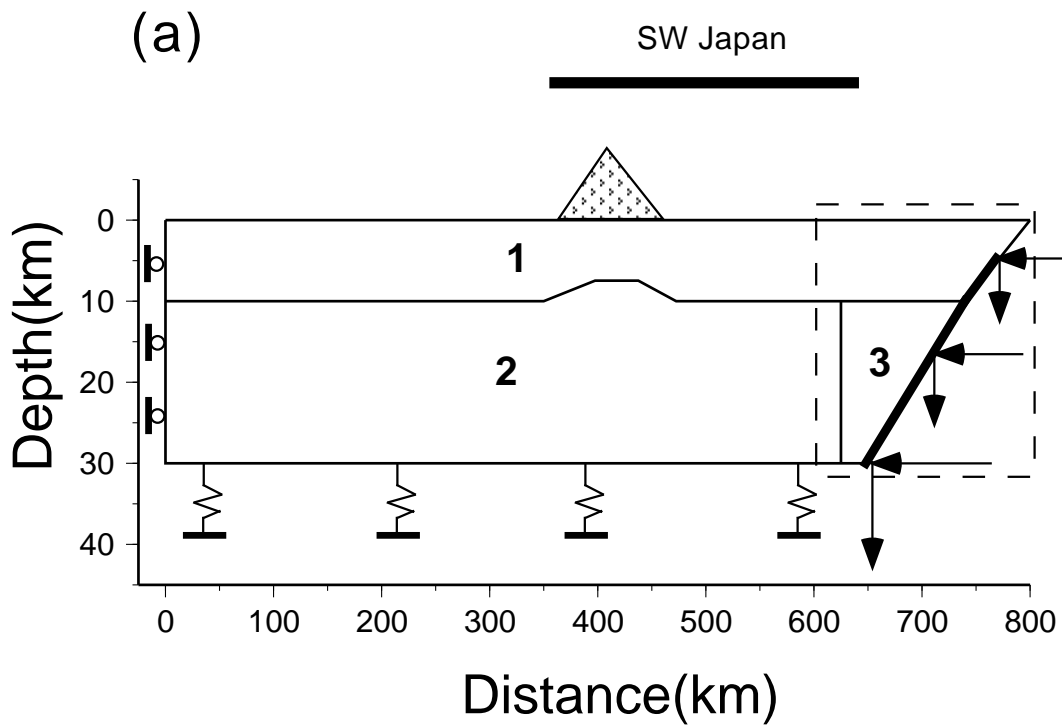


Figure 4.6: Finite element model. (a) The boundary conditions and the material properties of the model (see text for details). (b) The finite-element grid in the outer arc region of the model, which is show by a rectangle with dashed line in (a).

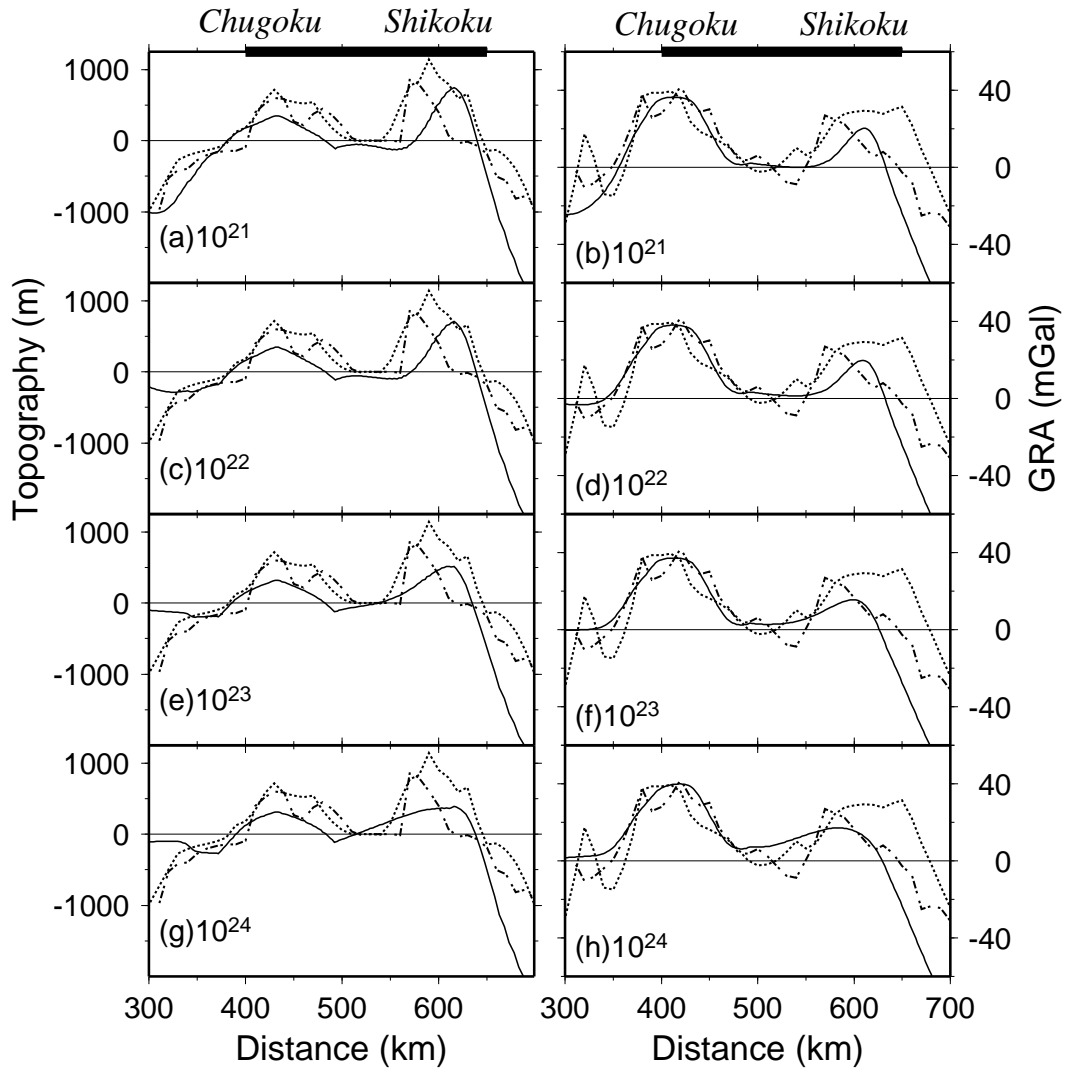


Figure 4.7: Effect of lower crust viscosity on topography (left panel) and gravity residual anomaly (right panel). a,b) Model 1, lower crust viscosity is 10^{21} Pa s; c,d) Model 2, lower crust viscosity is 10^{22} Pa s; e,f) Model 3, lower crust viscosity is 10^{23} Pa s; g,h) Model 4, lower crust viscosity is 10^{24} Pa s. Solid line denotes the topography or GRA calculated from finite element modeling. The dotted line shows observed topography or GRA of profile **A-A'**, and the dot-dashed line indicates profile **B-B'**.

Coupling Magnitude, $C_0=1.5$

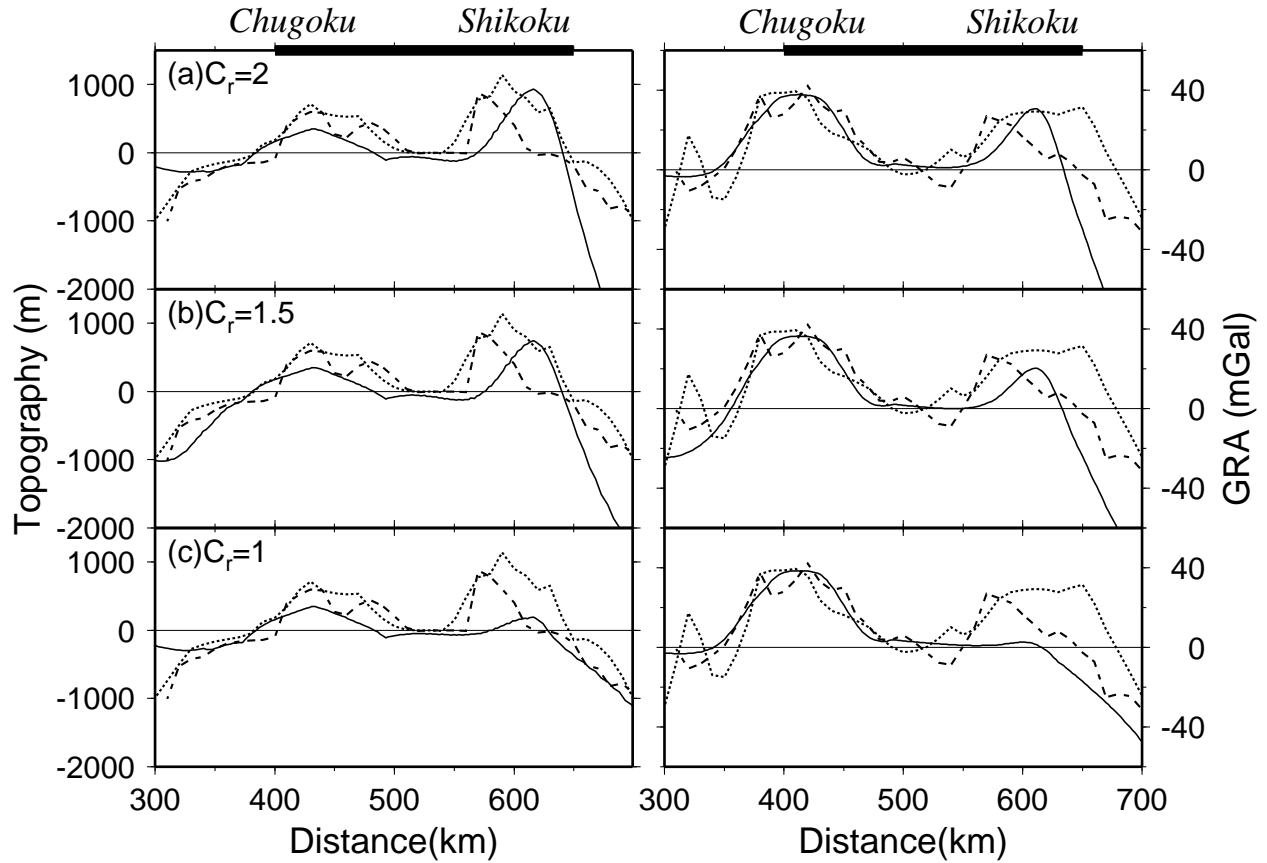


Figure 4.8: Effect of C_r on topography (left) and GRA (right) in southwest Japan. In all cases, $C_0=1.5$. (a) 2-fold of increasing coupling ($C_r=2$). (b) 1.5-fold of coupling ($C_r=1.5$). (c) uniform coupling ($C_r=1$). Solid lines represent the computed values. Dotted lines show the observed values along the profile **A-A'**, and the long-dashed lines the values along profile **B-B'**.

Coupling Ratio, $C_r = 1.5$

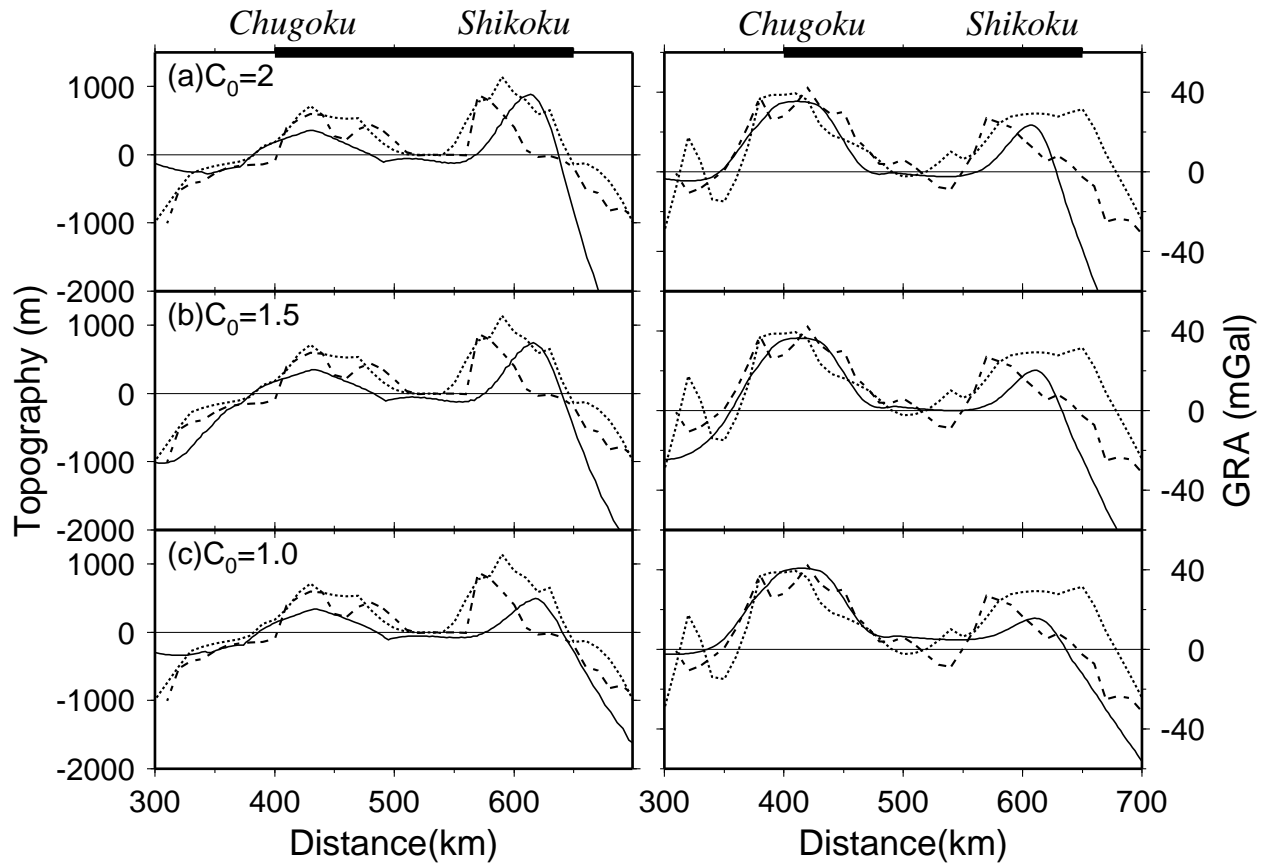


Figure 4.9: Effect of C_0 on topography (left) and gravity (right) in southwest Japan. C_r is 1.5 for all three cases. (a) $C_0=1$; (b) $C_0= 1.5$; (c) $C_0=2.0$. Solid lines represent the computed values. Dotted lines show the observed values along the profile **A-A'**. The long-dashed line represents the data along profile **BB'**.

Bibliography

- Aubouin, J., 1989. Some aspects of the tectonics of subduction zones, *Tectonophysics*, 160, 1-21.
- Bodri, B., S. Iizuka, and M. Hayakawa, 1991. Geothermal and rheological implications of intracontinental earthquakes beneath the Kanto-Tokai region, Central Japan, *Tectonophysics*, 194, 337-347.
- Byerlee, J. D., 1967. Theory of friction based on brittle fracture, *J. Appl. Phys.*, 38, 2928-2934.
- Byrne, D. E., D. M. Davis, and L. R. Sykes, 1988. Loci and maximum size of thrust earthquakes and the shallow region of subduction zones, *Tectonics*, 7, 4, 833-857.
- Carter, N., and M. C. Tsenn, 1987. Flow properties of continental lithosphere, *Tectonophysics*, 136, 27-63.
- Fitch, T. J., 1972, Plate convergence, transcurrent faults, and internal deformation adjacent to southeast Asia and the western Pacific, *J. Geophys. Res.*, 77, 4432-4460.
- Furukawa Y., and S. Uyeda, 1989. Thermal state under the Tohoku Arc with consideration of crustal heat generation, *Tectonophysics*, 164, 175-187.
- Geological Survey of Japan, 1968. Geological map of Japan, 1:2000000, Kawasaki.
- Geological Survey of Japan, 1992. Geological atlas of Japan (second edition), Asakura Publishing Co. Ltd.
- Handin, J., 1969. On the Coulomb-Mohr failure criterion, *J. Geophys. Res.*, 74, 5343-5348.
- Hasegawa, A., N. Umino, and A. Takagi, 1985. Seismicity in the Northeastern Japan Arc and Seismicity Patterns before Large Earthquakes, *Earthq. Predict. Res.*, 3, 607-626.
- Hasegawa, A., S. Horiuchi, and Norihito Umino, 1994. Seismic structure of the Northeastern Japan convergent margin: A synthesis, *J. Geophys. Res.*, 99, 22,295-22.311.
- Hasegawa, A., Umino, N., Takagi, A., Suzuki, S., Motoya, Y., Kameya, K., Tanaka, K., and Sawada, Y., 1983. Spatial distribution of earthquakes beneath Hokkaido and northern Honshu, Japan, *Zisin*, 36, 129-150.
- Hashimoto, M. (Eds.), 1991. *Geology of Japan*, Terra Scientific Publishing Company/Tokyo, Kluwer Academic Publishers, 249pp.
- Hashimoto, M., 1981. Three-dimensional stress distribution in southwestern Japan as expected from the configuration of the subducting Philippine Sea plate (Part 2), *Zisin*, 34, 197-211 (in Japanese).
- Hashimoto, M., 1984. Finite element modeling of deformations of the lithosphere at an arc-arc junction, The Hokkaido corner, Japan, *J. Phys. Earth*, 32, 373-398.
- Hashimoto, M., 1985. Finite element modeling of the three-dimensional tectonic flow and stress field beneath the Kyushu island, Japan, *J. Phys. Earth*, 33, 191-226.
- Hashimoto, Mitsuo, 1991, *Geology of Japan*, Terra Scientific publishing company, Tokyo.
- Hashizume, M., K. Ito, and T. Yoshii, 1981. Crustal structure of south-western Honshu, Japan and the nature of the Mohorovicic discontinuity, *Geophys. J. R. astr. Soc.* 66, 157-168.
- Hirahara K., 1981, Three-dimensional seismic structure beneath southwest Japan: the subducting Philippine sea plate, *Tectonophysics*, 79, 1-44.

- Huang, S. , I. S. Sacks, and J. A. Snoke, 1996a. Compressional deformation of island arc lithosphere in NE Japan resulting from long-term subduction-related tectonic forces: finite element modeling, Submitted to Tectonophysics.
- Huang S., I. S. Sacks and J. A. Snoke, 1996b. Topographic and seismic effects of long-term coupling between the subducting and overriding plates beneath northeast Japan, tectonophysics, in press.
- Huene, R. von, and R. Culotta, 1989. Tectonic erosion at the front of the Japan Trench convergent margin, Tectonophysics, 160, 75-90.
- Huene, R. von, D. Klaeschen, and B. Cropp, 1994. Tectonic structure across the accretionary and erosional part of the Japan Trench margin, J. Geophys. Res., 99, B11, 22,349-22,361.
- Kanamori, H., 1972. Tectonic implications of the 1944 Tonankai and the 1946 Nankaido earthquakes, Phys. Earth Planet. Interiors 5, 129-139.
- Karner, G. D., and J. K. Weissel, 1990. Factors controlling the location of compressional deformation of oceanic lithosphere in the Central Indian Ocean, J. Geophys. Res., 95, B12, 19,795-19,810.
- Kawakatsu, H., and T. Seno, 1983. Triple seismic zone and the regional variation of seismicity along the Northern Honshu Arc, J. Geophys. Res., 88, B5, 4215-4230.
- King, G.P., R. S. Stein, and J. B. Rundle, 1988. The growth of geological structures by repeated earthquakes, 1. Conceptual framework, J. Geophys. Res., 93, B11, 13,307-13,318.
- Kono, Y., and N. Furuse, 1989. 1:1 million scale gravity anomaly map in and around the Japanese Islands (in Japanese), 76pp., University of Tokyo Press, Tokyo, Japan.
- Lambeck, K., 1983a. The role of compressive forces in intracratonic basin formation and mid-plate orogenies, Geophys. Res. Lett., 10, 845-848.
- Lambeck, K., 1983b. Structure and evolution of the intracratonic basins of central Australia, Geophys. J. R. Astron. Soc., 74, 843-886.
- Martinod, J., and P. Davy, 1992. Periodic instabilities during compression or extension of the lithosphere: 1. Deformation modes from an analytical perturbation method, J. Geophys. Res., 97, 1999-2014.
- Martinod, J., and P. Davy, 1994. Periodic instabilities during compression of the lithosphere: 2. Analogue experiments, J. Geophys. Res., 99, 12,057-12,069.
- Matsu'ura, M. and T. Sato, 1989, A dislocation model for the earthquake cycle at convergent plate boundaries, Geophys. J. int., 96, 23-32
- Matsuda, T., H. Yamazaki, T. Nakata, and T. Imaizumi, 1980. The surface faults associated with the Rikuu earthquake of 1896, Bull. Earthq. Res. Inst., Univ. of Tokyo, 55, 795-855.
- Matsuda, T., K. Nakamura, and A. Sugimura, 1967. Late Cenozoic orogeny in Japan, Tectonophysics, 4, 349-366.
- McAdoo, D. C., and D. T. Sandwell, 1985. Folding of oceanic lithosphere, J. Geophys. Res., 90, 8563-8568.
- Melosh, H. J., and A. Raefsky, 1980. The dynamical origin of subduction zone topography, Geophys. J. R. astr. Soc. 60, 333-354.
- Melosh, H. J., and C. A. Williams, 1989. Mechanics of graben formation in crustal rocks: a finite element analysis, J. Geophys. Res., 94, 13,961-13,973.

- Mishina, 1990, Gravity anomaly of the island arc in northeast Japan, dissertation of Tohoku University. (in Japanese)
- Miyashiro, A. 1961. Evolution of metamorphic belts. *J. Petrol.*, 2, 277-311.
- Mizoue, M., Nakamura, M., Seto, N., Ishiketa, Y., and Yokota, T., 1983. II. Three-layered distribution of microearthquakes in relation to focal mechanism variation in the Kii Peninsula, southwestern Honshu, *Japan Bull. Earthq. Res. Inst.* 58, 287-310 .
- Ohmori, H. 1978. Relief structure of the Japanese mountains and their stages in geomorphic development, *Bull. Dept. Geog., Univ. Tokyo*, 10, 31-85.
- Okubo, Y. and T. Matsunaga, 1994. Curie point depth in northeast Japan and its correlation with regional thermal structure and seismicity, *J. Geophys. Res.*, 99, 22,363-22,371.
- Okubo, Y., H. Tsu, and K. Ogawa, 1989. Estimation of Curie point temperature and geothermal structure of island arcs of Japan, *Tectonophysics*, 159, 279-290.
- Okubo, Y., M. Makino, and S. Kasuga, 1991. Magnetic model of the subduction zone in the northeast Japan Arc, *Tectonophysics*, 192, 103-115.
- Pollack, H., S. J. Hurter, and J. R. Johnson, 1993. Heat flow from the earth's interior: analysis of the global data set, *Review of Geophysics*, 31 (3), 267-280.
- Research Group for Active Faults of Japan, 1991. 1:1 million Active Fault Map of Japan, University of Tokyo Press.
- Research Group for Explosion Seismology, 1977. Regionality of the upper mantle around northeastern Japan as derived from explosion seismic observations and its seismological implications, *Tectonophysics*, 37, 117-130.
- Research Group for Quaternary Tectonic map, 1973, Explanation text of the Quaternary tectonic map of Japan, Tokyo.
- Rydelek, P. A., and I. S. Sacks, 1988. Asthenospheric viscosity inferred from correlated land-sea earthquakes in north-east Japan, *Nature*, 336, 234-237.
- Rydelek, P. A., and I. S. Sacks, 1990. Asthenospheric viscosity and stress diffusion: a mechanism to explain correlated earthquakes and surface deformations in NE Japan, *Geophys. J. Int.*, 100, 39-58.
- Sacks, I. S., 1983. The subduction of young lithosphere, *J. Geophys. Res.*, 88, 3355-3366.
- Sato H., 1986. Geological development of the Cenozoic system in central northeast Honshu (between Sakata and Furukawa) (in Japanese with English abstract). *Contrib. Inst. Geol. Paleontol. Tohoku Univ.*, 88/89, 1-32, 1-45.
- Sato, H. 1994. The relationship between late Cenozoic tectonic events and stress field and basin development in northeast Japan, *J. Geophys. Res.*, 99, 22,261-22,274.
- Sato, K., 1988. Stress and displacement fields in the northeastern Japan Island Arc as evaluated with three-dimensional finite element method and their tectonic interpretations, *Tohoku geophysical Journal*, 31, 57-99.
- Sato, T., and Matsu'ura, M., 1988, A kinematic model for deformation of the lithosphere at subduction zones, *J. Geophys. Res.*, 93, 6410-6418.
- Sato, T., and Matsu'ura, M., 1992. Cyclic crustal movement, steady uplift of marine terraces, and evolution of the island arc-trench system in southwest Japan, *Geophys. J. Int.*, 111, 617-629.
- Sato, T., and Matsu'ura, M., 1993. A kinematic model for evolution of island arc-trench systems, *Geophys. J. Int.*, 114, 512-530.

- Savage, J. C., and W. Thatcher, 1992. Interseismic deformation at the Nankai Trough, Japan, subduction zone, *J. Geophys. Res.*, 97, 11,117-11,135.
- Scholz C. H., and J. Campos, 1995. On the mechanism of seismic decoupling and back arc spreading at subduction zones. *J. Geophys. Res.*, 100, 22,103 - 22,115.
- Segawa J., and Y. Tomoda, 1976. 3. Gravity measurements near Japan and study of the upper mantle beneath the oceanic trench-marginal sea transition zones, in *Geophysics of the Pacific basin and its margin: a volume in honor of George P. Woollard*, AGU, pp. 35-52.
- Seno, T., S. Stein, and A. Gripp, 1993. A model for the motion of the Phillipine Sea plate consistent with Nuvel-1 and geological data, *J. Geophys. Res.* 98 17,941-17,948.
- Shimazaki, K., 1974. Pre-seismic crustal deformation caused by an underthrusting oceanic plate in eastern Hokkaido, Japan, *Phys. of the Earth and Planet. Interiors*, 8, 148-157.
- Shimazaki, K., 1976. Intra-plate seismicity and inter-plate earthquakes: historical activity in Southwest Japan, *tectonophysics*, 33, 33-42
- Shiono, K., 1977. Focal mechanisms of major earthquakes in Southwest Japan and their tectonic significance, *J. phys. Earth*, 25, 1-26.
- Stephenson, R. A., and S. A. Cloetingh, 1991. Some examples and mechanical aspects of continental lithospheric folding, *Tectonophysics*, 188, 27-37.
- Stephenson, R. A., B. D. Ricketts, S. A. Cloetingh, and F. Beekman, 1990, Lithosphere folds in the Eureka Orogen, Arctic Canada? *Geology*, 18, 603-606.
- Sugimura, A., and S. Uyeda, 1973. *Island Arcs: Japan and Its Environs*, 247pp., Elsevier Scientific Publishing Company, Amsterdam - London -New York.
- Suyehiro, K. and A. Nishizawa, 1994. Crustal structure and seismicity beneath the forearc off northeast Japan, *J. Geophys. Res.*, 99, 22,331-22,347.
- Takami, K., 1988, Geological structure of the Japan Sea and its tectonic implications, *Bulletin of the Geological Survey of Japan*, 39, 269-365.
- Tanioka Y., L. Ruff and K. Satake, 1993. Unusual rupture process of the Japan sea earthquake, *EOS Transactions, AGU*, 74, August 24.
- Thatcher, W., 1984. The earthquake deformation cycle at the Nankai Trough, Southwest Japan, *J. Geophys. Res.*, 89, 3087-3101.
- The Regional Subcommittees Of The Coordinating Committee Forearthquake Prediction, 1994 Summary of observations for earthquake prediction in Japan (part 3), Kinki, Chugoku, Shikoku, Kyushu and Okinawa areas; edited by Geographic survey institute, ministry of construction, Japan.
- Turcotte, D. and G. Schubert, 1982. *Geodynamics: Applications of Continuum Physics to Geological Problems*, 450pp., John Wiley and Sons, New York.
- Unimo, N., A. Hasegawa, and T. Matsuzawa, 1995. sP depth phase at small epicentral distances and estimated subducting plate boundary, *Geophys. J. Int.*, 120, 356-366.
- Wallace, M. H., and H. J. Melosh, 1994. Buckling of a pervasively faulted lithosphere, *PAGEOPH*, 142, 239-261.
- Wang, C. Y., 1980. Sediment subduction and frictional sliding in a subduction zone, *Geology*, 8, 530-533.
- Watts, A. B., 1992. The effect elastic thickness of the lithosphere and the evolution of foreland basins, *Basin Research*, 4, 169-178.

- Weissel, J. K., R. N. Anderson, and C. A. Geller, 1980. Deformation of the Indo-Australian plate, *Nature*, 287, 284-291.
- Wesnousky, S.G., G. H. Scholz, and K. Shimazaki, 1982. Deformation of an island arc: Rates of moment release and crustal shorting in intraplate Japan determined from seismicity and Quaternary fault data, *J. Geophys. Res.*, 87, 6829-6852.
- Wessel, P. and W. H. F. Smith, 1991, Free Software helps map and display data, *EOS Trans., AGU*, 72, 441.
- Wessel, P., and W. H. F. Smith, 1993. The GMT-SYSTEM v. 2.1.4 Technical Reference & Cookbook, SOEST/NOAA.
- Wilks, K. R., and N. L. Carter, 1990. Rheology of some continental lower crustal rocks, *Tectonophysics*, 182, 57-77.
- Williams, C. A., 1990. Numerical Modeling of Fault Formation and the Dynamics of Existing Faults, Ph.D. Dissertation, University of Arizona.
- Yamazaki, K., T. Tamura and I. Kawasaki, 1985. Seismogenic stress field of the Japan Sea as derived from shallow and small earthquakes (in Japanese with English abstract), *J. Seismo. Soc. Jpn.*, 38, 541-558.
- Yoshii, T., 1979. A detailed cross-section of the deep seismic zone beneath northeastern Honshu, Japan, *Tectonophysics*, 55, 349-360.
- Yoshioka, S., and M. Hashimoto, 1989. A quantitative interpretation on possible correlations between intraplate seismic activity and interplate great earthquakes along the Nankai Trough, *Phys. Earth Planet. Int.*, 58, 173-191.
- Zhao, D., A. Hasegawa, and H. Kanamori, 1994. Deep structure of Japan subduction zone as derived from local, regional, and teleseismic events, *J. Geophys. Res.*, 99, 22,313-22,329.
- Zhao, D., Horiuchi, and A. Hasegawa, 1992, Seismic velocity structure of the crust beneath the Japan Islands, *Tectonophysics*, 212, 289-301.
- Zuber, M.T., 1987. Compression of oceanic lithosphere: An analysis of intraplate deformation in the central Indian Basin, *J. Geophys. Res.*, 92, 4817-4825.

Appendix A: Calculation of the gravity residual anomaly from a deformed FEM mesh

Gravity (Bouguer gravity) and the gravity residual anomaly of the deformed FEM mesh are calculated by finite-element modeling. In order to calculate the Bouguer gravity of the deformed model, gravity from the deformed mesh (g_m) is computed first. g_m is defined as the gravity signature of all elements. If an element is not totally below sea level, only the part of the element below sea level contributes to the gravity signature. Gravity from the less dense sedimentary rocks (g_d) also contributes to the total Bouguer gravity. For the land area, a terrain correction (g_t) is also applied. Seawater adds another gravity component, g_w . Adding g_m , g_t , g_d and g_w together yields the Bouguer gravity on land and the free-air gravity for the sea. An additional correction (g_c) is calculated to convert the marine free-air gravity to Bouguer gravity. Thus, Bouguer gravity for the FEM model is

$$g_b = g_m + g_t + g_d + g_w + g_c$$

The isostatic correction (g_i) is calculated from the topography with the assumption of a 30 km thick crust at the coastline. Therefore, the gravity residual anomaly (g_{res}) is

$$g_{res} = g_b - g_i$$

We incorporated the gravity-residual calculation into a TECTON postprocessing code using the GMT package (Wessel and Smith, 1993). The gravity residual anomaly is a measure of isostatic equilibrium for the deformed model. Figure 2.6 shows two cases of isostatic compensation. For Airy compensation, i.e., a mountain has its root, the gravity residual anomaly is zero. If the lithosphere folds, a high, positive gravity residual anomaly is observed at the elevation peak.

Appendix B: Failure criterion

Stress, including its variations in time and space, plays a critical role in the determination of failure of the earth rock. The state of stress can be described by the three principal stresses: σ_1 , σ_2 , and σ_3 , i.e., which are ordered from largest to smallest.

The Mohr-Coulomb failure criterion is based on an assumed linear relationship between the shear stress and the normal stress:

$$\tau_{failure} = c + \sigma_n \tan \phi$$

where τ is the shear stress, σ the normal stress, c the cohesive strength of the rock and ϕ the angle of internal friction. Failure occurs when the Mohr circle first touches the failure envelope. This occurs when the radius of the Mohr circle, $(\sigma_1 - \sigma_2) / 2$, is equal to the perpendicular distance from the center of the circle, $(\sigma_1 + \sigma_2) / 2$, to the failure envelope,

$$\left(\frac{1-\mu}{2}\right)_{failure} = c \cos \alpha + \left(\frac{1+\mu}{2}\right) \sin \alpha$$

The proximity to failure (PTF) is defined as the ratio between the actual radius of the Mohr circle, $(\sigma_1 - \sigma_2) / 2$, and the radius at failure,

$$PTF = \frac{\left(\frac{\sigma_1 - \sigma_2}{2}\right)}{\left(\frac{\sigma_1 - \sigma_2}{2}\right)_{failure}}$$

When the $PTF < 1$, the stress is within the failure envelope, but when the $PTF = 1$, failure occurs.

Appendix C: Implementation of erosion and deposition

The rearrangement of surface mass by erosion and deposition is very important to the displacement field and stress state of a deformable lithosphere. We modified and implemented the scheme of erosion and deposition by T. Sato & M. Matsu'ura (1993) for use in TECTON. Erosion and deposition cause modification of surface topography as well as loading and unloading on the lithosphere. Erosion is treated as a set of positive loads (i.e. upward force) acting at the top of plate, while sedimentation is treated as a set of negative loads. An observation about the state of erosion and deposition in Japan is that the rate of erosion for the mountainous regions is in proportion to the square of land height (Ohmori, 1978):

$$d = c * h^2$$

where d is the rate of erosion/deposition, h the height/depth, and c an erosion constant.

This scheme is appropriate for erosion, but not for deposition, because in this model, the amount of deposition is dependent on only the depth. This is not quite right, especially when there is an adjacent mountain range. The consequence of the above simple function is that the amount of erosion may not equal the amount of deposition. In our application, we maintain an equilibrium between the amounts of erosion and deposition. The amount of deposition is therefore scaled to balance the erosion. The computer implementation takes into account two constraints: a) the rate of erosion/deposition is proportional to height/depth; and b) the conservation of mass.

The implementation procedure is shown as follows: 1) evaluate topography at each time step to find out where erosion or deposition occurs (erosion occurs when topography is above sea level, and deposition occurs when topography is below sea level.); 2) compute the thickness of mass removed by erosion (or added by deposition) during one time step; integrate the volume of erosion and deposition along the profile; determine a scale factor defined by the ratio between the total amounts of erosion and deposition. The final amount of deposition is obtained by multiplying

the deposition by the scale factor; 3) the amount of erosion/deposition on each node is then converted to gravitational forces, which are added to the global forces at the nodes where erosion/deposition occurs; 4) compute displacement due to loading and unloading governed by the updated force system and the existing boundary condition; 5) update the topography with the thickness of mass removed by erosion or added by deposition, and the displacement due to loading and unloading, then go to the next time step based on the same procedure as described above.

The computational algorithm is given by

$$W(x, n \ t) = W_f(x, n \ t) + \sum_{k=1}^n W_e(x, k \ t)$$

and

$$W_f(x, n \ t) = W_i(x, n \ t) + \sum_{k=1}^n W_r(x, k \ t)$$

where W is the total displacement, W_e the thickness of mass removed by erosion or added by deposition. W_f the summation of displacement from existing forces (W_i), and rebound or subsidence by erosion/deposition (W_r). W_f comes from the FEM solution,

$$W_f = [M_s]^{-1} \{f_g\}$$

where $[M_s]^{-1}$ is the inverse of the stiffness matrix, and f_g the global force updated by gravitational forces of erosion/deposition.

An example of erosion and deposition is shown in Figure 2.9. A rectangular load, which represents a mountain, is placed on the top of a continuous plate. The mountain is eroded, and sediments are deposited in the downward area.

Appendix D: Nonlinear viscosity

Material properties of the lithosphere are obviously important in the analysis of the long-term lithospheric deformation. The behavior of rocks in the Earth can be adequately described by viscoelastic behavior. Rock rheology depends on temperature: as rocks get hotter, their viscosity decreases. For example, the asthenosphere under Japan has a viscosity of about 2.0×10^{19} PAS (Rydelek and Sacks, 1990) and a temperature of about 200 °C below its solidus (Sato and Sacks 1990). At lower temperatures, the viscosity increases. We therefore use surface heat flow as the major determinant for the viscosity structure.

Surface heat flow at the inner arc is about twice that at the outer arc in northeast Japan. We constructed a strength profile of the lithosphere and an effective viscosity structure based on heat flow data and experimental rheology laws. The strength profile of the lithosphere is based on the

brittle and ductile flow laws of lithospheric material and the observed heat flow. Byerlee's law is used to construct the brittle strength for sliding on preexisting fractures (Byerlee, 1967 b). Flow laws of granite, granulite and dunite define the ductile strength of the lithosphere in northeast Japan (Table 2.1). The steady-state flow law is (Carter and Tsenn, 1987):

$$\dot{\epsilon} = A \exp(-Q_c / RT) \sigma^n$$

where $\dot{\epsilon}$ is the steady-state strain rate, σ the differential stress, T the absolute temperature, R the gas constant, A a material constant, n the power-law exponent, and Q_c the activation energy.

The ductile strength of the material or the differential stress is

$$\sigma = \left\{ \frac{\dot{\epsilon}}{A} \exp(-Q/RT) \right\}^{\frac{1}{n}}$$

The strength profile is constructed combining the brittle strength and the ductile strength. The smaller of these is the strength, and the brittle-ductile transition is then obtained from the strength profile.

Viscosity is a key parameter in lithospheric deformation. We consider both the viscosity obtained from experiment derived flow laws and the viscosity obtained from the observables of the actual deformation, e.g, gravity and topography. Viscosity can be linear or nonlinear. For linear viscosity, $n = 1$. Linear viscosity is defined in terms of the differential stress and the steady state strain rate as

$$\eta = \frac{\sigma}{\dot{\epsilon}}$$

For nonlinear viscosity, we can calculate the effective viscosity with respect to strain rate,

$$\eta = \frac{1}{2} \cdot \left(\frac{1-n}{n}\right) \left\{ A \exp(-Q/RT) \right\}^{-\frac{1}{n}} = (2\dot{\epsilon})^{\frac{1-n}{n}} \frac{1}{c}$$

and the effective viscosity with respect to stress,

$$\eta = \frac{c}{n-1}$$

where the viscosity coefficient (c) is,

$$c = \frac{\exp(Q_c / RT)}{2A}$$

The viscosity coefficient is a quantity that is independent of stress and strain rate. The viscosity coefficient and n are the two quantities used in the FEM computation (Williams, 1990). if $n=1$, $\eta = \eta_0$. Given the limitations in the available data, there is no chance to evaluate a more complicated viscosity law than linear. Therefore we determine an equivalent linear viscosity. Rydelek and Sacks (1988, 1990) and Williams (1990), modeled the lithosphere as a Maxwell viscoelastic solid. The Maxwell time constant (τ) defines the time-dependency of a viscoelastic material. It is the viscosity of the material divided by its shear modulus (η_0 / μ). The Maxwell time constant is used to indicate whether a material may be considered as an elastic solid or a viscous fluid over the time period of interest. We are interested in long-term time scales, i.e., on the order of millions of years. Any material with a time constant greater than this is assumed to behave elastically, while any materials with a time constant very much less than this behaves as a viscous fluid.

Ductile flow depends strongly on temperature. The temperature distribution is derived from the surface heat flow data (Furukawa and Uyeda, 1989) by solving the 1-D steady-state heat conduction equation (Bodri, Iizuka and Hayakawa, 1991). Thicknesses of the upper crust and lower crust comes from the results of the Research Group of Reflection Seismology (1973). The heat conductivity of the upper crust, lower crust, and upper mantle are 3.0, 2.5, and 4.0 W/mK respectively. The radiogenic heat generation for the upper crust and the lower crust are 1.0 and 0.4 $\mu\text{W}/\text{m}^3$ respectively, and there is no heat generation in the upper mantle. The depth of the brittle-ductile transition is about 5 km at the inner arc and increases to 50 km at the east of the outer arc (Fig. 2.8).

The flow law parameters are given in Table D.1:

Table D.1. The steady-state flow-law parameters for granite, granulite and dunite

Material	$\log_{10}A$ ($\text{MPa}^{-n}\text{S}^{-1}$)	n	Q_c (KJmol^{-1})	References
Westely granite(wet)	-3.7	1.9	140.6	Carter & Tsenn(1990)
Pikwitonei granulite	4.15	4.2	455	Wilks & Carter(1991)
Anita Bay Dunite (wet)	4	3.4	444	Carter & Tsenn(1990)

Vita

Shaosong Huang

Education: **Ph.D. in Geophysics**, Virginia Polytechnic Institute and State University (Virginia Tech), September 1996.
 M.S. in Geophysics, Graduate School of Chinese Academy of Geological Sciences, Beijing, P. R. China, July 1988.
 B.S. in Geology, Department of Earth Sciences, Nanjing University, P. R. China, July 1985.

Experience:

8/95-present Geophysicist, Seismic Data Processing, Geco-Prakla, NSA
8/91-6/95 Teaching/Research Assistant, Dept. of Geological Sciences, Virginia Tech
8/88-7/91 Junior Petroleum Geophysicist, Institute of Petroleum Geology, Beijing, P. R. China

Personal: Date of birth: Dec. 2, 1965
 Place of birth: Fujian, P. R. China